Nanoscale non-collinear magnetic structures in Co-based epitaxial ultrathin films

Dissertation
zur Erlangung des Doktorgrades
an der Fakultät für Mathematik, Informatik und
Naturwissenschaften
Fachbereich Physik
der Universität Hamburg

vorgelegt von

Marco Perini

Hamburg
2019

Gutachter/innen der Dissertation:
Prof. Dr. Roland Wiesendanger
Dr. Robert Frömter

Zusammensetzung der Prüfungskommission:
Prof. Dr. Roland Wiesendanger
Dr. Robert Frömter
Prof. Dr. Peter Schmelcher
Prof. Dr. Stefan Heinze
Prof. Dr. Michael Thorwart

Vorsitzende/r der Prüfungskommission:
Prof. Dr. Peter Schmelcher

Datum der Disputation:
15.02.2019

Vorsitzender Fach-Promotionsausschusses PHYSIK:
Prof. Dr. Wolfgang Hansen

Leiter des Fachbereichs PHYSIK:
Prof. Dr. Michael Potthoff

Dekan der Fakultät MIN:
Prof. Dr. Heinrich Graener

Abstract

Magnetic skyrmions are localized non-collinear spin configurations with non-trivial topology, which gives them stability against external perturbations. For this reason these objects could be the fundamental information carriers for the next generation of data storage devices. Among the different materials where skyrmions have been observed, several Co-based systems have shown the possibility to stabilize skyrmions at room temperature. Investigating the properties of these films can help to gain a deeper understanding of the mechanisms responsible for the stabilization of non-collinear objects. In this study extended Co films are grown epitaxially on two different substrates, namely Ir(111) and Pt(111), and in the first case two different additional top layers, Pt and Rh, are deposited. The magnetic properties of these films are investigated using spin-polarized scanning tunnelling microscopy. Co/Ir(111), Pt/Co/Ir(111) and Co/Pt(111) films all display ferromagnetic out-of-plane domains, separated by nanometer-sized domain walls. The walls possess unique rotational sense, as demonstrated by using tips with different magnetization directions, as well as by in-plane magnetic fields. The results are compared with density functional theory calculations, which help to understand the role of the different magnetic interactions in the stabilization of domain walls. Additionally, room temperature magnetic domains are visible on a Co double layer on Ir(111).
Rh/Co/Ir(111) islands present not only an increased number of domain walls, separating out-of-plane domains, but also isolated skyrmions coexisting with them in zero magnetic field. The non-collinear magnetic structures can be easily detected thanks to a large non-collinear magnetoresistance, which modifies the film's local density of states at different energies. Skyrmions with diameters around 3 nm are observed in the virgin magnetic state, and they can also be nucleated from a ferromagnetic background using the STM tip. This system is thus of great interest to study all-electrical skyrmion creation and detection processes at zero magnetic field. This thesis demonstrates how Co-based epitaxial films can host different types of non-collinear magnetic structures, whose properties could be exploited in view of the development of technological applications.

Inhaltsangabe

Magnetische Skyrmionen sind lokalisierte nicht-kollineare Spin-Konfigurationen mit nicht-trivialer Topologie, die ihnen Stabilität gegen externe Störungen verleihen. Aus diesem Grund könnten diese Objekte die grundlegenden Informationsträger für die nächste Generation von Datenspeichergeräten sein. Unter den verschiedenen Materialien, bei denen das Auftreten von Skyrmionen beobachtet wurde, waren viele Co-basierte Systeme in der Lage, Skyrmionen bei Raumtemperatur zu stabilisieren. Die Untersuchung der Eigenschaften dieser Schichten kann helfen, ein tieferes Verständnis jener Mechanismen zu erlangen, die für die Stabilisierung von nicht-kollinearen Objekten verantwortlich sind. In dieser Studie werden erweiterte Co-Schichten epitaktisch auf zwei verschiedenen Substraten gewachsen, nämlich Ir(111) und Pt(111), und im ersten Fall werden zwei verschiedene zusätzliche Deckschichten, Pt und Rh, verdampft. Die magnetischen Eigenschaften dieser Schichten werden mittels spin-polarisierter Rastertunnelmikroskopie untersucht. Co/Ir(111), Pt/Co/Ir(111) und Co/Pt(111)-Schichten zeigen alle senkrechte ferromagnetische Domänen, die durch nanometergroße Domänenwände abgegrenzt sind. Die Wände besitzen einen festen Drehsinn, wie durch Spitzen mit unterschiedlichen Magnetisierungsrichtungen sowie durch in-plane Magnetfelder gezeigt wird. Die Ergebnisse werden mit Dichtefunktionaltheorie-Berechnungen verglichen, die helfen, die Rolle der verschiedenen magnetischen Wechselwirkungen bei der Stabilisierung von Domänenwänden zu verstehen. Zusätzlich sind magnetische Domänen bei Raumtemperatur auf einer Co-Doppellage auf Ir(111) sichtbar.
Rh/Co/Ir(111)-Inseln zeigen nicht nur eine erhöhte Anzahl von Domänenwänden, die senkrechte Domänen abgrenzen, sondern auch isolierte Skyrmionen, die mit ihnen im Null-Magnetfeld koexistieren. Die nicht-kollinearen magnetischen Strukturen sind dank eines großen nicht-kollinearen Magnetowiderstandes leicht zu erkennen, der die lokale Zustandsdichte der Schicht bei verschiedenen Energien verändert. Skyrmionen mit Durchmessern um 3 nm werden im nativen magnetischen Zustand beobachtet und können mit der STM-Spitze auch in einem ferromagnetischen Hintergrund erzeugt werden. Dieses System ist daher von großem Interesse für die Untersuchung von elektrischen Prozessen zur Erzeugung und Erkennung von Skyrmionen im Null-Magnetfeld.
Diese Arbeit zeigt, wie Co-basierte epitaktische Schichten verschiedene Arten von nicht-kollinearen magnetischen Strukturen beherbergen können, deren Eigenschaften

im Hinblick auf die Entwicklung technologischer Anwendungen genutzt werden könnten.

Contents

Abbreviations

HDD	hard disk drive
DMI	Dzyaloshinskii-Moriya interaction
STM	scanning tunnelling microscopy
$E_{\mathbf{F}}$	Fermi energy
dI/**d**U	differential conductance
LDOS	local density of states
TMR	tunnelling magnetoresistance
TAMR	tunnelling anisotropic magnetoresistance
NCMR	non-collinear magnetoresistance
UHV	ultra-high vacuum
DFT	density functional theory
fcc	face-centered cubic
hcp	hexagonal close-packed
T_c	Curie temperature
vac-DOS	vacuum density of states
MR	magnetoresistance
FM	ferromagnetic
DW	domain wall
RT	room temperature
STT	spin-transfer torque

Chapter 1

Introduction

Recent years have seen the evolution of new technologies at ever increasing speed. With smart devices permeating more and more aspects of everyday life, the amount of information that is collected, stored and retrieved everyday grows exponentially. Digital data is produced not only by devices such as smartphones, computers and tablets, but in an increasing portion by so-called "embedded devices", including medical implants, security cameras and smart vehicles [1]. One of today's technological challenges is how to store efficiently this growing amount of information. One of the most common devices for data storage is the hard disk drive (HDD). The information in it is encoded in bits, with two possible states "0" and "1". Combinations of "0"s and "1"s allow to codify all types of digital data, ranging from texts and numbers to images and videos. In a HDD the physical bits are small ferromagnetic domains, whose magnetization can be oriented in two, typically opposite directions, corresponding to the two states of a digital bit. The size of such domains has decreased with the years, from 0.3 mm^2/bit in 1958 to 320 nm^2/bit in 2018 [2], thus allowing more information to be stored in the same area. This technology is, however, slowly reaching its natural limitations, as the size of the magnetic bits cannot be decreased arbitrarily without affecting their thermal stability, signal-to-noise ratio or the magnetic field necessary to switch them [3]. Additionally, the reading and writing of the bits is performed by a small electromagnet, the HDD "head", positioned only a few nanometers away from the magnetic surface hosting the bits: physical shocks, contamination sources or electronic failures can all lead to a crash of the head into the surface, usually causing loss of data.
To overcome the limitations presented above, several alternatives to HDDs have been proposed. Among these, it is worth mentioning the racetrack memory [4], or domain-wall memory, which might offer storage densities comparable to conventional HDDs, with better performances in reading and writing operations [5]. Instead of having a head mechanically moving over the bits on a surface, the magnetic domains are stored in a wire and are moved coherently along it using spin-polarized current pulses. In this way they pass above the read and write heads, which are at fixed positions. This design allows furthermore to create arrays of wires in 3D, in-

creasing the storage density with respect to 2D arrangements typical for HDDs.

Another magnetic configuration which could be used as information carrier is the magnetic skyrmion. It corresponds to a localized non-collinear arrangement of spins which is topologically different from a collinear ferromagnetic state, and possesses for this reason an increased stability against annihilation [6]. Such objects have been found in non-centrosymmetric bulk crystals [7–10] as well as in ultrathin metal films composed of various materials [11–14]. It has been shown that skyrmions can be written and detected in numerous ways [12, 15–22], and that they can be moved by means of electric currents [23–25] which are in some cases several orders of magnitude lower than for domain walls. For these reasons several implementations of skyrmion racetrack memories have been proposed, where the locally ferromagnetic and skyrmion configurations constitute the two states of a digital bit [15, 26, 27]. Skyrmions could also be used as building blocks for neuro-inspired computation paradigms [28], exploiting their magnetoresistance to build non-linear resistive components [29].
Co-based ultrathin films have recently attracted significant attention in these research fields, as it has been shown that it is possible to stabilize skyrmions at room temperature by having Co in contact with materials with strong spin-orbit coupling, such as Pt and Ir [25, 30–32]. This arrangement is claimed to generate a large Dzyaloshinskii-Moriya interaction (DMI) [33, 34], which is responsible for the thermal stability of the observed skyrmions.

In this thesis, the magnetic properties of atomically-thin Co films deposited on different substrates are investigated. The effects of two different top layers, namely Pt and Rh, are also studied. The films are deposited epitaxially, contrarily to a large part of the ongoing research in the field, which focusses on sputter-deposited films. Using epitaxial growth more ordered films and interfaces can be obtained, which also allows to compare the obtained results with *ab-initio* calculations. The films are investigated using spin-polarized scanning tunnelling microscopy (SP-STM). This technique has proven itself to be very versatile in the study of nanoscale magnetism: with its extremely high spatial resolution it has been possible to observe spin configurations at the atomic scale [11, 35], and using the STM tip magnetic skyrmions can be locally manipulated [12, 20].

Chapter 2 gives an overview on the relevant magnetic interactions responsible for non-collinear magnetism in ultrathin films, as well as a description of the operational principle of SP-STM. The last part of the Chapter briefly covers the details of the experimental set-up.
Chapter 3 describes the magnetic state of extended Co films on Ir(111) and Pt(111), as well as some of the properties of the observed domain walls. The effect of an additional Pt top layer is also studied, and compared with density functional theory

calculations.
Chapter 4 shows how the magnetism of Co/Ir(111) films is drastically modified by the deposition of a Rh top layer, producing a variety of nanometer-size non-collinear magnetic configurations.
Finally, Chapter 5 summarizes the obtained results and provides an outlook for future developments.

Chapter 2

Theoretical background and Experimental Set-up

This Chapter provides the theoretical knowledge necessary for the understanding of the results presented in this thesis, as well as some details on the experimental methods that have been used. The first Section (2.1) deals with the main interactions playing a role in non-collinear magnetism, described first in an atomistic model (Section 2.1.1) and then in the so-called micromagnetic framework (Section 2.1.2). Section 2.1.3 presents the main properties of the two non-collinear magnetic structures studied in this work, namely magnetic domain walls and skyrmions. The second part of the Chapter (Section 2.2) briefly describes the working principle of SP-STM and the main effects which allow to study non-collinear magnetism with STM. Section 2.3 provides a concise description of the main steps of sample preparation, as well as an overview of the experimental set-up that has been used.

2.1 Magnetic interactions and non-collinear magnetism in ultrathin films

2.1.1 Magnetic interactions at the atomic level

The following Section presents some of the most relevant magnetic interactions within an atomistic model. Higher-order interactions, such as the four-spin and the biquadratic interaction, are for simplicity not treated here, as they do not play a role in the stabilization of the magnetic structures observed in this thesis. The magnetic moment of an atom is due mostly to its electrons in the unfilled electron shells, and it is here assumed to be localised at the atom's position. For simplicity, the interactions will be described as acting between atoms located at positions $\vec{r_i}$ with magnetic moment $\vec{S_i}$, with $|\vec{S_i}| = 1$.

Exchange interaction

The exchange interaction is a consequence of the Coulomb interaction between electrons, combined with the Pauli exclusion principle. For two electrons with spins $\vec{S}_i$ and $\vec{S}_j$ the Hamiltonian associated with this interaction is described as [36]:

$$\mathcal{H} = -J_{ij}\,\vec{S}_i \cdot \vec{S}_j, \qquad J_{ij} = 2\int \varphi_i^*(\vec{r_1})\varphi_j^*(\vec{r_2})\frac{e^2}{|\vec{r_1}-\vec{r_2}|}\varphi_i(\vec{r_2})\varphi_j(\vec{r_1})\mathrm{d}\vec{r_1}\mathrm{d}\vec{r_2}, \tag{2.1}$$

where J_{ij} is the exchange integral, whose value depends on the overlap of the electrons' spatial wavefunctions φ_i and φ_j. Extending this model to a system of many atoms with classical spins results in an energy contribution described by the classical Heisenberg model:

$$E_{\text{ex}} = -\sum_{i,j} J_{ij}\,\vec{S}_i \cdot \vec{S}_j, \tag{2.2}$$

where the summation is performed over all pairs of spins. For the modelling of several magnetic systems it is sufficient to consider only the interactions between nearest-neighbours, with exchange constant J_1. Depending on its sign, J_1 can favour ferromagnetic ($J_1 > 0$) or antiferromagnetic ($J_1 < 0$) ordering of the spins. To accurately describe the magnetic state of specific systems it is, however, necessary to consider higher order J_{ij}s: the competition of Js with different strengths and signs can lead to the phenomenon of frustrated magnetism, which can, under certain conditions, stabilize non-collinear magnetic states [37–39]. As the distance between atom pairs becomes larger, the overlap between the respective electron wavefunctions becomes negligible. In metals, the exchange interaction, and therefore the J_{ij}, between atoms above a certain distance is mediated via conduction electrons: such electrons become spin-polarized due to a localized atomic magnetic moment, and their spin-polarization couples with the magnetic moment of another atom at a certain distance r. This is the Ruderman-Kittel-Kasuya-Yosida interaction, which presents a decaying oscillatory dependence on the distance between the magnetic moments [40–42].

Zeeman energy

The Zeeman energy for a system of many atoms with magnetic moment of magnitude μ in an external magnetic field $\vec{B}$ is expressed as:

$$E_{\text{Zeem}} = -\sum_i \mu\vec{S}_i \cdot \vec{B}, \tag{2.3}$$

and describes the tendency of the magnetic moments to align along the direction of the applied field.

Magnetic anisotropy

The crystalline structure of magnetic materials induces some energetically-favoured spin orientations, which are linked to the crystal symmetry axes of the system. This is a consequence of the spin-orbit interaction, which couples the atomic magnetic moments to the electric field generated by the electrons forming the crystal structure, called crystal field [36]. In the case of a thin film the resulting energy contribution can be assumed to depend on the angle of the spins with respect to a single axis. Such so-called uniaxial anisotropy takes the form:

$$E_{\text{aniso}} = -\sum_i K_{\text{eff}} \, (S_i^z)^2, \tag{2.4}$$

where S_i^z is the spin component along the anisotropy axis, assumed here to be in the z direction, perpendicular to the film. K_{eff} is the effective anisotropy constant, which combines contributions to the anisotropy from different sources. Volume and surface magnetocrystalline anisotropies account for the contribution of atoms located in the bulk and on the surface of crystals, respectively, and in the limit of thin films the surface anisotropy becomes predominant. K_{eff} also includes the effect from the so-called shape anisotropy, or stray field interaction, originating from the dipolar interaction between atomic magnetic moments. It can be described as acting between two magnetic dipoles $\vec{\mu_i}$ and $\vec{\mu_j}$ at a distance of $\vec{r}_{ij}$ according to:

$$E_{\text{dip}} = \frac{\mu_0}{4\pi} \sum_{i \neq j} \frac{1}{r_{ij}^3} \left[\vec{\mu_1} \cdot \vec{\mu_2} - \frac{3}{r_{ij}^2} (\vec{\mu_1} \cdot \vec{r}_{ij})(\vec{\mu_2} \cdot \vec{r}_{ij}) \right]. \tag{2.5}$$

Being a long-range interaction, the shape of the system determines the exact dipolar field acting on each magnetic moment. For a thin film the shape anisotropy always favours spins oriented in the plane of the film, while the magnetocrystalline surface anisotropy favours spins oriented perpendicularly to such plane.
The value of K_{eff} results from the contributions of the above-described terms. If $K_{\text{eff}} > 0$ the magnetic moments align along the anisotropy axis, which is in this case called easy axis, thus perpendicularly to the sample plane. If $K_{\text{eff}} < 0$ the magnetic moments align in the sample plane, which is in this case called easy plane.

Dzyaloshinskii-Moriya interaction

Another interaction which stems from the spin-orbit coupling is the antisymmetric exchange interaction, also known as Dzyaloshinskii-Moriya interaction (DMI) [33, 34]. The associated energy contribution can be written as:

$$E_{\text{DM}} = \sum_{i,j} \vec{D}_{ij} \cdot (\vec{S}_i \times \vec{S}_j), \tag{2.6}$$

where $\vec{D}_{ij}$ is the Dzyaloshinskii-Moriya (DM) vector. The value of $\vec{D}_{ij}$ is material-specific, but its axis can in general be deduced from the symmetry of the crystal

structure. In particular, for it to be non-zero the system must lack inversion symmetry. Consider two spins located at positions $\vec{r_1}$ and $\vec{r_2}$, and define the middle point between them as $\vec{r}_{ij} = (\vec{r_i} + \vec{r_j})/2$. Moriya's symmetry rules allow to determine the direction of $\vec{D}_{ij}$ as follows [34]:

- If a center of inversion is located at $\vec{r}_{ij}$, then $\vec{D}_{ij} = 0$.
- If a mirror plane perpendicular to $\vec{r_i} - \vec{r_j}$ includes $\vec{r}_{ij}$, then $\vec{D}_{ij} \perp (\vec{r_i} - \vec{r_j})$.
- If a mirror plane includes $\vec{r_1}$ and $\vec{r_2}$, then $\vec{D}_{ij} \perp$ mirror plane.
- If a two-fold rotation axis is perpendicular to $\vec{r_i} - \vec{r_j}$ and includes $\vec{r}_{ij}$, then $\vec{D}_{ij} \perp$ rotation axis.
- If an n-fold rotation axis ($n \geq 2$) includes $\vec{r_i}$ and $\vec{r_j}$, then $\vec{D}_{ij} \parallel (\vec{r_i} - \vec{r_j})$.

In ultrathin films the interface between the magnetic layer and the substrate breaks the inversion symmetry, and the interfacial DMI results from the coupling of two spins $\vec{S_i}$ and $\vec{S_j}$ via a non-magnetic substrate atom, provided the substrate has a large spin-orbit coupling, as in the case of heavy metals such as Ir and Pt [43]. In such a configuration the DM vector lies perpendicular to the plane of the triangle having the two magnetic atoms and the substrate atom as vertices [44]. Equation 2.6 shows that the DMI favours spins which are oriented perpendicularly to each other and, more generally, a non-collinear spin alignment [45]. The energy contribution (for a single pair of spins) can also be rewritten as:

$$E_{\mathrm{DM}} = \vec{D}_{ij} \cdot (\vec{S_i} \times \vec{S_j}) = (\vec{D}_{ij} \cdot \hat{n}) \sin(\varphi_{ij}), \tag{2.7}$$

where $\hat{n}$ is the unit vector pointing in the direction of $(\vec{S_i} \times \vec{S_j})$ and φ_{ij} is the angle between the two spin directions. The relation $E_{\mathrm{DM}}(\varphi) = -E_{\mathrm{DM}}(-\varphi)$ now shows that spin structures rotating in different directions are not energetically equivalent, and that the DMI favours a specific rotational sense, which depends on the sign of $\vec{D}_{ij} \cdot \hat{n}$.

2.1.2 Magnetic interactions in the continuum approximation

Having defined the magnetic interactions between isolated atoms as above, one could retrieve the magnetic state of a system by minimizing the total energy for all its spins. For large ensembles of spins, this could become computationally too expensive. One way to overcome this limitation consists in using a continuum approximation, in which the isolated spins $\vec{S_i}$ located at fixed positions $\vec{r_i}$ are replaced by a vector field of magnetization $\vec{m}(\vec{r}) = \vec{M}(\vec{r})/M_S$, where the saturation magnetization M_S is assumed constant ($|\vec{m}| = 1$). Following the variational principle, $\vec{m}(\vec{r})$ is then chosen as to minimize the total energy of the system. This continuum approximation for the treatment of magnetic interactions takes the name of micromagnetism [46].
Within such an approximation the energy contributions from the different interactions are expressed in terms of energy densities, and the total energy of the system

results from a spatial integration of these quantities. The exchange energy density is expressed as:

$$e_{\text{ex}} = A(\nabla \vec{m})^2, \tag{2.8}$$

which describes the energy penalty for magnetic configurations that deviate from a constant equilibrium magnetization direction. The higher the exchange stiffness A, the larger the energy penalty.
The anisotropy energy density is described in the most general form in terms of spherical harmonics. In the case of uniaxial anisotropy this simplifies, up to fourth order terms, to:

$$e_{\text{aniso}} = K_1 \sin^2(\theta) + K_2 \sin^4(\theta), \tag{2.9}$$

where K_1 and K_2 are the first two anisotropy constants, and θ is the angle between the magnetization direction and the anisotropy axis. Similarly to what has been described in the atomistic case, a large positive K_1 indicates that the magnetization tends to align along the anisotropy axis (easy axis anisotropy), while a large negative K_1 favours a magnetization oriented in the plane perpendicular to the anisotropy axis (easy plane anisotropy). When K_2 has a comparable size to K_1 and opposite sign, the easy directions are found on a cone, whose angle with respect to the anisotropy axis depends on the ratio K_1/K_2 [46]. A K_2 with the same sign of K_1 makes the resulting anisotropy energy density larger, while opposite signs of the two constants can result in more complex spin arrangements.
A general formulation of the total energy of a magnetic system in a certain volume V, neglecting higher order exchange and DMI contributions, can be approximated by [45]:

$$E = \int_V \left[A(\nabla \vec{m})^2 + D w_{\text{DM}} - K_{\text{eff}}\, m_z^2 - B M_S\, m_z \right] \mathrm{d}^3\vec{r}, \tag{2.10}$$

having assumed both the applied magnetic field $\vec{B}$ and the anisotropy axis along the z direction. The material parameters A, D and K_{eff} account for the strength of exchange interaction, DMI and anisotropy, respectively. D is the so-called DM constant, and K_{eff} is the effective uniaxial anisotropy constant, which includes contributions from both the magnetocrystalline and the shape anisotropy. M_S is the micromagnetic analogue of μ. w_{DM} is the DMI energy functional, and its exact formulation depends on the symmetry class of the system. For the thin film case, with DMI originating at the interface between substrate and magnetic film of thickness t, a 2D formulation of Eq. 2.10 is expressed as follows [6]:

$$E = t \int_{Area} \Bigg\{ A \left[\left(\frac{\partial \vec{m}}{\partial x} \right)^2 + \left(\frac{\partial \vec{m}}{\partial y} \right)^2 \right] + D \left(m_z \frac{\partial m_x}{\partial x} - m_x \frac{\partial m_z}{\partial x} + m_z \frac{\partial m_y}{\partial y} - m_y \frac{\partial m_z}{\partial y} \right) \tag{2.11}$$

$$- K_{\text{eff}}\, m_z^2 - B M_S\, m_z \Bigg\} \mathrm{d}x \mathrm{d}y,$$

where the magnetization is assumed constant along the z direction, within the magnetic film. A disadvantage of such a formulation is that the exchange stiffness A includes all the contributions from the different J_{ij}s in a single number, and the model fails in describing accurately non-collinear states stabilized by the frustration of exchange interactions. To do so, more complex micromagnetic models have been developed [38, 39].

2.1.3 Non-collinear magnetic states

Several non-collinear magnetic configurations are stabilized by the competition between the previously described magnetic interactions. Two such configurations, domain walls and skyrmions, are described here in more detail.

Magnetic domain walls

A macroscopic ferromagnet contains a number of regions, called domains, inside each of which the magnetization is constant and points in a certain direction. In this way the demagnetization energy for the ferromagnet is reduced. Differently oriented domains are separated by domain walls, regions where the magnetization rotates from one direction to the other one. In the case of thin films with out-of-plane easy axis anisotropy, the domain magnetization is oriented along the z direction. The domain walls separating domains with opposite orientations are classified according to the plane of magnetization rotation: in Bloch-type walls the magnetization rotates in a plane parallel to the plane of the wall (helical wall), while in Néel-type walls the two planes are perpendicular to each other (cycloidal wall), see Fig. 2.1. It has been shown [47, 48] that the interfacial DMI favours Néel-type walls with spin rotation plane perpendicular to the DM vector $\vec{D}$. These walls possess a fixed sense of magnetization rotation, given by the sign of $\vec{D}$. Note that the transition between a Bloch and a Néel wall with increasing $|\vec{D}|$ is a continuous one: initially the Bloch wall is favourable because of the lower magnetostatic charges, but as the DMI in-

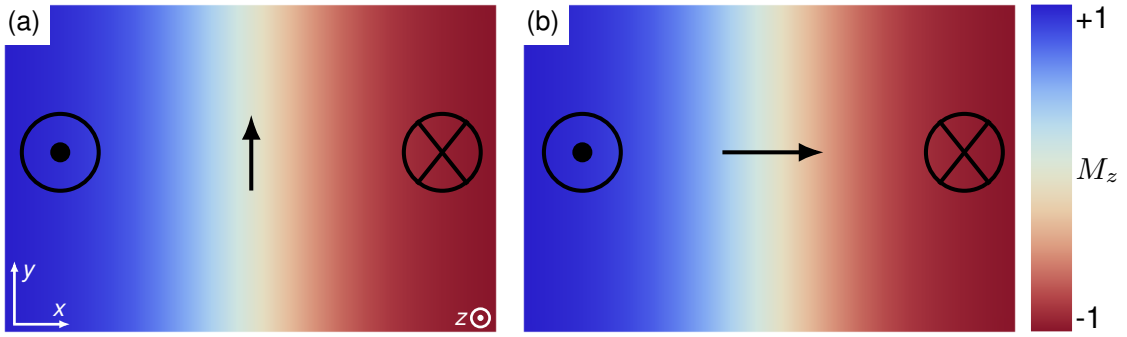

Figure 2.1: Sketch of a Bloch-type (a) and of a Néel-type (b) domain wall (top view).

creases the spins tend to align themselves according to a cycloidal configuration, and the energy cost of larger magnetostatic charges is compensated by the rotation around the DM vector [48].
Assuming to have Néel-type walls in a thin film system, their structure can be characterized by the single quantity $\varphi(\vec{r})$, which is the angle of the wall's magnetization with respect to the magnetic easy axis. This is a valid approximation over a wide range of parameters, and allows to determine the wall structure from the minimization of the one-dimensional total energy functional [47]:

$$E[\varphi] = \int_{-\infty}^{+\infty} \left[A \left(\frac{\mathrm{d}\varphi}{\mathrm{d}x} \right)^2 + D \frac{\mathrm{d}\varphi}{\mathrm{d}x} + K \sin^2 \varphi \right] \mathrm{d}x, \tag{2.12}$$

where the wall propagates along the x direction, and the DM vector has only one non-zero component, along the y direction and here indicated with D. Note that a number of simplifying assumptions have been made. First of all the magnetization in the wall is assumed to change only in the direction perpendicular to the wall, which is the x axis in this case, sometimes referred to as wall propagation direction. For this reason the total energy described in Eq. 2.12 is actually a total energy per unit length, as no integration in the y direction is performed. Additionally, the second anisotropy constant has been neglected, and only the first term, proportional to $\sin^2 \varphi$ has been considered, with effective anisotropy constant K. The following boundary conditions are introduced to account for the oppositely pointing ferromagnetic domains:

$$\lim_{x \to -\infty} \varphi(x) = 0, \qquad \lim_{x \to +\infty} \varphi(x) = \pi. \tag{2.13}$$

The energy functional in Eq. 2.12 can now be minimized with respect to φ, yielding the domain wall profile:

$$\varphi(x) = \arccos \left(\tanh \left(\sqrt{\frac{K}{A}} x \right) \right) = \arccos \left(\tanh \left(\frac{x}{w/2} \right) \right), \tag{2.14}$$

where the quantity $w = 2\sqrt{A/K}$ is defined as the wall width. Note that the DMI contribution to the energy functional in Eq. 2.12 results, after integration, in a constant term $-\pi|D|$, and therefore does not influence the shape of the domain wall. It does however enter the domain wall energy per unit length:

$$\sigma_{DW} = 4\sqrt{AK} - \pi|D|, \tag{2.15}$$

showing that the DMI does favour the creation of domain walls, although their width is, within this model, determined uniquely by exchange stiffness and anisotropy constant.
The domain wall profile of Eq. 2.14 describes the spin rotation for a single isolated wall, also referred to as a 180° domain wall. Such formula can be extended to pairs of walls, also known as 360° domain walls, as follows [49]:

$$\varphi_{360}(x) = \arccos \left(\tanh \left(\frac{x + c}{w/2} \right) \right) + \arccos \left(\tanh \left(\frac{x - c}{w/2} \right) \right), \tag{2.16}$$

where the additional parameter c corresponds to half of the distance between the centers of the two 180° walls. Eq. 2.16 can also be used to model the profile of magnetic skyrmions [50].

Magnetic skyrmions

Domain walls are solutions to a one-dimensional simplified version of the micromagnetic model of Eq. 2.11, with specific boundary conditions. It has been shown [6, 45] that, for certain material parameters and magnetic fields, the energy functional of Eq. 2.11 can also be minimized by solutions with axial symmetry, where the magnetization rotates only in a localized area, thus resulting in isolated particle-like objects. They have been called skyrmions after Tony Skyrme, who first introduced similar objects as solutions of the Skyrme model in particle physics [51]. The fundamental property of a skyrmion, which distinguishes it from a magnetic vortex, is its non-zero integer topological charge, also known as winding number or skyrmion number. This quantity is defined in two dimensions as [8]:

$$Q_{\text{top}} = \frac{1}{4\pi} \int_A \vec{m}(\vec{r}) \cdot \left(\frac{\partial \vec{m}}{\partial x} \times \frac{\partial \vec{m}}{\partial y} \right) \mathrm{d}\vec{r}, \tag{2.17}$$

where the integration is performed over the whole skyrmion area A. Q_{top} represents how many times the magnetization field $\vec{m}$ covers the unit sphere, where each point on the sphere corresponds to one possible orientation of $\vec{m}$ in 3D. So while the magnetization in a vortex only covers half of the unit sphere, in a skyrmion it covers

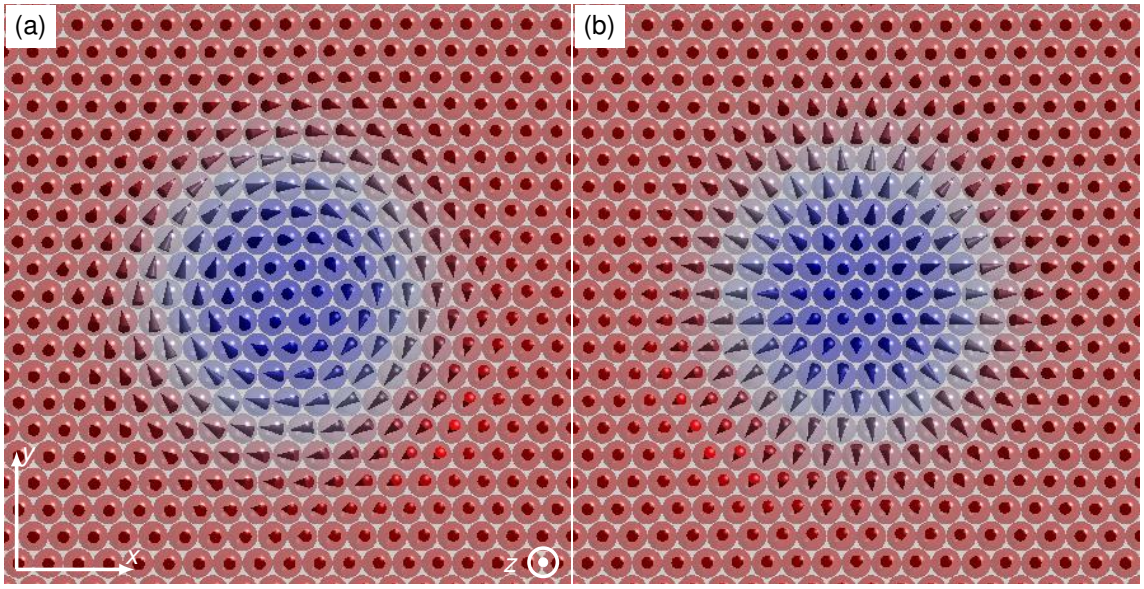

Figure 2.2: Schematic top view of a Bloch-type (a) and of a Néel-type (b) skyrmion. The spins are coloured according to their component along the z direction, with the same colour coding as in Fig. 2.1.

the whole of it. In a continuum model, states with different topology cannot be continuously transformed into one another, an effect known as topological protection: a skyrmion ($Q_{\text{top}} = 1$) cannot collapse into the ferromagnetic state ($Q_{\text{top}} = 0$), and is therefore a stable magnetic configuration. In real systems, where the atomic lattice is discrete, states with different topological numbers are separated by an energy barrier, thus providing (meta-)stability of magnetic skyrmions in certain materials in the appropriate conditions (for example at specific magnetic fields and temperatures). Similarly to domain walls, also skyrmions can be of Bloch or Néel-type, corresponding to a helical or cycloidal spin rotation when going from the center to the outside of the objects (see Figure 2.2). Which type of skyrmion is energetically favourable depends on the symmetry of the system, which determines the direction of the DM vector. While in bulk materials the DMI arising from the crystal structure stabilizes Bloch-type skyrmions [7, 10], in ultrathin films the interfacial DMI favours Néel-type skyrmions with a preferred sense of rotation [52], similarly to the case of domain walls. The stray field interaction (see Section 2.1.1) is known to stabilize magnetic bubbles with Bloch domain walls [53, 54]. Additionally, skyrmion lattices and (meta-)stable isolated skyrmions can also be produced by frustrated exchange interactions, which do not select a preferred wall type or rotational sense [37–39].
In this Section magnetic skyrmions have been defined starting from their non-zero topological charge. Strictly speaking, this definition also includes objects which are normally not labelled as skyrmions, such as stray-field-stabilized magnetic bubbles with Bloch-type walls. These objects, which have been extensively studied in the 1970s for applications in memory devices, usually present sizes between 100 nm and 1 µm, which are significantly larger than the typical sizes of DMI-stabilized skyrmions (between 5 and 100 nm) [8]. Additionally, the term "skyrmion bubble" has been used to refer to magnetic bubbles which present Néel-type domain walls with fixed sense of rotation, indicating an interplay of DMI and dipolar interaction (and Zeeman energy in case of applied magnetic fields) in the stabilization of such objects [16]. As the size of skyrmion bubbles approaches that of skyrmions, it becomes more difficult to operate a clear distinction between the two, since they share several common properties, such as finite topological charge and similar current-induced motion. It has been proposed to classify the two types of objects based on their radial magnetization profile [55]: whereas a skyrmion bubble would exhibit a large central area of collinear spins, corresponding to a plateau in the magnetization profile, in a skyrmion all the spins would be non-collinear with respect to each other, thus resulting in a magnetization profile without a plateau. It has, however, been claimed that this is not a robust criterion to separate the two types of objects [56, 57]. In view of technological applications, distinguishing between the two classes of objects might not constitute a major issue, as skyrmions and skyrmion bubbles share some relevant features for practical applications: they both possess a non-trivial topology, which guarantees stability against annihilation, and both can be artificially created and manipulated exploiting different effects [12, 16, 20, 25, 58,

59]. In Chapter 4 several isolated magnetic objects with fixed rotational sense and non-trivial topology will be shown. Only those presenting little to no collinearity in their center will be called skyrmions. Instead, objects with a central region of collinear spins which is several times larger than their domain wall width will only be referred to as isolated domains, despite their non-zero topological charge.

2.2 Scanning Tunnelling Microscopy on non-collinear magnetic structures

This Section presents the principle of operation of spin-polarized scanning tunneling microscopy (SP-STM), which is the experimental technique that has been used throughout this thesis to study non-collinear magnetism in ultrathin films. After a brief description of the operational principle of non-magnetic STM, the main imaging mechanisms used to detect spin structures are presented. STM simulations show how magnetic domain walls and magnetic skyrmions appear when imaged via such mechanisms.

2.2.1 Scanning Tunnelling Microscopy

Scanning tunneling microscopy (STM), invented by Gerd Binnig and Heinrich Rohrer in 1981 [60]) is a microscopy technique that relies on the phenomenon of quantum tunnelling of electrons between two electrodes through a potential barrier. In an STM set-up the electrodes are a metallic, atomically-sharp tip and a conductive sample, which are brought very close to each other (typically at a few Å distances), and the potential barrier is the material separating them, typically vacuum or air. A bias voltage is applied between the two electrodes to generate a net flow of electrons in one direction. The tunnelling process, and thus the tunnelling current, depends exponentially on the thickness of the potential barrier, i.e. the distance between tip and sample.
A simplified theoretical description of the tunnelling processes between tip and sample is given by Bardeen [61], approximating the STM set-up as a tunnel junction with a square potential barrier. The probability p of an electron in the state ψ_t and energy E_t in the tip to tunnel into the sample to a state ψ_s with energy E_s is given by the Fermi golden rule:

$$p = \frac{2\pi}{\hbar} |M_{\mathrm{t,s}}|^2 \, \delta(E_\mathrm{t} - E_\mathrm{s}), \tag{2.18}$$

where the δ is used to restrict the discussion to electrons tunnelling between states of same energy (elastic tunnelling). The quantity $M_{\mathrm{t,s}}$ is the tunnelling matrix element between the electronic states ψ_t and ψ_s. Bardeen showed that such element is

determined from the two wavefunctions as:

$$M_{\mathrm{t,\,s}} = \frac{\hbar^2}{2m} \int (\psi_{\mathrm{t}}^* \nabla \psi_{\mathrm{s}} - \psi_{\mathrm{s}} \nabla \psi_{\mathrm{t}}^*) \cdot \mathrm{d}S, \tag{2.19}$$

where the integration is performed on any surface within the potential barrier. A bias voltage U is applied between tip and sample, and the total tunnel current can be calculated as the sum of the tunnelling processes over all the possible tip and sample states ψ_{t} and ψ_{s}, respectively:

$$I = \frac{2\pi e}{\hbar} \sum_{\mathrm{t,\,s}} |M_{\mathrm{t,\,s}}|^2 \delta(E_{\mathrm{t}} - E_{\mathrm{s}}) \left[f(E_{\mathrm{t}} - eU) - f(E_{\mathrm{s}}) \right]. \tag{2.20}$$

The sum is weighted over the energy distributions of tip and sample states, described by the Fermi-Dirac distribution $f(E)$.

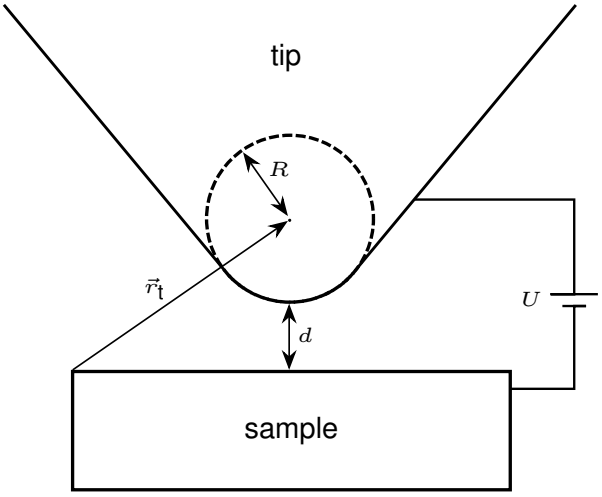

Figure 2.3: Schematic representation of the STM geometry: the tip apex in the vicinity of the sample surface can be assumed to be spherical, with curvature radius R, and at a distance of d from the surface. To have a net tunnel current, a bias voltage U is applied between tip and sample.

As seen in Eq. 2.19, to calculate the tunnelling matrix element it is necessary to provide a description for the wavefunctions of tip and sample. Tersoff and Hamann [62] assumed a spherical symmetry for the tip wavefunction, and thus considered ψ_{t} as an s-wave orbital located at the center of the tip's apex atom $\vec{r}_{\mathrm{t}}$. The tip apex has a curvature radius R and its center is at a distance d from the sample surface (see Figure 2.3). The resulting tunnel current, in the limit of small bias voltages (on the order of 10 meV in metals [63]), is then:

$$I \propto U \rho_{\mathrm{t}}(E_{\mathrm{F}})\, e^{2\kappa R} \sum_{\mathrm{s}} |\psi_{\mathrm{s}}(\vec{r}_{\mathrm{t}})|^2\, \delta(E_{\mathrm{s}} - E_{\mathrm{F}}), \tag{2.21}$$

where $\kappa = \sqrt{2m\phi}/\hbar$ is the effective decay constant, depending on the work function ϕ, assumed equal for tip and sample. The quantity $\rho_{\mathrm{t}}(E_{\mathrm{F}})$ is the local density of states (LDOS) of the tip at the Fermi energy, and similarly also the LDOS for the sample can be derived, by re-writing:

$$\sum_{\mathrm{s}} |\psi_{\mathrm{s}}(\vec{r}_{\mathrm{t}})|^2\, \delta(E_{\mathrm{s}} - E_{\mathrm{F}}) = \rho_{\mathrm{s}}(\vec{r}_{\mathrm{t}}, E_{\mathrm{F}}). \tag{2.22}$$

The tunnel current is then proportional to the sample's density of states at the center of the tip. This quantity in turn decays exponentially as the tip-sample distance increases:

$$\rho_{\mathrm{s}}(\vec{r}_{\mathrm{t}}) \propto |\psi_{\mathrm{s}}(\vec{r}_{\mathrm{t}})|^2 \propto e^{-2\kappa d}. \tag{2.23}$$

This simplified model is sufficient to show the exponential dependence of the tunnelling current on the distance between tip and sample.
In a more general description, the assumption of small bias voltages is relaxed, and in the continuous limit the tunnel current is found to be [64, 65]:

$$I \propto \int_0^{eU} \rho_{\mathrm{s}}(\vec{r}_{\mathrm{t}}, E_{\mathrm{F}} + \epsilon)\, \rho_{\mathrm{t}}(E_{\mathrm{F}} - eU + \epsilon)\mathrm{d}\epsilon, \tag{2.24}$$

thus showing that I depends in general on the integrated density of states of both tip and sample in the energy regime between E_{F} and $E_{\mathrm{F}} + eU$. For this reason, both changes in the sample topography and electronic density of states can result in changes of the measured tunnel current. One way to measure variations in the sample's LDOS at specific voltages is to measure the so called differential conductance, or $\mathrm{d}I/\mathrm{d}U$:

$$\frac{\mathrm{d}I}{\mathrm{d}U} \propto \rho_{\mathrm{s}}(\vec{r}_{\mathrm{t}}, E_{\mathrm{F}} + eU), \tag{2.25}$$

where the tip's LDOS has been assumed constant, for simplicity. The $\mathrm{d}I/\mathrm{d}U$ plays a very important role in SP-STM, since it allows to detect changes in the sample's electronic structure at specific energies, which can be induced by the sample's magnetic properties.

2.2.2 Spin-polarized Scanning Tunnelling Microscopy

In the previous Section it has been shown how measuring the tunnel current between tip and sample gives information about the topographic details of the sample surface, as well as about the sample's LDOS. In the case of a magnetic sample, such LDOS can undergo significant variations, resulting in several magnetoresistive effects, described in this Section, that give access to the local magnetic configuration.

Imaging mechanisms

Tunnelling magnetoresistance (TMR) The tunnelling magnetoresistance (TMR) describes how the tunnel current between two magnetic electrodes, separated by a thin insulator, depends on the relative orientation of their magnetizations. In the simple case of two ferromagnetic electrodes with same density of states, the tunnel current is found to be larger when the magnetizations are aligned parallel, compared to when they are antiparallel [66]. This can be understood from the drawings in Fig. 2.4. The exchange energy produces a spin-splitting of the LDOS in the ferromagnets. The two spin-polarized density of states are indicated as $\rho_{\uparrow}$ and $\rho_{\downarrow}$,

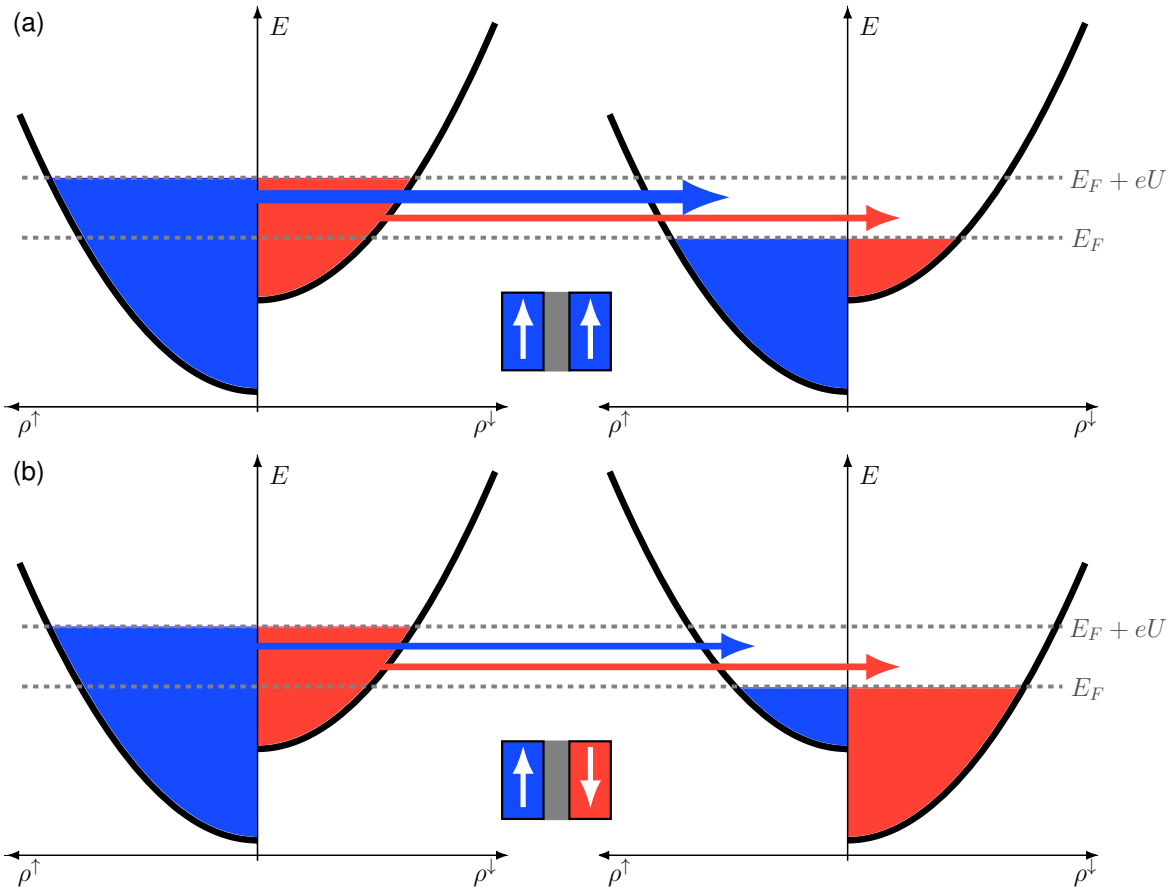

Figure 2.4: Schematic representation of spin-dependent tunnelling between ferromagnetic electrodes. When the two electrodes have parallel magnetization (a) the majority spin electrons can tunnel in a large amount of unoccupied majority spin states, producing a large tunnel current. When the electrodes have antiparallel magnetization (b) a smaller number of unoccupied states for the majority spin electrons is available, and the resulting tunnel current is lower. For simplicity, spin-flip and inelastic tunnelling processes are neglected.

corresponding to electronic states with up-pointing and down-pointing spins, respectively. This split results in spin-dependent electron tunnelling from one electrode to the other. For simplicity, only elastic tunnelling processes without spin-flip are considered, meaning that an electron can only tunnel into an unoccupied state having same energy and spin. In the case of a parallel alignment of the electrodes (Fig. 2.4(a)), a large number of electrons with the majority spin (spin-up in the Figure) can tunnel in a large number of unoccupied majority states, and few electrons with the minority spin (spin-down in the Figure) can tunnel in the few unoccupied minority states. The resulting spin-polarized current, given by the sum of the electronic tunnelling processes in the two spin channels, is therefore large. When the electrodes have antiparallel alignment (Fig. 2.4(b)), the electrons with the minority

spin can still tunnel in the unoccupied minority states, but only a fraction of the electrons with majority spin can tunnel, since the density of unoccupied majority spin states is reduced. This produces a tunnel current which is lower than in the parallel alignment case. In a more general case, it has been found that the conductance G of a magnetic tunnel junction can be expressed as [67]:

$$G \propto 1 + P_1 P_2 \cos\theta, \tag{2.26}$$

where θ is the angle between the magnetization directions of the two electrodes, and P_1 and P_2 are their effective spin polarizations. The effective polarization at a specific energy is defined as:

$$P(E) = \frac{\rho^{\uparrow}(E) - \rho^{\downarrow}(E)}{\rho^{\uparrow}(E) + \rho^{\downarrow}(E)}. \tag{2.27}$$

The TMR effect can also be used in an STM configuration, where the electrodes are now a magnetic sample and a magnetic tip [68, 69], and it constitutes the underlying mechanism of SP-STM. The Tersoff-Hamann model described in Section 2.2.1 can be extended to the case of ferromagnetic electrodes [70], with an additional parameter θ that refers to the angle between tip and sample magnetization directions. Assuming a constant tip's LDOS $\rho_{\mathrm{t}} = \rho_{\mathrm{t}}^{\uparrow} + \rho_{\mathrm{t}}^{\downarrow}$ and a tip's magnetization vector $\mathbf{m}_{\mathrm{t}} = (\rho_{\mathrm{t}}^{\uparrow} - \rho_{\mathrm{t}}^{\downarrow})\mathbf{e}_{\mathrm{t}}$, with $|\mathbf{e}_{\mathrm{t}}| = 1$, the tunnel current at the center of the tip's apex atom $\vec{r}_{\mathrm{t}}$ can be approximated as:

$$I(\vec{r}_{\mathrm{t}}, U, \theta) \propto \rho_{\mathrm{t}}\,\tilde{\rho}_{\mathrm{s}}(\vec{r}_{\mathrm{t}}, E_{\mathrm{F}} + eU) + \mathbf{m}_{\mathrm{t}} \cdot \tilde{\mathbf{m}}_{\mathrm{s}}(\vec{r}_{\mathrm{t}}, E_{\mathrm{F}} + eU). \tag{2.28}$$

Here the tilde symbol on $\tilde{\rho}_{\mathrm{s}}$ and $\tilde{\mathbf{m}}_{\mathrm{s}}$ indicates that the two quantities are integrated over the energies between E_{F} and $E_{\mathrm{F}} + eU$. Analogously to the standard STM case, the differential conductance can be computed:

$$\frac{\mathrm{d}I}{\mathrm{d}U}(\vec{r}_{\mathrm{t}}, U, \theta) \propto \rho_{\mathrm{t}}\,\rho_{\mathrm{s}}(\vec{r}_{\mathrm{t}}, E_{\mathrm{F}} + eU) + \mathbf{m}_{\mathrm{t}} \cdot \mathbf{m}_{\mathrm{s}}(\vec{r}_{\mathrm{t}}, E_{\mathrm{F}} + eU), \tag{2.29}$$

where now ρ_{s} and $\mathbf{m}_{\mathrm{s}}$ are evaluated only at the energy $E_{\mathrm{F}} + eU$. Using the definition of polarization given in Eq. 2.27, the differential conductance can then be re-written as:

$$\frac{\mathrm{d}I}{\mathrm{d}U}(\vec{r}_{\mathrm{t}}, U, \theta) \propto \rho_{\mathrm{t}}\,\rho_{\mathrm{s}}(\vec{r}_{\mathrm{t}}, E_{\mathrm{F}} + eU)[1 + \cos(\theta(\vec{r}_{\mathrm{t}}))\, P_{\mathrm{t}} P_{\mathrm{s}}(\vec{r}_{\mathrm{t}}, E_{\mathrm{F}} + eU)]. \tag{2.30}$$

The spin-polarized differential conductance is therefore sensitive to the relative orientation of tip and sample magnetizations, described by θ. This means that how a certain magnetic structure appears in an SP-STM measurement can highly vary depending on the tip magnetization direction (see Section 2.2.4).

Tunnelling anisotropic magnetoresistance (TAMR) The tunnelling anisotropic magnetoresistance (TAMR) is an effect due to spin-orbit coupling, which mixes electronic states with different orbital character and thus produces a modification of

the sample's LDOS which depends on its local magnetization direction. Contrarily to TMR, this effect does not depend on the *relative* magnetization of sample and tip, and in fact it can be observed also using non-magnetic tips [71, 72]. The analytical relation between the tunnel current and the sample magnetization direction depends on the specific orbitals which mix together. For a 1D domain wall, assuming a large exchange splitting of majority and minority bands in the LDOS, it has been shown [63, 72] that the current can be approximated as to be proportional to $\cos^2(\theta)$, where θ is the angle of the sample magnetization with respect to the local spin quantization axis. The TAMR thus allows to distinguish between out-of-plane and in-plane oriented magnetic configurations, without the need of a magnetic tip.

Non-collinear magnetoresistance (NCMR) Another magnetoresistive effect which does not require a magnetic sensitive tip is the non-collinear magnetoresistance (NCMR). It has been observed for magnetic structures, such as skyrmions and inhomogeneous spin spirals, which present a non-uniform non-collinearity [17, 73]. Contrarily to TAMR, it does not depend on the absolute orientation of each atomic spin, but rather on the difference in the alignment between neighbouring spins [74, 75]. The effect originates from a mixing of the spin-up and spin-down bands for non-collinear states, resulting in a modification of the LDOS. The NCMR allows to distinguish between locally collinear and non-collinear areas, such as the ferromagnetic state and the center of a domain wall, respectively. How the tunnel current is modified by the NCMR is highly dependent on the details of the sample's LDOS. An attempt to model the modification in the $\mathrm{d}I/\mathrm{d}U$ signal due to the NCMR in a constant-current image (see Section 2.2.3) is presented in Chapter 4.

Induced magnetic polarization A magnetic layer can induce a spin-polarization in a non-magnetic layer in contact with it. In a thin film geometry, the non-magnetic atoms on top of a magnetic film can have non-zero magnetic moments. If the magnetic layer is not in a ferromagnetic state, but rather in more complex arrangements such as an antiferromagnetic or a non-collinear state, the induced magnetic moments in the top layer might vary in intensity throughout the layer. This produces a variation in the system's LDOS, which could be detected using STM. Such an effect has been experimentally observed in Rh/Fe/Ir(111) [76].

2.2.3 SP-STM measurements

The dependence of the tunnelling current on the LDOS of tip and sample, as well as on their relative distance, can be exploited in different types of measurements. In a typical STM measurement the tip is moved back and forth in straight lines over a selected area, and different quantities such as tunnel current and $\mathrm{d}I/\mathrm{d}U$ are recorded as a function of the tip position across the scan area. In this way one obtains a 2D map of the measured quantities on the sample surface. This Section briefly

describes the most common types of STM measuring modes, which are often used in combination to simultaneously acquire information about different properties of the surface.

Constant-height mode The simplest way to measure the variations in tunnel current is to keep the tip at a fixed height while it moves across the sample surface: the measured variations can then be directly attributed to changes in the sample topography or LDOS, since the tip did not move in the z direction. With such a procedure there is, however, a risk of a mechanical contact between tip and sample, for example when the sample surface exhibits a high protrusion and the tip is not sufficiently far from the surface. Such mechanical contacts can produce massive changes on both the tip and the sample, and are typically to be avoided. For this reason this measuring mode is rarely used in practice.

Constant-current mode A safer way to move the STM tip across a surface consists in using a feedback loop that adjusts the tip height in order to keep the tunnel current at a constant value. When the tip first encounters a protrusion, the tip-sample distance is reduced, and the current starts to increase. The feedback loop then retracts the tip from the surface, increasing the tip-sample distance and bringing back the current to the desired value. This procedure works in a similar fashion when the tip encounters a depression of the surface. In this mode the height of the tip is recorded simultaneously with the tunnel current, and a height map of the sample surface can then be reconstructed from it. In this thesis a map of the tip height in a constant-current measurement is also referred to as an STM constant-current map. Note that, as the current can be modified by variations in the LDOS, it is sometimes possible to observe changes in the tip height due to modifications of the electronic structure, due for example to TMR or other contrast mechanisms.

Differential conductance (dI/dU) measurement The magnetoresistive effects described in Section 2.2.2 produce variations in the LDOS which are usually best visible at specific energies. One way to experimentally detect such modifications consists in finding a bias voltage where the LDOS modifications are more pronounced, and measure the differential conductance as a function of the lateral tip position. The advantage of this method with respect to measuring the tunnel current is that the $\mathrm{d}I/\mathrm{d}U$ is sensitive to the changes of LDOS only at the selected bias voltage, while in the tunnel current all the LDOS variations from the Fermi energy to the chosen bias voltage are integrated together in the signal, making it harder to detect them and to disentangle different contributions. One way to directly measure the $\mathrm{d}I/\mathrm{d}U$ consists in using a lock-in amplifier. A sinusoidal modulation of amplitude U_m and frequency ω is added to the applied bias voltage U_0:

$$U(t) = U_0 + U_m \sin(\omega t). \tag{2.31}$$

The tunnel current, as a function of the applied voltage of Eq. 2.31, can be approximated using a first order Taylor expansion:

$$I(U(t)) \sim I(U_0) + \frac{\mathrm{d}I}{\mathrm{d}U}\Big|_{U=U_0} U_m \sin(\omega t), \tag{2.32}$$

and it is multiplied by a reference signal [1] $U_{\text{ref}}(t) = \sin(\omega t + \phi)$ with a phase ϕ that can be manually adjusted:

$$U_{\text{ref}}(t) I(U(t)) \sim I(U_0)\sin(\omega t + \phi) + \frac{\mathrm{d}I}{\mathrm{d}U}\Big|_{U=U_0} U_m \sin(\omega t)\sin(\omega t + \phi) \tag{2.33}$$

$$= \frac{\mathrm{d}I}{\mathrm{d}U}\Big|_{U=U_0} \frac{U_m}{2}\sin(\phi) + I(U_0)\sin(\omega t + \phi) + \frac{\mathrm{d}I}{\mathrm{d}U}\Big|_{U=U_0} \frac{U_m}{2}\sin(2\omega t + \phi). \tag{2.34}$$

By applying a low-pass filter with cut-off frequency ω it is then possible to isolate a DC signal which is proportional to the differential conductance evaluated at the selected bias voltage. The lock-in technique allows to measure the $\mathrm{d}I/\mathrm{d}U$ simultaneously with the constant-current height map. Typical voltage modulations are on the order of 10% of the applied bias voltage, and frequencies on the order of 1 kHz.

Spectroscopy curves As seen in Section 2.2.1, the $\mathrm{d}I/\mathrm{d}U$ signal is proportional to the sample's LDOS at the position of the tip apex. The LDOS decreases in intensity with increasing distance from the surface, and what is measured by the $\mathrm{d}I/\mathrm{d}U$ is usually called vacuum density of states. At distances of a few angstroms, which are typical tip-sample distances for an STM set-up, this quantity still retains meaningful information on the sample's LDOS. One way to study the energy dependence of the LDOS consists in recording the differential conductance at different biases. This is typically done by fixing the position of the tip above a certain location in the sample, and sweeping the bias voltage within a selected range of values. For each bias value the $\mathrm{d}I/\mathrm{d}U$ is recorded, so that at the end a curve of $\mathrm{d}I/\mathrm{d}U(U)$ is obtained. This procedure, also known as single point spectroscopy, gives information about the sample's LDOS in a certain energy range. By comparing curves at different sample positions it is possible to observe at which energies the LDOS is modified. It is also possible to record a spectroscopy map, where for each point in a 2D grid a single spectrum is recorded. To obtain data with sufficient energy and spatial resolution, this type of measurement typically requires several hours, but the resulting map gives a full picture of the LDOS distribution in both energy and space.

2.2.4 Simulation of (SP-)STM images

To understand how various non-collinear spin structures appear when imaged via different magnetoresistive effects, it is useful to simulate the expected STM contrast, that can be used as a reference for the interpretation of the experimental results. The

[1] The amplitude of the reference signal is assumed to be equal to 1, for simplicity.

simulations presented in this thesis have been performed by adapting the code written by Niklas Romming [77].
The magnetic configuration to be studied is modelled by a list of normalized magnetic moments $\vec{S}_i$ located at the atomic positions $\vec{r}_i$. The current is calculated by assuming an exponential decay of its intensity with the distance from the surface, and assuming that all surface atoms have identical properties [78]. In these simulations the densities of states of sample and tip, which are in general material specific and have to be calculated separately, are for simplicity not taken into account. For this reason the calculated current, for a flat surface, is only sensitive to modifications due to TMR, in case of a tip with non-zero spin-polarization, or to other electronic effects as those described in Section 2.2.2. The tunnel current at the tip position $\vec{r}_\mathrm{t}$ is thus calculated as:

$$I(\vec{r}_\mathrm{t}) = \sum_i I_i^\mathrm{loc}\, e^{-2\kappa|\vec{r}_\mathrm{t}-\vec{r}_i|}, \tag{2.35}$$

where $\kappa = \sqrt{2m_e\phi}/\hbar$ is the decay constant, and ϕ is the sample work function. As I decays exponentially in intensity with the distance, the sum in Eq. 2.35 can be computed just over atoms within a certain distance of $\vec{r}_\mathrm{t}$, to speed up the calculation. Given a tip-sample distance of z_0, a typical cut-off distance is $3z_0$. I_i^loc contains the contributions from the different magnetoresistive effects described in Section 2.2.2, excluding polarization effects for simplicity:

$$I_i^\mathrm{loc} = I_0 \left(1 + \gamma_P \vec{S}_i \cdot \vec{m}_\mathrm{t} + \gamma_\mathrm{T}(S_i^z)^2 + \gamma_N \frac{\bar{\alpha}}{\pi}\right), \tag{2.36}$$

where γ_P, γ_T and γ_N are pre-factors determining the strength of TMR, TAMR and NCMR, respectively, and $\vec{m}_\mathrm{t}$ is the tip magnetization direction. The TAMR depends on the square of the z component of each spin [63, 72], while the NCMR contribution is assumed to be proportional to $\bar{\alpha}$, which is the mean angle between $\vec{S}_i$ and its nearest neighbours [73, 74], normalized by its maximum value π.

Figure 2.5(a) shows the spin structure for two Néel domain walls with same sense of magnetization rotation. Figures 2.5(b) and (c) display the simulated TAMR and NCMR contrast, respectively, assumed to be positive. The resulting images are very similar, because the areas of maximal non-collinearity, i.e. the center of the walls, correspond to where the wall magnetization is pointing along the in-plane direction. Thus, both the TAMR and NCMR signals are largest at the wall center, and decrease in intensity with slightly different rates into the out-of-plane ferromagnetic state. For this reason it can be hard to distinguish between these two effects from experimental data on domain walls. Figures 2.5(d) to (f) show the TMR contrast associated with different tip magnetization directions. With a fully out-of-plane tip sensitivity (Fig. 2.5(d)) the oppositely pointing magnetic domains are clearly recognizable, while the walls are only visible as areas with intermediate contrast level between domains. On the other hand, a tip with an in-plane component in the same

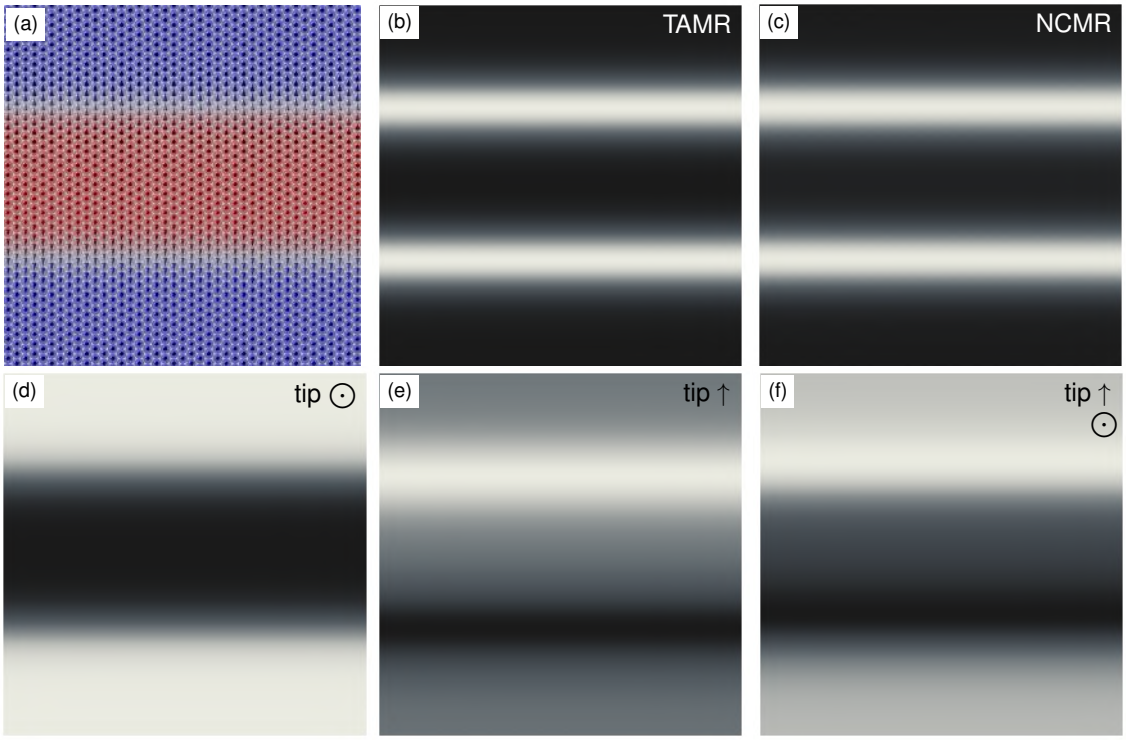

Figure 2.5: (a): Schematic spin configuration (top view) for two Néel domain walls with anticlockwise rotational sense. The colour coding follows the one of Figs. 2.1 and 2.2. (b), (c): Corresponding TAMR and NCMR simulated contrast, assumed to be positive, i.e. the signal on the domain walls is larger than on the magnetic domains. A negative contrast would have resulted in a darker contrast for the walls than for the surrounding domains. The sign and intensity of such contrast depends on the details of the system's LDOS. (d) to (f): Simulated TMR contrast on the two domain walls with a fully out-of-plane (d), fully in-plane (e) and canted (f) magnetic tip. The tip direction is indicated on the top right corners.

direction of the wall propagation direction (Fig. 2.5(e)) allows to distinguish the two walls, possessing oppositely pointing in-plane magnetization, whereas the magnetic domains appear all identical. In general a magnetic tip might have a magnetization direction which is neither fully out-of-plane nor in-plane oriented. In this case it is sometimes said that the tip magnetization direction is canted, and with such a tip it is possible to obtain information on different sample magnetization components simultaneously, as seen in Fig. 2.5(f): the in-plane direction of the walls is still clearly distinguishable, but additionally the oppositely pointing domains have slightly different contrast levels.
Figure 2.6(a) shows now the spin structure corresponding to two magnetic skyrmions with different diameters. The simulated TAMR and NCMR signals (Figs. 2.6(b) and (c)) are still very similar for the large skyrmion, but present a significant difference for the small skyrmion. At the center of both skyrmions the spins are pointing in

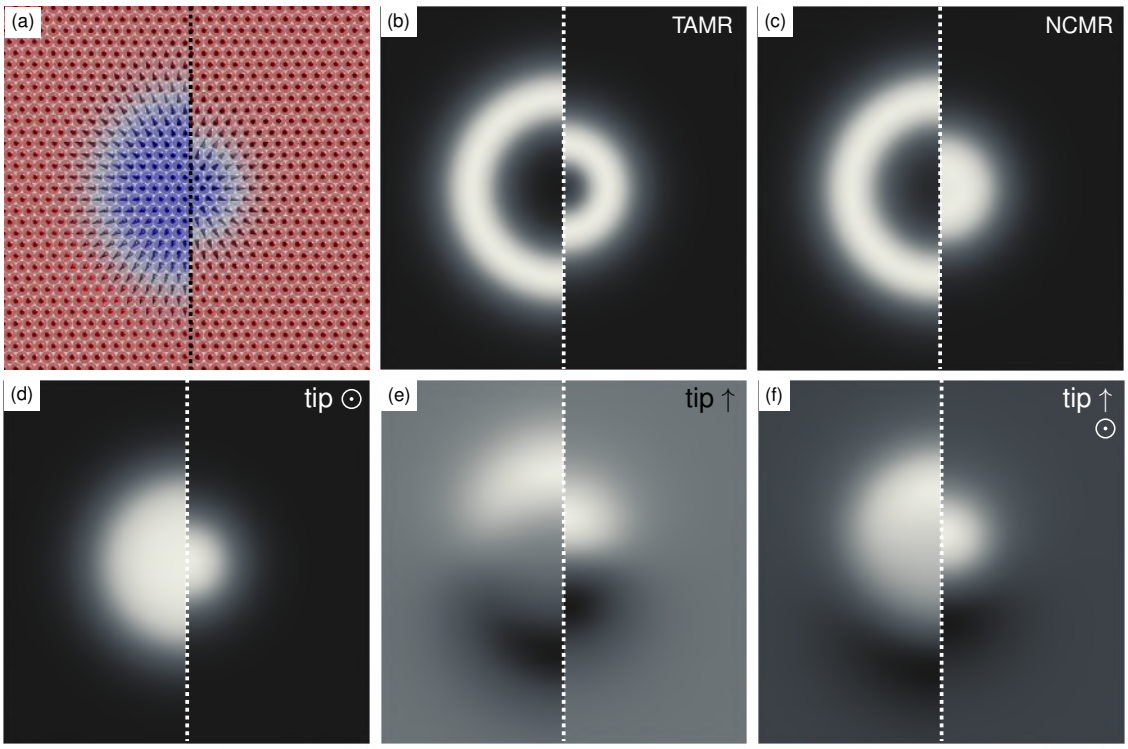

Figure 2.6: (a): Schematic spin structure (top-view) for two Néel skyrmions with 4 nm (left) and 1.8 nm (right) diameters. The colour coding follows the one of Figs. 2.1 and 2.2. Whereas the simulated TAMR signal (b) for the two skyrmions is similar, resulting in a ring-like object, the NCMR signal (c) is larger at the center of the small skyrmion, due to the higher non-collinearity, thus resulting in a very different contrast for the two objects. (d) to (f): Simulated TMR signal for different tip magnetization directions, indicated in the top right corners.

the out-of-plane direction, resulting in a similar TAMR signal outside and at the center of the two objects. However, while in the large skyrmion the spins at the center are mostly collinear, in the small skyrmion they have larger nearest neighbour angles, producing an NCMR signal at the skyrmion center which allows to distinguish it from the ferromagnetic background [17]. Such difference between TAMR and NCMR contrasts for small skyrmions will be used in Chapter 4 as an indication of a NCMR-type electronic contrast on different non-collinear structures in Rh/-Co/Ir(111). Figures 2.6(d) to (f) display the same skyrmions imaged via simulated TMR contrast using the same tip orientations assumed in Figs. 2.5(d) to (f).

2.3 Experimental details

The STM measurements reported in this thesis, as well as the various steps in the sample preparation procedure, are carried out in ultra-high-vacuum (UHV) condi-

tions, with typical vacuum pressures on the order of 1×10^{-10} mbar. A typical set-up consists of several chambers, equipped with different devices necessary for the sample preparation and characterization, and connected together through valves that can isolate chambers during specific operations. The main sample preparation steps, as well as an overview of the STMs used in this work, are described in the following Section.

2.3.1 Sample preparation

In this thesis two different substrates have been used, namely Ir(111) and Pt(111), which come as high purity single crystals with typical size: 7 mm$\times$5 mm$\times$1 mm. The crystals are bound on a 1-mm-thick W sample plate using thin W wires, which keep the sample fixed during the STM measurements. The sample plate is then used to transport the crystal between the different chambers. The procedure necessary to obtain a clean surface is strongly dependent on the material being used. For both Ir(111) and Pt(111) the first step consists in sputtering the surface with Ar^+ ions. The ions are accelerated with a voltage between 700 V and 800 V and directed towards the sample surface. In this way several layers of material, which might have been in contact with air or with other contaminants in the UHV system, are removed, and the obtained surface is composed of substrate atoms which had previously been in the bulk of the crystal.
The obtained surface is rough, and an additional step, usually called annealing, is necessary to achieve atomically flat areas. The crystal is bombarded with high-energy electrons (typically accelerated at voltages between 500 V and 1000 V) and heats up consequently. The desired temperature to be reached, as well as the duration of the bombardment, depends on the specific material. For Ir(111) typical values are around 1500 K for 60 seconds, while for Pt(111) the sample is kept at a temperature around 800 K for 5 to 10 minutes. After the annealing the sample temperature drops exponentially over time and approaches room temperature: this means that faster or slower transfers of the samples between the chambers are necessary to have the desired sample temperature during the deposition of the materials to be studied. In this thesis Co has been deposited on both substrates, and in the case of Co/Ir(111) an additional layer, either Pt or Rh, has also been grown on top of Co.
Another step is sometimes necessary to get rid of carbon impurities. The procedure, referred to as oxygen annealing, consists in heating the sample in an O_2-rich atmosphere, with O_2 partial pressures between 1×10^{-6} mbar and 1×10^{-7} mbar. At certain temperatures the C impurities at the surface react with the O_2, producing CO and CO_2 which desorb from the surface. The remaining oxygen on the surface is removed by an additional annealing procedure, to be performed once most of the oxygen has been removed from the chamber. Several cycles of this procedure can help reducing the C contamination of the crystals. Figure 2.7 shows the surface of a clean Ir(111), which exhibits atomically flat terraces with a step height of one atomic

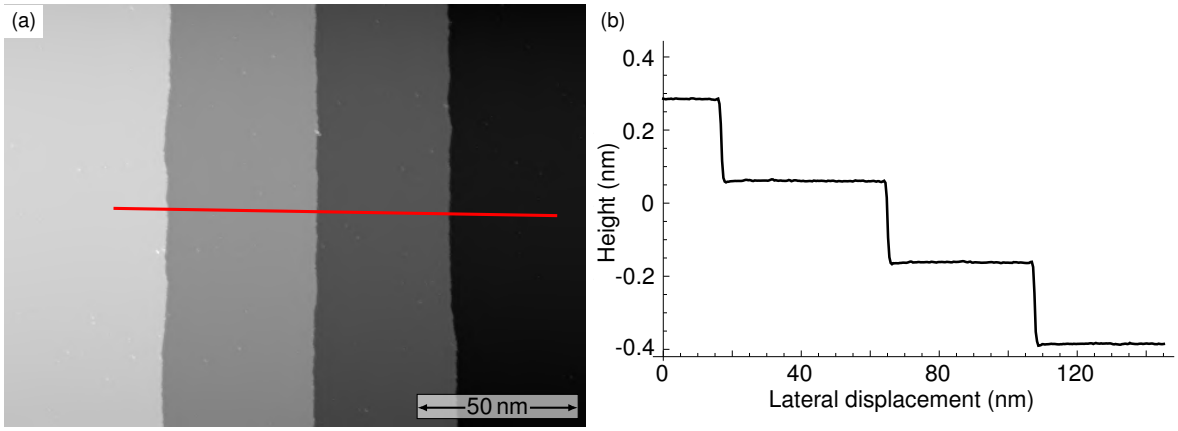

Figure 2.7: (a): STM constant current map of an Ir(111) surface after the cleaning procedure described in the text, displaying flat terraces and atomic steps between them. The line profile indicated by the red line is plotted in (b). *Measurement parameters*: -400 mV, 1 nA, 4 K, Cr bulk tip

layer.
Once the surface is clean, Co, as well as Pt and Rh afterwards, are deposited using molecular beam epitaxy, which allows the controlled growth of atomically thin films, as well as the deposition of single atoms. The evaporant material, usually coming from a high-purity rod, is heated by electrons coming from a tungsten filament, and the obtained flux of atoms is directed towards the sample surface. The material that arrives on the sample surface can organise itself in different ways, depending on its impinging energy, as well as on the sample temperature. At higher substrate temperatures the atoms have more energy and typically diffuse to the closest step edge, where they find bonding sites with higher coordination number (the number of bonds it can form with the substrate). This results in the so-called step-flow growth mode [79], and usually allows to achieve a layer-by-layer growth. A disadvantage of high-temperature deposition is the increased chance of intermixing between the sample and the evaporant, since the higher energy can allow the deposited atoms to penetrate below the surface. This can result in atomic films consisting of substrate atoms and evaporated atoms alloyed together. To reduce such an effect the evaporation can be performed at lower substrate temperatures, which favours, especially in the case of large terraces, the nucleation of islands, rather than of a uniform layer growing from the step edge. Increasing the amount of deposited material can result in the nucleation of higher atomic layers side by side with uncovered areas of the substrate surface. For this reason, this approach might not be optimal for the growth of extended uniform films. Therefore, tuning the deposition parameters and the substrate temperature is a fundamental step to obtain samples with the desired properties. For the experimental set-up used in this thesis typical deposition rates for Co and Rh are between 0.1 and 0.2 monolayers per minute; Pt grows at a lower rate, around 0.03 monolayers per minute, presumably because of

the lower diameter of the evaporant rod, which results in a lower flux of atoms.

2.3.2 Scanning tunnelling microscopes

The largest part of the results of this thesis has been obtained in a multi-chamber UHV system, with dedicated chambers to perform the necessary sample preparation steps, two low temperature STMs and a room temperature STM. The latter has been mostly used to characterize the growth of the materials on the desired substrate, while the low temperature microscopes have been used for the SP-STM measurements. Room temperature SP-STM can also be performed, if the Curie temperature of the sample allows it, but it is generally harder to obtain tips with stable magnetization, due to the larger thermal fluctuations. Each low temperature microscope is thermally anchored to a bath cryostat, which also contains superconducting coils that can generate magnetic fields in the out-of-plane direction. The cryostats are typically filled with liquid He, which brings the coils into the superconducting state and thus allows the flow of large dissipationless currents, necessary to reach the desired magnetic field values. The maximum value of magnetic field that can be applied, as well as the base temperature that the sample can reach, depends on the specific design of the STM: for the two aforementioned systems such values are 2.5 T, $\sim$ 8 K [80], and 9 T, $\sim$ 4 K. One experiment presented in Chapter 3 has been performed in a different UHV system, with an STM equipped with three coils, allowing to apply a magnetic field in any direction, with a base temperature of $\sim$ 5 K [81].

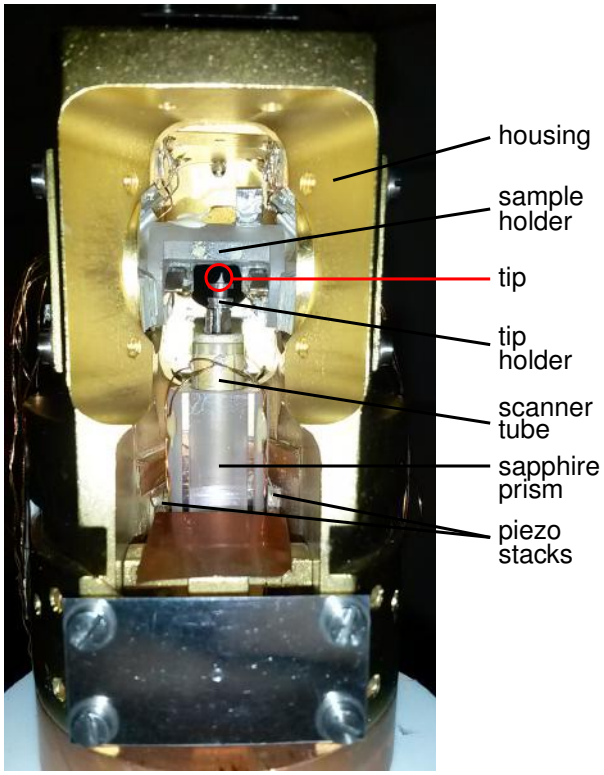

Figure 2.8: Photography of the STM head from the STM described in [81]. A scanner tube hosts the tip holder and moves the tip above the sample surface. The scanner is glued to a sapphire prism. Several piezoelectric stacks glued to the STM housing allow to move rigidly prism and scanner farther and closer to the sample. In this STM the sample holder can be rotated using piezoelectric stacks as well: this allows to expose the sample surface to a flux of atom from an evaporator mounted in the chamber, and thus to deposit single atoms on the cold sample.

The design principle of the three presented STMs is very similar, and briefly described here. The position of the STM tip is controlled by a piezoelectric scanner, to which the tip is attached. Such scanner consists of a tube whose inner and outer surfaces are divided into five electrodes: four electrodes are symmetrically located on the outer surface, and the fifth one covers the whole inner surface. By applying high voltages between the electrodes the tube can be bent or elongated with very high precision, allowing for the movement of the tip above the sample surface, both laterally and perpendicularly to it. The scanner tubes used for these STMs can extend in the z direction by an amount on the order of hundreds of nanometers. To bring the tip within such close distance to the sample surface an additional step is required. Tip and scanner tube are rigidly glued to a sapphire prism, which is in contact with piezoelectric stacks. By applying a high voltage between such stacks and the electrical ground, the prism can be moved closer or farther away from the sample thanks to a slip-stick mechanism [82]. In this way tip and scanner can be brought closer to the surface, up to the point where extending the scanner tube is sufficient to reach the desired tunnelling conditions. Figure 2.8 shows a picture of an STM head, where all the main components described above are visible.
To image magnetic structures via TMR it is necessary that also the tip has a magnetic moment (see Section 2.2.2). This usually means either using non-magnetic tips which are coated with a magnetic film, or using tips made of a magnetic material. In this thesis the STM tips which have been used are made of bulk chromium. This material is antiferromagnetic below room temperature, presenting the advantage of smaller stray fields at the sample surface compared to bulk ferromagnetic tips. Large tip stray fields can produce unwanted modifications of the magnetic structures being imaged, and for many SP-STM experiments low stray fields are therefore preferable. While in a symmetric environment the net magnetic moment of an antiferromaget is negligible, in an STM tip what determines the magnetic sensitivity is the state of the atom located at the tip apex [69]. Such state can be modified by applying moderate voltage pulses (typically between 1 V and 10 V for fractions of a second), which can rearrange the state of the apex atom, or the whole atomic configuration at the tip apex if the bias is large enough. In this way the same magnetic structure can be imaged using different tip sensitivities, obtained by changing apex atom states. Additionally, the state of these tips is typically not modified by magnetic fields because of the antiferromagnetic ordering. This allows to study the changes in the sample's magnetic structure upon application of external magnetic fields while having a fixed magnetic sensitivity of the STM tip.

Chapter 3

Magnetic properties of epitaxial Co films on Ir(111) and Pt(111)

This Chapter presents an investigation of the properties of extended Co films deposited on Ir(111) and on Pt(111). SP-STM reveals for both systems the presence of large out-of-plane magnetic domains separated by nanometer-sized domain walls, the latter ones possessing a unique sense of rotation, emerging from the DMI at the Co/Ir and Co/Pt interfaces. In the case of Co on Ir(111), the effect of a Pt film on top of the Co is also studied, to investigate whether the additional layer significantly modifies the magnetic structures, and whether it helps stabilizing non-collinear spin structures, as already reported in previous works on magnetic multilayers [30, 83]. Part of the results obtained on Co on Ir(111) constitute part of a joint publication with colleagues from the University of Kiel, who have modelled theoretically some of the systems investigated here, thus allowing a comparison of the experimental findings with predictions from density functional theory (DFT) [84]. Some of the results regarding Co on Pt(111) form part of a publication [85] where the properties of magnetic domain walls are investigated for different ultrathin films patterned by strain relief, namely Co/Pt(111) and Ni/Fe/Ir(111). The Chapter also provides additional unpublished results.

3.1 Previous works

3.1.1 Co/Ir(111): ferromagnetic nanoislands

The growth and the magnetic properties of Co monolayer nanoislands on Ir(111), where a monolayer denotes a one-atom-thick layer, have already been studied using SP-STM [86]. They grow mostly pseudomorphically on the Ir(111) surface despite the 8% lattice mismatch between the two materials. Occasional dislocation lines relieve the strain between Co islands and substrate. The film grows both in isolated triangular islands and from the Ir step edge, in this second case forming Co wires with same height as the Co islands. No gap is visible between the Ir step

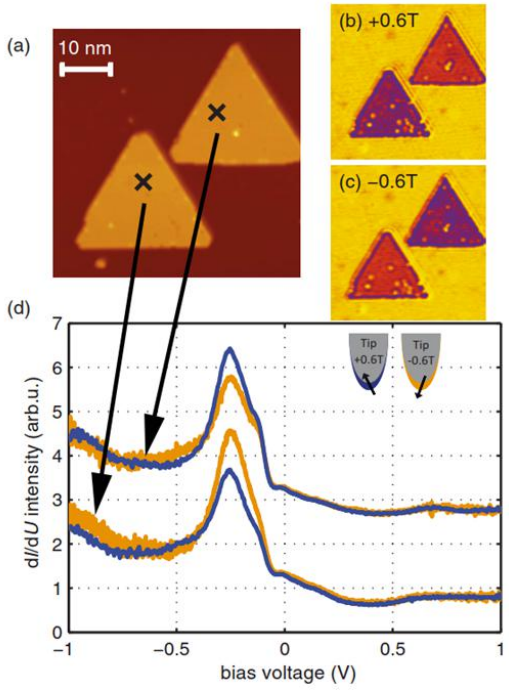

Figure 3.1: (a): Constant-current map of two Co triangular islands on Ir(111). (b), (c): Spin-polarized differential conductance maps of the same two islands as in (a) using a Fe/W tip, taken at B=±0.6 T. (d): Spin-polarized spectra taken at the positions indicated in (a), with different tip magnetization directions. The spectra for one island are offset for clarity. *Measurement parameters*: -250 mV, 2 nA, 6 K, Fe/W tip. Taken from [86] with permission.

edges and the Co wires growing from them, indicating that the wires follow the stacking of the Ir(111). Additionally, when the Co islands and the Co wires coalesce together no dislocation lines or height changes are observed. Since they also show edges along the same close-packed directions, is was concluded that both Co islands and wires grow in only one stacking, namely fcc, which is the one induced by the Ir substrate. The magnetic properties of the nanoislands were investigated using a Fe-coated W tip, whose magnetization direction can be changed by applying a magnetic field. Figure 3.1(a) shows the constant-current map of two Co islands on Ir(111), while Figs. 3.1(b) and (c) show the corresponding $\mathrm{d}I/\mathrm{d}U$ maps at two opposite values of an out-of-plane magnetic field, revealing a two-level contrast on the Co which reverses with the magnetic field. This is also visible in Fig. 3.1(d), which shows spectroscopy measurements taken on the two islands at different values of magnetic field. The peaks visible at -260 mV have a different intensity on the two islands. When the tip direction is inverted, the intensities of the peaks reverse. Such inversion of the islands' contrast with the magnetic field proves that the origin of the contrast is magnetic and not electronic. Since the tip is out-of-plane magnetized, following the applied field, and since the islands' magnetization direction does not

change at such small fields, it was concluded that the Co islands are then single domain ferromagnetic, with an easy magnetization axis normal to the sample surface. By applying large out-of-plane magnetic fields, it was shown that such islands have a magnetic coercivity of more than 4 T, and at least 5 T are necessary to reach magnetic saturation of the sample.

3.1.2 Co/Pt(111): reconstructed films with out-of-plane anisotropy

Several studies have already investigated in detail the growth of Co atomic layers on a Pt(111) surface [87, 88]. Due to the lattice mismatch of 9.4% between the two materials, the Co monolayer does not grow pseudomorphically on the sample surface. In order to relieve the tensile strain, it creates instead an irregular reconstruction pattern made of areas in which the Co atoms are located on either the fcc or the hcp hollow sites, separated by lines of atoms located on bridge sites (see Fig. 3.2). Such bridge lines create triangles pointing in two different directions: areas delimited by triangles in the two directions correspond to fcc- and hcp-stacked Co. The Co fcc areas are found to be significantly larger in size, indicating that the fcc stacking is energetically favourable. Higher Co layers relieve the strain by producing a hexagonal Moiré pattern, which persists without modifications up to 5 Co monolayers [87].

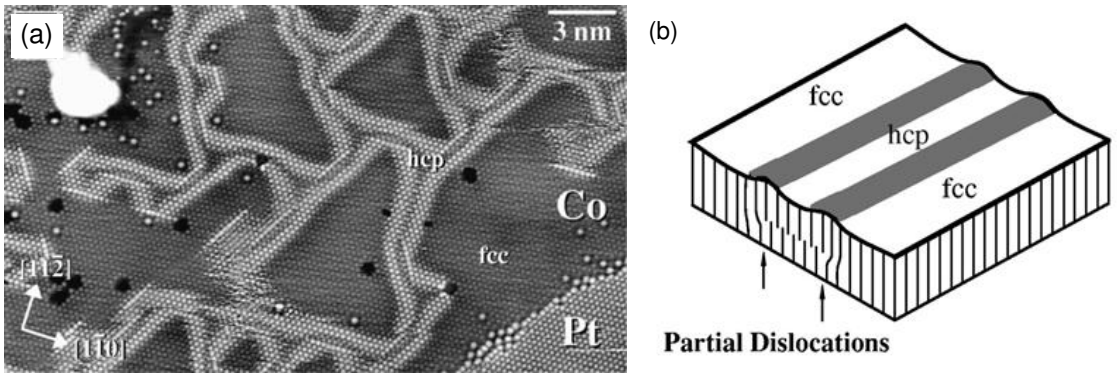

Figure 3.2: (a): STM constant-current map with atomic resolution of a monolayer Co film deposited on Pt(111). The Co fcc areas are significantly larger than the Co hcp ones, and the two are separated by bridge lines. (b): Sketch of two dislocation lines separating differently stacked Co areas. Taken from [87] with permission.

The magnetic properties of isolated monolayer and double layer Co islands on Pt(111) have also been previously studied using SP-STM [89, 90]. It has been shown that the two-levels $\mathrm{d}I/\mathrm{d}U$ contrast visible on the Co islands changes upon the application of out-of-plane magnetic fields, indicating that the film is out-of-plane ferromagnetic. At the low Co coverages which have been investigated, only rarely are domain walls visible.

3.2 Growth of extended Co and Pt/Co films

The above mentioned SP-STM studies have limited themselves to mostly isolated Co islands, which are single domain ferromagnetic and separated from each other by areas without any magnetic material, without the need for the system to create magnetic domain walls. If the magnetic Co film extends continuously over larger areas, magnetic structures with opposite magnetization might now be separated more often by domain walls, as the areas of bare Ir or Pt decrease in size. This could allow to study more extensively the properties of such non-collinear magnetic objects. This Section presents the study of the growth of Co extended films, up to several monolayers in coverage, on both Ir(111) and Pt(111). Additionally, the growth of a Pt layer on top of a Co/Ir(111) is investigated.

3.2.1 Co growth on Ir(111)

Extended Co areas on Ir(111) are prepared by evaporating Co on the clean Ir substrate, between 6 and 8 minutes after the annealing of the crystal, when its temperature is around 100 °C (see Section 2.3.1 for details on the cleaning procedure).
Figure 3.3 shows the growth up to four atomic layers of Co on Ir(111). The Co monolayer grows mostly pseudomorphically from the step edges (Fig. 3.3(a)), with occasional reconstruction lines to relieve the film strain due to the lattice mismatch. Some of these lines are indicated by the red arrow. The Co double layer (Fig. 3.3(b)) exhibits a reconstruction pattern consisting of mostly triangular areas, separated by bridge lines. The triangles formed by the bridge lines are oriented in two different directions, and at specific bias voltages they show a different apparent height in constant-current maps. This suggests that they correspond to fcc and hcp Co areas. The reconstruction pattern is similar to the one observed in Co/Pt(111) [87, 89] and in Ni/Fe/Ir(111) [91] (see Fig. 3.3(d) for a closer view). Higher layers of Co on Ir(111) are reconstructed as well (Fig. 3.3(c)), and present a more regular structure which arranges itself partly following a hexagonal symmetry, as seen in Figs. 3.3(e) and (f). In (e) it is also possible to observe a different topographic signal for the up-pointing and down-pointing triangular areas, corresponding to differently stacked Co areas. As the coverage increases, the various Co layers can arrange themselves in different combinations of fcc and hcp stackings: assuming a uniform fcc stacking for the Co monolayer, each additional Co layer can grow in either fcc or hcp on top of the previous one, thus creating several differently stacked Co areas, which are usually separated by stacking fault lines. One such line is indicated by the red arrow in Fig. 3.3(f) for an area with four Co layers. The reconstruction pattern of Co triple and quadruple layers is similar to the ones observed in the double layer Co on Pt(111) after a post-annealing procedure [88, 90].

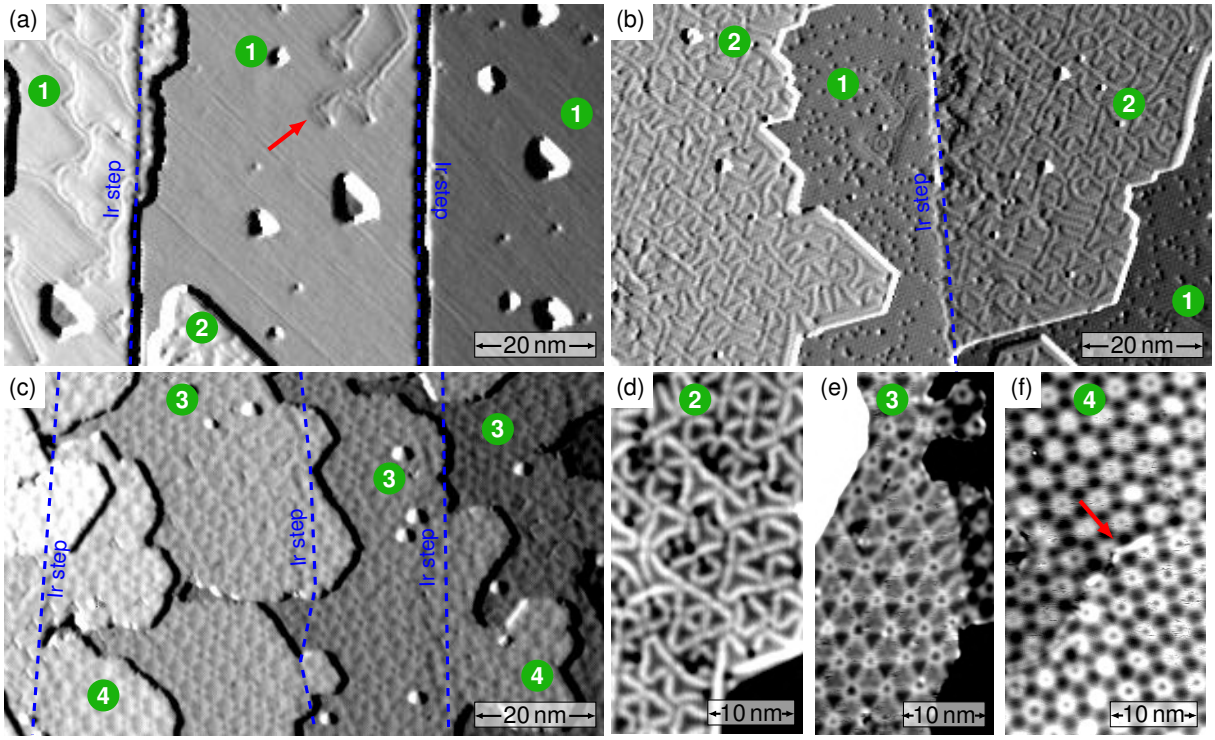

Figure 3.3: (a), (b), (c): STM constant-current maps of different amounts of Co deposited on Ir(111), from one monolayer up to four (indicated by the green circles). The derivative of the height signal has been added to the height signal to increase the visibility of the structure details. The red arrow in (a) indicates a few reconstruction lines on the Co monolayer. (d), (e), (f): Closer views of the reconstruction patterns for Co double, triple and fourth layers. The structure becomes increasingly more symmetric as the Co coverage increases. The red arrow in (f) indicates a stacking fault line. *Measurement parameters*: (a): -200 mV, 750 pA, 78 K; (b): -450 mV, 750 pA, 8 K; (c): -450 mV, 1 nA, 8 K; (d): -650 mV, 750 pA, 8 K; (e), (f): -50 mV, 1.5 nA, 8 K. All images measured with a Cr bulk tip.

3.2.2 Co growth on Pt(111)

Large areas of Co on Pt(111) are prepared by evaporating Co from a high purity rod on the clean Pt substrate, which is at room temperature in order to reduce the amount of intermixing between the two materials. Figure 3.4 shows the growth of the first two layers of Co on Pt(111), both layers displaying a reconstruction pattern. The double layer grows in extended patches before the monolayer is completed, leaving areas of Pt(111) uncovered. The inset displays a closer view on the reconstruction pattern of the Co monolayer.
Increasing the Co coverage results in a more complex arrangement of Co layers, as shown in Fig. 3.5(a). Contrarily to what is observed for Co/Ir(111), where a full Co monolayer could be achieved easily by tuning the amount of deposited material, here even at high Co coverages there are still Pt areas which remain uncovered.

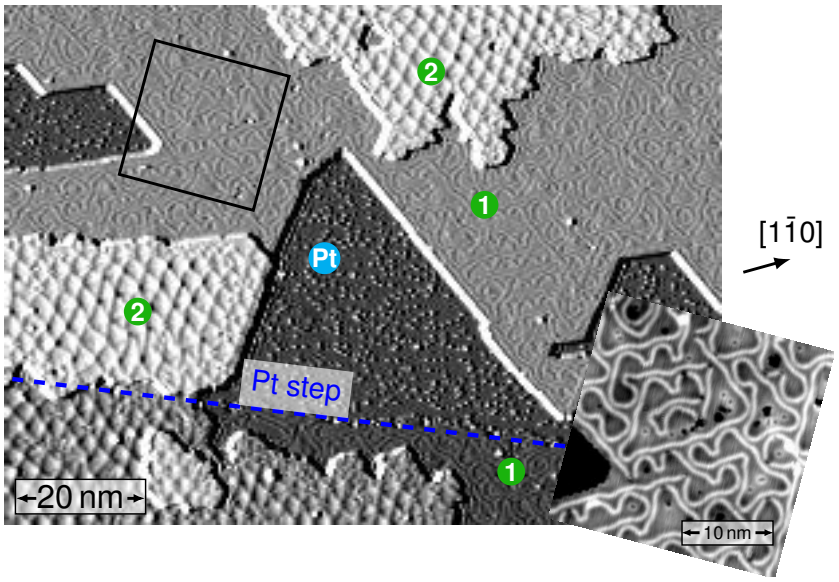

Figure 3.4: STM constant-current map of a Co/Pt(111) sample. The coverage corresponds to 1 atomic layer, and there are areas of Co monolayer and double layer. The differentiated topography has been superimposed to the topographic signal to improve the visibility of the surface features. Both the Co monolayer and double layer show a complex dislocation network. The inset shows the details of the monolayer dislocation network. *Measurement parameters*: 1 nA, 4 K, Cr bulk tip, main: -250 mV, inset: -1 V. Adapted from [85].

On the other hand, the vast majority of Co monolayer areas are already covered by double layer areas. The different growth of Co on the two surfaces is attributed to the different substrate temperature, as higher temperatures favour a layer-by-layer growth of the films [79, 92].
At specific bias voltages it is possible to observe changes in $\mathrm{d}I/\mathrm{d}U$ contrast across the same Co layers. Areas with different contrast are usually delimited by sharp edges mostly following the close-packed directions of the surface. This produces a variety of $\mathrm{d}I/\mathrm{d}U$ contrast levels, as visible in Fig. 3.5(b), which do not correlate with the magnetic signal visible in Fig. 3.5(c) for the same area, at a different bias (see Section 3.3 for more details on the magnetic properties). The origin of such contrast can therefore be explained as originating from differently stacked Co films. As already seen in high Co layers on Ir(111) (see Section 3.2.1), Co layers growing on top of each other can arrange in a variety of combinations of fcc and hcp stackings, each combination resulting in slightly different electronic properties, visible in $\mathrm{d}I/\mathrm{d}U$ maps taken at specific bias voltages. Figures 3.5(d) and (e) offer a closer view on 2 differently stacked Co double layer areas. No clear difference between the left and right part of the image is visible from the constant-current map, and the only change in the reconstruction pattern is in correspondence of the stacking fault line, located on a constriction (see red ellipses). In the $\mathrm{d}I/\mathrm{d}U$ map, however, the difference between

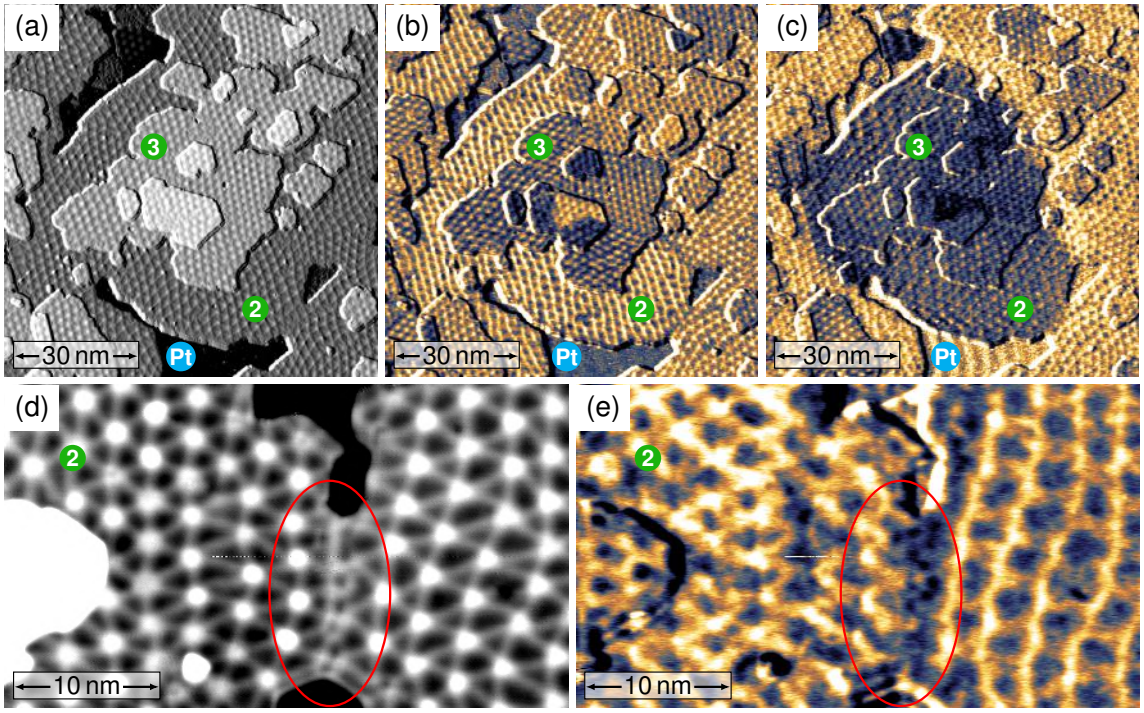

Figure 3.5: STM constant-current (a) and $\mathrm{d}I/\mathrm{d}U$ (b) maps of about 2.3 monolayers of Co on Pt(111). In (a) the derivative of the signal has been superimposed to the height signal to increase the visibility of the reconstruction pattern. The Co double layer grows in extended areas, while still leaving small Pt patches uncovered. Some triple layer areas are also visible. For Co layers above the first one, areas with different $\mathrm{d}I/\mathrm{d}U$ contrast are identifiable, corresponding to differently stacked layers. (c): $\mathrm{d}I/\mathrm{d}U$ map, now with out-of-plane spin sensitivity, of the same area of (a) and (b). The position of the observed dark magnetic domain wall does not correlate with the contrast levels in (b), and thus allows to exclude a possible magnetic origin for them. (d), (e): STM constant-current and $\mathrm{d}I/\mathrm{d}U$ maps of a small area of Co double layer on Pt(111). The dislocation network is perturbed at the film's constriction, where a stacking fault line is located. The line separates Co double layer areas with different $\mathrm{d}I/\mathrm{d}U$ contrast. *Measurement parameters*: 4 K, Cr bulk tip, (a), (b): 350 mV, 1 nA; (c): -850 mV, 500 pA; (d), (e): 250 mV, 500 pA.

the two areas becomes more evident, as the $\mathrm{d}I/\mathrm{d}U$ signal produced by the two reconstruction patterns is slightly different.
The reconstruction pattern follows a hexagonal symmetry, but is not perfectly regular, as it could be expected for a Moiré pattern. The partially disturbed reconstruction network is similar to the misfit structure observed for Co double layers on Pt(111) after a post-annealing procedure [88, 90]. According to [88], such misfit structure is a consequence of a gradual change in the lattice constant from the Pt substrate to the Co double layer, which could be caused by a certain degree of intermixing between the first Co layer and the Pt. Contrarily, a Moiré pattern is usually

caused by an abrupt change in the lattice constants between layers. Therefore, the presence of this misfit structure could be an indication of a residual amount of intermixing between Pt and the Co monolayer in the system, which persists even when the deposition is done at room temperature.

3.2.3 Growing Pt on top of Co/Ir(111)

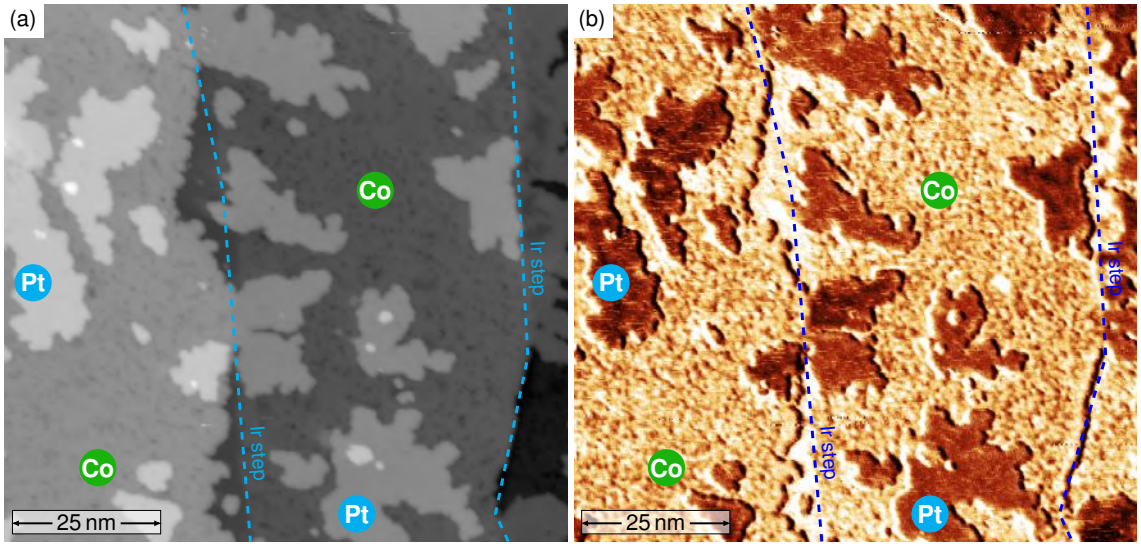

Figure 3.6: STM constant-current (a) and differential conductance (b) maps of a sample of Pt/Co/Ir(111). The Pt islands grow with irregular shape and in both fcc and hcp stackings, as evident from the different contrast levels in $\mathrm{d}I/\mathrm{d}U$. *Measurement parameters*: -450 mV, 800 pA, 8 K, Cr bulk tip.

Pt is evaporated on the Co/Ir(111) film after the Co deposition, approximately 25 minutes after the annealing of the Ir(111) surface. Since the temperature of a sample drops exponentially over time after the annealing, the Ir substrate temperature during Pt evaporation is assumed to be very close to room temperature. Figure 3.6 shows the growth of about 0.3 monolayers of Pt on top of a Co monolayer on Ir(111). Contrarily to Co, Pt does not grow predominantly from the Ir step edges, but instead mostly in small isolated islands with irregular size and shape. At the chosen bias voltage the two materials exhibit a different $\mathrm{d}I/\mathrm{d}U$ signal, which allows an easy identification in a $\mathrm{d}I/\mathrm{d}U$ map. The Pt growth is pseudomorphic, and the $\mathrm{d}I/\mathrm{d}U$ map of Fig. 3.6(b) reveals that the Pt islands possess two different contrast levels, that can be associated with areas of fcc and hcp stacking. The Co layer appears dirtier than in previous preparations without Pt. The exact cause is not clear, however one possible source of contamination could be by-products of the Pt evaporation, such as hydrogen. Alternatively, isolated Pt atoms could get embedded in the Co layer, creating a more inhomogeneous surface.

It is possible to obtain larger Pt islands by increasing the Pt coverage, although they still tend to grow separately from each other, as shown in Fig. 3.7(a). Additionally, small patches of double layer Pt start to appear before the first layer is completed, creating a more complex arrangement of atomic layers. In order to achieve more uniform films, after the Pt deposition the sample is annealed at a temperature around 500 °C. This results indeed in a more uniform growth of Pt on top of the Co monolayer, as visible in Fig. 3.7(b). Now most Pt areas have coalesced and grow from the Ir step edges, and no double layer Pt islands are present anymore. The different $\mathrm{d}I/\mathrm{d}U$ signal for the two materials at the used bias voltages allows to identify them in $\mathrm{d}I/\mathrm{d}U$ maps, and to observe that Pt is indeed on top of the Co and did not move below it as a consequence of the post-annealing, as shown later in the Chapter in Fig. 3.24. The possibility of intermixing between the two materials is discussed at the end of the Section.

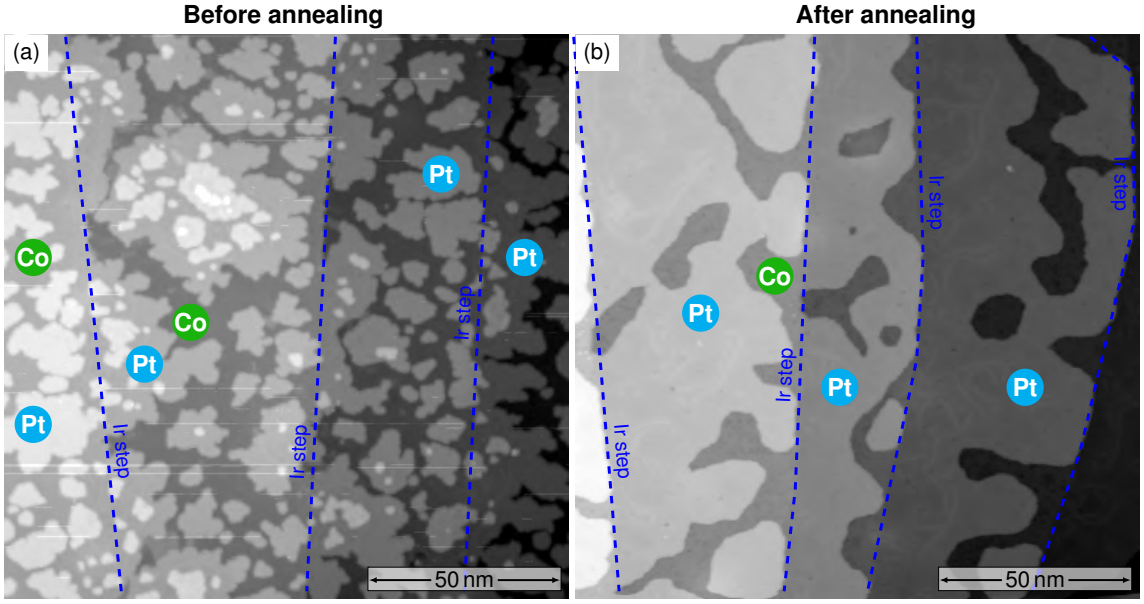

Figure 3.7: STM constant-current maps of a Pt/Co/Ir(111) sample directly after the Pt deposition (a) and after an additional post-annealing procedure at temperatures around 500 °C (b). The Pt film is more uniform after the annealing, with more extended areas of Pt monolayer and no sign of double layer islands. *Measurement parameters*: (a): -450 mV, 500 pA, 300 K, PtIr tip; (b): -450 mV, 800 pA, 8 K, Cr bulk tip.

A similar procedure has been used to try to grow extended areas of Pt on higher layers of Co. Figures 3.8(a) and (b) show the growth of Pt at room temperature on a sample consisting mostly of triple layer of Co. The different materials are easily identifiable from the $\mathrm{d}I/\mathrm{d}U$ map (b), where, at this bias voltage, Pt appears darker than Co. The height signal of the Pt shows a height modulation which resembles a reconstruction pattern, but it is unclear whether the Pt layer is actually reconstructed

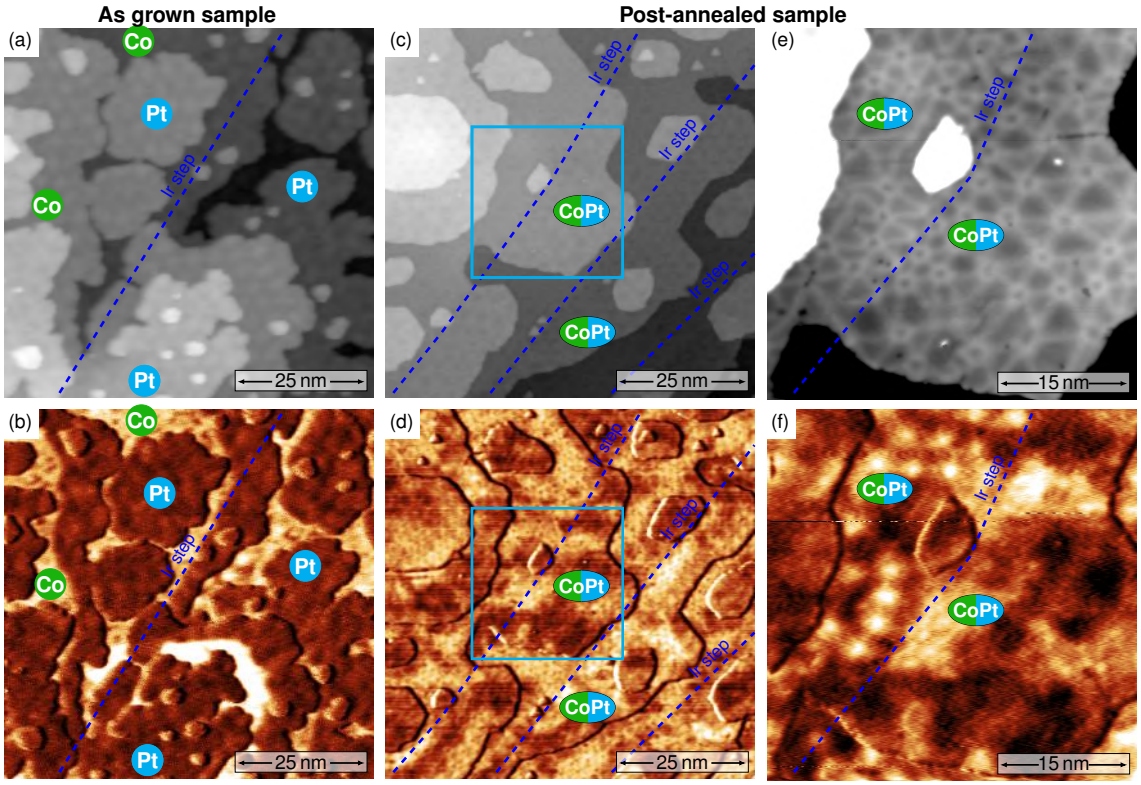

Figure 3.8: (a), (b): STM constant-current and differential conductance maps of about 0.75 monolayers of Pt deposited at room temperature on 3.5 monolayers of Co on Ir(111). The $\mathrm{d}I/\mathrm{d}U$ signal allows to easily identify Pt and Co areas. (c) to (f): STM constant-current and differential conductance maps of 0.6 monolayers of Pt deposited on 3.5 monolayers of Co on Ir(111), with subsequent annealing of the sample at 500 °C. The strong variation of $\mathrm{d}I/\mathrm{d}U$ signal on each layer suggests that Pt and Co are embedded together in the film. The dark $\mathrm{d}I/\mathrm{d}U$ signal associated with Pt is correlated in topography with a distortion of the reconstruction pattern. The blue boxes in (c) and (d) indicate the area imaged in (e) and (f). *Measuring parameters*: (a), (b): -450 mV, 700 pA, 300 K, PtIr tip; (c), (d): -300 mV, 1 nA, 8 K, Cr bulk tip; (e), (f): -450 mV, 1 nA, 8 K, Cr bulk tip.

or if the modulation is due to the reconstructed Co layers below. The amplitude of the modulation on the Co triple layer and on the Pt on top of it is similar and on the order of 20 pm. The effect of post-annealing on a sample with slightly less Pt and the same amount of Co is shown in Figs. 3.8(c) and (d): the obtained layers are more uniform and extended, but the $\mathrm{d}I/\mathrm{d}U$ signal reveals a highly non-uniform contrast in all the layers. Pt and Co, corresponding here to the dark and bright areas in $\mathrm{d}I/\mathrm{d}U$, respectively, are embedded together, and due to the post-annealing procedure they have thus intermixed into a single layer. A closer view (Figs. 3.8(e) and (f)) shows that the reconstruction pattern of the layer is also modified by the intermixing: the triangular areas that normally correspond to fcc and hcp Co are

now greatly extended in size in correspondence to the areas with low $\mathrm{d}I/\mathrm{d}U$ signal, i.e. where presumably the Pt is. Such a distortion of the reconstruction pattern was not observed in uncovered samples with similar amounts of Co on Ir(111). These highly intermixed layers are not ideal to investigate the effects of the Co/Ir and Pt/Co interfaces on the magnetic properties of the films, and therefore they have not been investigated any further. The Pt and the Co layers presented in Fig. 3.7(b) are assumed to be not as heavily intermixed as those in Figs. 3.8(c) to (f), because in $\mathrm{d}I/\mathrm{d}U$ images (see for example Fig. 3.24 in Section 3.3) Pt and Co appear to belong to separate layers with different $\mathrm{d}I/\mathrm{d}U$ signals, contrarily to what is observed in Figs. 3.8(d) and (f). A small amount of alloying due to the post-annealing procedure cannot be excluded, however, it is not so strong as to embed Co and Pt in the same layer. This allows to study the effects of the Pt/Co interface on the magnetic properties of the system.

3.3 Magnetism of Co films

While conventional STM can be used to study the growth of Co films on the different substrates, SP-STM provides information on their magnetic properties. In this Section the properties of both the magnetic domains and the domain walls separating them are investigated.

3.3.1 Magnetic domains

Figure 3.9 shows a perspective view of a Co monolayer film on several terraces of Ir(111), and some small double layer islands are also visible. The image is coloured with the simultaneously measured spin-polarized $\mathrm{d}I/\mathrm{d}U$ signal. Previously measured Co monolayer islands displayed two levels of contrast when imaged with an out-of-plane sensitive magnetic tip [86]. The similar kind of two-level contrast observed here allows to deduce that the tip has a magnetization component along the out-of-plane direction. The magnetic domains extend mostly along the atomic terraces, and are separated by domain walls. The walls are predominantly found in geometrical constrictions, where their length is reduced. This indicates that creating these walls has an energy cost per unit length. Another way to reduce the domain wall energy is to have oppositely pointing domains on adjacent terraces: if the coverage of the magnetic material is exactly one monolayer or below, there are no magnetic atoms connecting the adjacent domains, and therefore no domain wall is created to separate them. In Fig. 3.9 also small islands of Co double layer are visible, which display two levels of $\mathrm{d}I/\mathrm{d}U$ contrast which are correlated to those observed in the monolayer. This provides evidence that the double layer Co is ferromagnetic with out-of-plane anisotropy. A proof of its out-of-plane character is given below, using an out-of-plane magnetic field (see Fig. 3.11). The domain walls visible in Fig. 3.9 do not cross such double layer islands, and are instead often positioned in

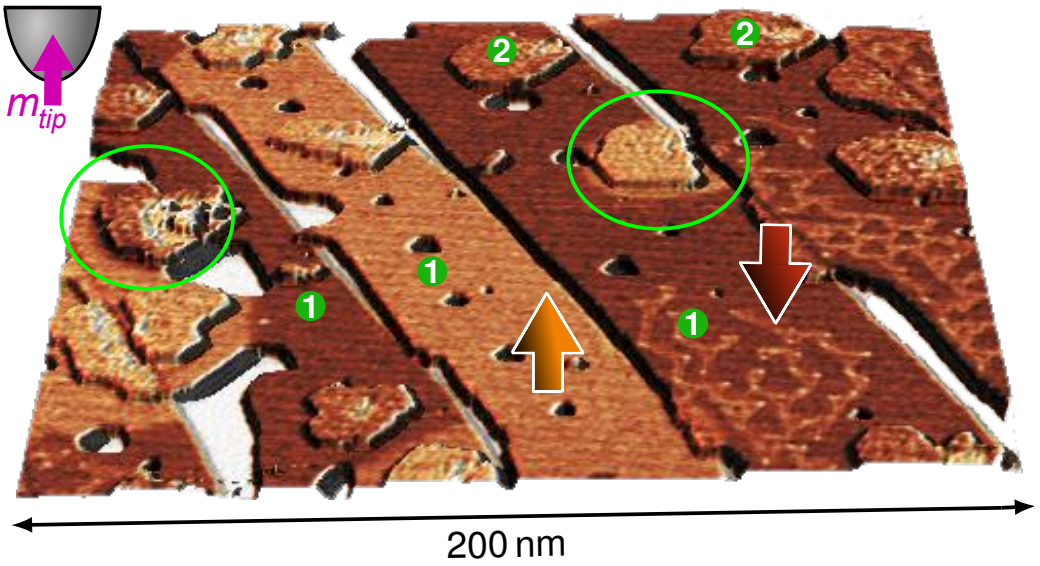

Figure 3.9: Perspective view of the topography of about 1.2 monolayers of Co on Ir(111), coloured with the simultaneously recorded spin-polarized $\mathrm{d}I/\mathrm{d}U$ signal. The arrows indicate two magnetic domains pointing in opposite directions. The ellipses indicate areas where the domain walls avoid the double layer islands by sitting just below them. *Measurement parameters*: -580 mV, 500 pA, 8 K, Cr bulk tip. Adapted from [84].

Co monolayer areas close to them (see ellipses in Fig. 3.9), indicating that the double layer Co has a larger domain wall energy density than the monolayer. This is probably due to an increased exchange stiffness in the double layer due to the higher number of Co nearest neighbours.

As the Co coverage increases above a complete monolayer, the magnetic film becomes fully connected across all the Ir terraces. The local morphology of the sample plays now an important role in determining the size and shape of the magnetic domains, as can be seen in Fig. 3.10. The Figure shows the spin-polarized $\mathrm{d}I/\mathrm{d}U$ maps of two different areas of an almost full double layer Co film on Ir(111). The area in (a) presents a very regular landscape of terraces, all with similar size and direction. Because of this, the magnetic domains present a stripe-like shape, which follows the terrace orientation. Most of the domain walls are located very close to the terrace edges, where small Co monolayer areas are still present, and only rarely does a wall cross the Co double layer (see blue ellipses in Fig. 3.10(a)). On the other hand, the area in (b) shows terraces with smaller and more irregular size, where the Co does not always grow continuously, as shown in the inset. This results in a higher density of terrace edges and constrictions, where domain walls can minimize their energy. For this reason the observed domains have a more irregular shape.

The size of the domains can be modified by applying a magnetic field in the out-of-plane direction, as shown in Fig. 3.11: the bright domain visible in (a) starts to

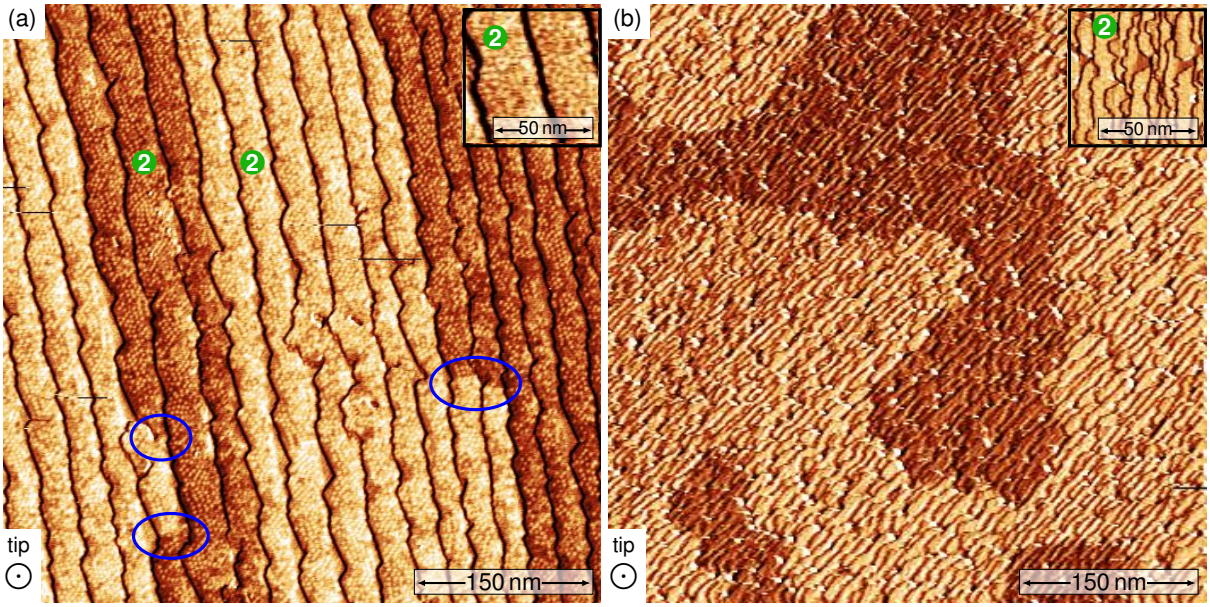

Figure 3.10: Spin-polarized differential conductance of two areas, with same size, of about 2 monolayers of Co on Ir(111). The tip is sensitive to the out-of-plane component of the sample's magnetization. The domains have a shape which is strongly correlated to the topographic details of the sample. The insets offer a closer view on the terrace landscape in the two sample spots. *Measurement parameters*: 1 nA, 4 K, Cr bulk tip, (a): -550 mV, (b): 750 mV.

shrink as +650 mT are applied in the direction perpendicular to the sample (b). This also shows that the Co double layer domains are oriented in the out-of-plane direction. At slightly higher fields the domain splits into two separate objects (c), and scanning over them again produces another change in their shape (d). This is probably caused by a combination of the applied magnetic field and of the tip scanning across the domain: in zero magnetic field the walls remain pinned to terrace edges and constrictions, whereas in the presence of a magnetic field the domains with magnetization parallel (antiparallel) to the field direction tend to grow (shrink), and thus a current-induced depinning of the walls could happen more often.
Depositing even more Co produces a change in the size of the magnetic domains. As the Co coverage reaches the third and fourth atomic layer, it becomes harder using SP-STM to find domains with opposite magnetization. The domain wall density appears to have decreased, as shown in Figure 3.12: there is only one domain wall in an area of 530×330 nm^2, separating two very large out-of-plane domains. This domain wall appears to be less influenced by the morphology of the sample, compared to what is observed for films with less Co. It crosses areas with different Co coverage, without a clear preference for geometrical constrictions, terrace edges or thinner Co layers. This behaviour can be attributed to the smaller change in domain wall energy between higher Co layers. In a simple picture, assuming the same

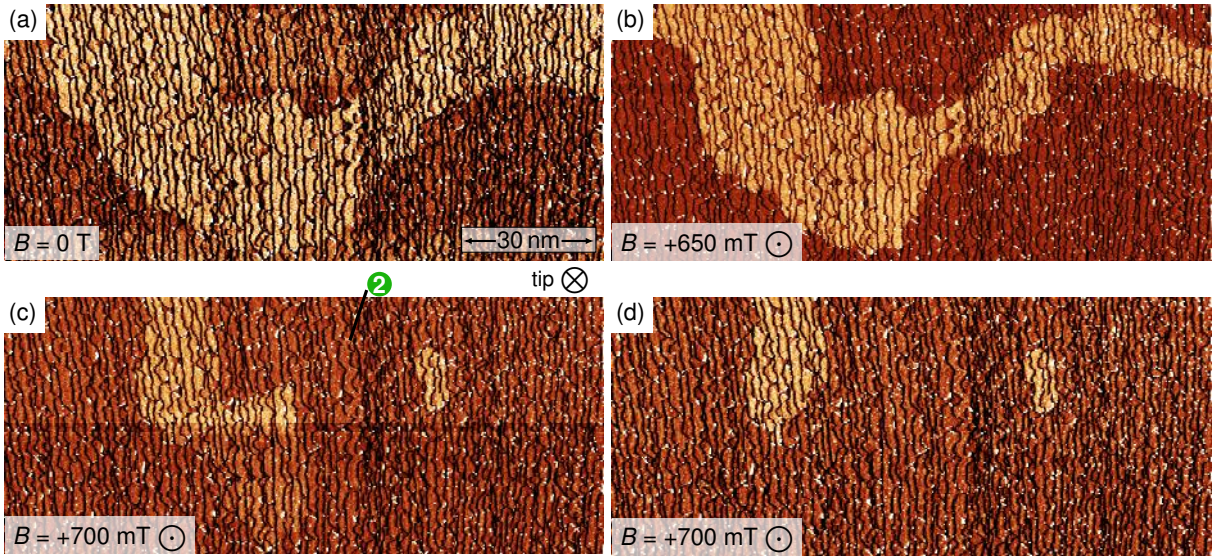

Figure 3.11: Spin-polarized differential conductance maps, with out-of-plane sensitivity, of about 2 monolayers of Co on Ir(111). As the magnetic field increases, the bright domain shrinks in size and eventually splits into two objects. The STM tip favours the domain wall movement and brings the domains into more stable configurations. *Measurement parameters*: 750 mV, 500 pA, Cr bulk tip, 4 K

magnetic parameters, a domain wall in a Co double layer costs twice the energy as compared to a wall in the monolayer, because in the first case the wall is composed by twice the amount of spins. On the other hand, the difference in wall energy between third and fourth Co layer is smaller, resulting in smaller energy penalties for having a domain wall on a higher layer. When taking into account also the changes in the magnetic parameters, it can be expected that the largest changes in magnetic properties should happen at low Co coverages, since at higher coverages the system parameters tend to approach the values of the bulk material, as the contribution of the Ir interface becomes less important.

Figures 3.13(a) and (b) show the topography and magnetic state of Co monolayer and double layer areas on Pt(111), both layers possessing out-of-plane magnetic anisotropy [89, 90]. The two-levels contrast visible in the $\mathrm{d}I/\mathrm{d}U$ map of Fig. 3.13(b) cannot be attributed to stacking differences, as those seen in Fig. 3.5 in Section 3.2.3, because such variations only appear starting from the Co double layer, while here the contrast difference is also visible on the monolayer. It is therefore possible to conclude that such contrast has a magnetic origin, and that the tip has out-of-plane sensitivity. This is further supported by observing that changes in $\mathrm{d}I/\mathrm{d}U$ contrast levels are in correspondence of constriction of the film, where large triangular islands coalesce together (see red ellipses in Fig. 3.13(b)). Such changes in $\mathrm{d}I/\mathrm{d}U$ contrast correspond therefore to magnetic domain walls, which possess a positive energy cost per unit length (similarly to Co/Ir(111)) and are located where such cost is mini-

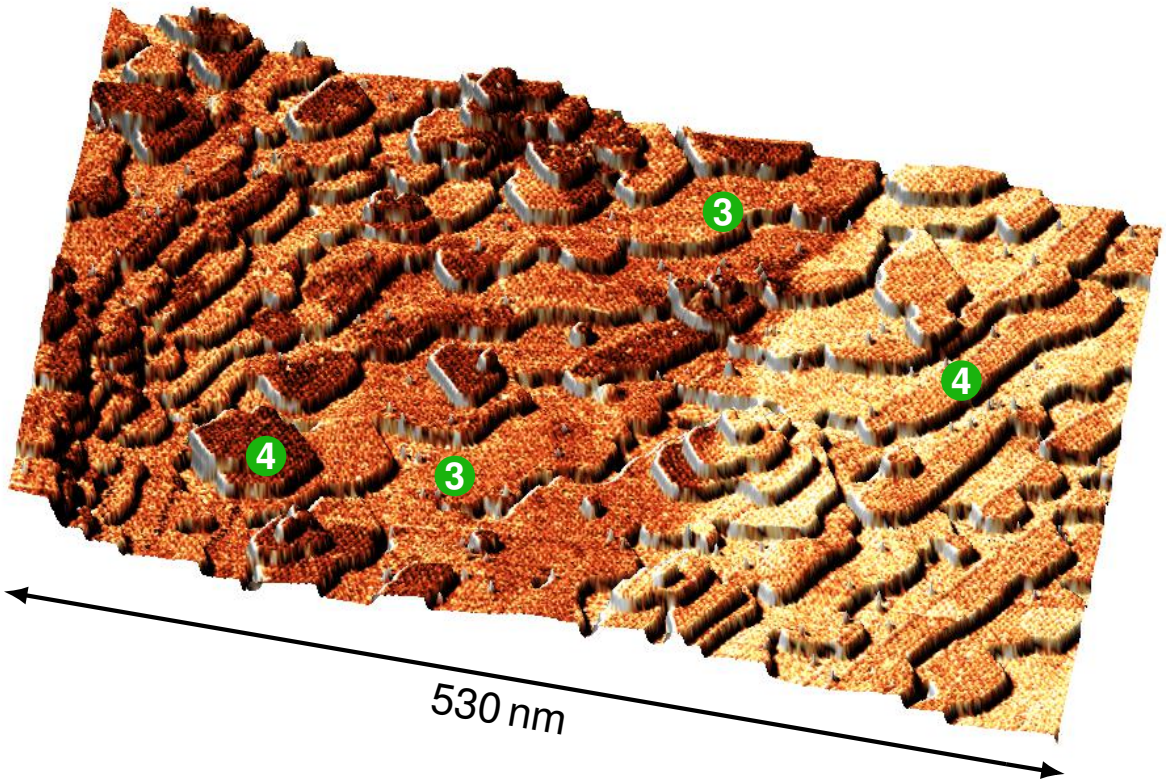

Figure 3.12: Perspective view of the topography of about 3.3 monolayers of Co on Ir(111), coloured with the simultaneously measured spin-polarized $\mathrm{d}I/\mathrm{d}U$ signal. The two domains, corresponding to the bright and dark coloured areas, are fairly large, extending for several hundreds of nanometers. The domain wall dividing them does not seem to be influenced in its path by the sample morphology: it does not follow terrace edges, neither does it avoid crossing higher Co layers. The numbers in the green ellipses indicate the Co layers. *Measurement parameters*: -750 mV, 800 pA, 8 K, Cr bulk tip.

mized. Higher Co layers show a magnetic $\mathrm{d}I/\mathrm{d}U$ signal which is strongly correlated to the one visible on the double layer, see Fig. 3.13(c). This suggests that also the triple layer Co areas observed possess a magnetization in the out-of-plane direction. This is consistent with previous observations of spin reorientation transitions, from out-of-plane to in-plane, for Co coverages between 4 and 10 monolayers, depending on the Co growth conditions [93–96]. The Co does not completely cover the Pt surface even when most areas have a Co coverage of at least two monolayers, and the magnetic film still presents discontinuities. As a result, the shape of the magnetic domains is strongly influenced by the constrictions in the films, where uncovered Pt areas are found (see red ellipses in Fig. 3.13(c)). It was therefore not possible to study the size and shape of the domains as a function of coverage, as done for the Co/Ir(111) system.

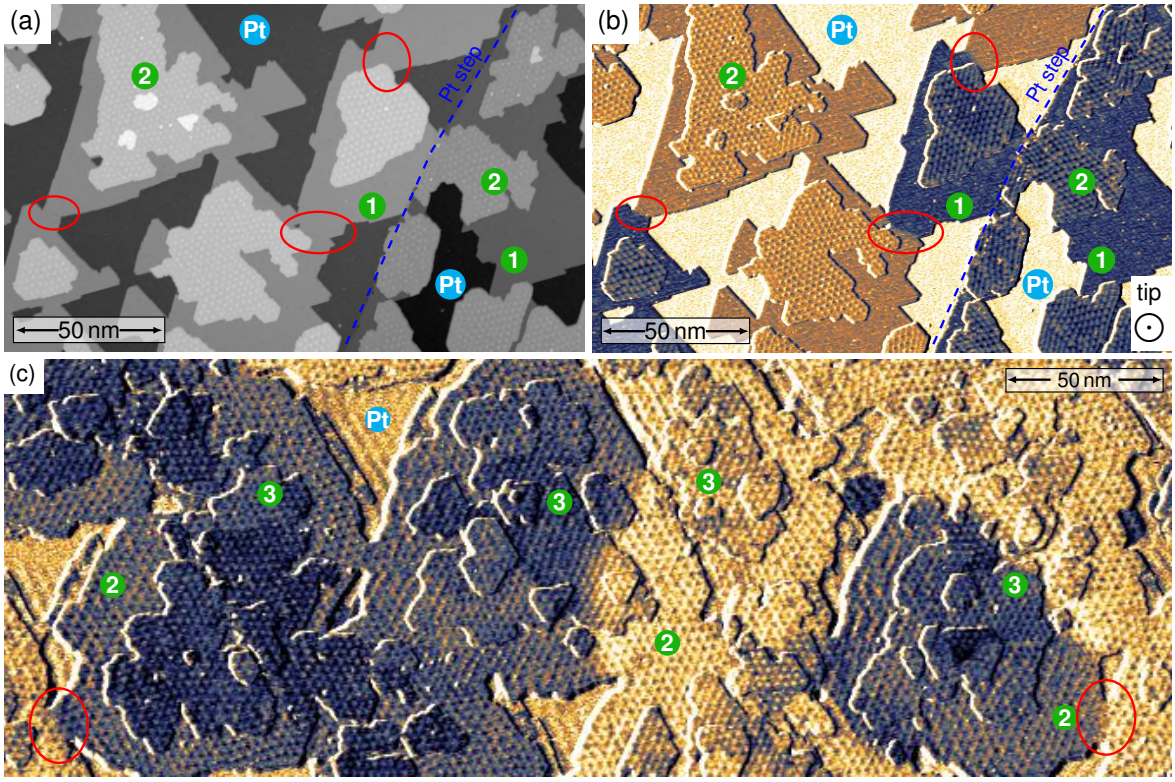

Figure 3.13: STM constant-current (a) and spin-polarized differential conductance (b) maps of about 0.8 Co ML deposited on Pt(111). The tip has out-of-plane sensitivity. Large triangular Co islands are connected together via small coalescence points, where domain walls are often located, in order to minimize their length. (c) Spin-resolved differential conductance of a film of mostly double and triple layer Co on Pt(111). Uncovered Pt areas are still visible, creating constrictions in the magnetic film. The tip is mostly sensitive to the out-of-plane component, but a small in-plane component cannot be excluded, as some walls exhibit a slightly different contrast level than the domains they separate. *Measurement parameters*: 4 K, Cr bulk tip; (a), (b): -770 mV, 1 nA; (c): -850 mV, 500 pA.

3.3.2 Domain wall width

The width of a magnetic domain wall is the length scale over which its spins rotate from one domain direction to the other one. In a simplified model the domain wall width is determined by the ratio of exchange stiffness to uniaxial anisotropy of the system (see Section 2.1.3). Here the domain wall width is investigated as a function of the Co coverage, as a means to study how the magnetic parameters change in the different layers. An example of a domain wall on the Co monolayer on Ir(111) is shown in Fig. 3.14(a): it runs in a straight line in order to minimize its length and therefore its energy. The $\mathrm{d}I/\mathrm{d}U$ signal within the blue rectangle is plotted in Fig. 3.14(b) as a function of the position across the wall. Assuming a fully out-of-plane sensitive tip, the following equation can be fitted to the obtained domain wall

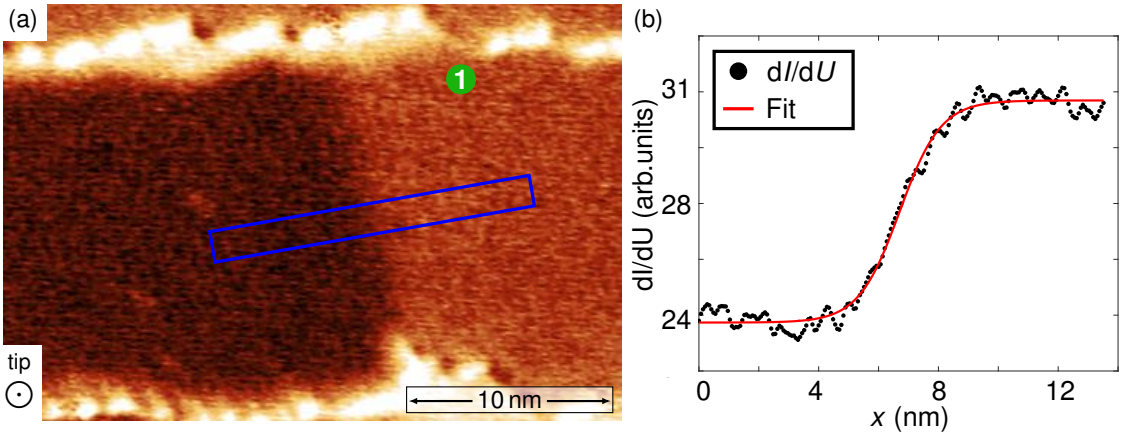

Figure 3.14: (a): Spin-polarized differential conductance map of a single domain wall in Co/Ir(111) using an out-of-plane sensitive tip. The signal inside the blue box is averaged in the short direction and then plotted against the long direction in (b). The red line is a fit of Eq. 3.1 to the data points, in arbitrary units. *Measurement parameters*: -450 mV, 500 pA, Cr bulk tip, 8 K. Adapted from [84].

profile:

$$y = y_0 + y_{sp}\cos(\varphi(x)), \tag{3.1}$$

where y_0 and y_{sp} are the spin-averaged and spin-polarized contributions to the $\mathrm{d}I/\mathrm{d}U$ signal, respectively, and where $\varphi(x)$ is the angle of the wall spins with respect to the out-of-plane easy axis, already defined in Eq. 2.14 in Section 2.1.3 as:

$$\varphi(x) = \arccos\left(\tanh\left(\frac{x - x_0}{w/2}\right)\right), \tag{3.2}$$

where x is the spatial coordinate along the profile, x_0 is the position of the center of the wall and w is the domain wall width, defined as $w = 2\sqrt{A/K}$.
The same procedure can be applied to domain walls on Co films on Pt(111), as shown in Fig. 3.15 for the Co monolayer case. Depending on the bias voltage, the dislocation network is visible in $\mathrm{d}I/\mathrm{d}U$ maps with a different intensity, which can sometimes be larger than the magnetic signal coming from the oppositely pointing domains (see Figs. 3.15(b) to (d)). The domain wall is located in a constriction, and runs almost perfectly straight, in order to minimize its length. The Co reconstruction does not seem to affect in any significant way the position of the wall, which does not avoid any of the stackings nor the bridge lines. A possible explanation for the slightly curved path of the wall could be the presence of several atomic defects which act as pinning centers, indicated with red ellipses in Figs. 3.15(a) and (c). Among the three $\mathrm{d}I/\mathrm{d}U$ maps, Fig. 3.15(c) has the lowest signal coming from the reconstruction pattern, and therefore presents the most uniform magnetic contrast across each domain. The magnetic signal within the white box in Fig. 3.15(c) is thus

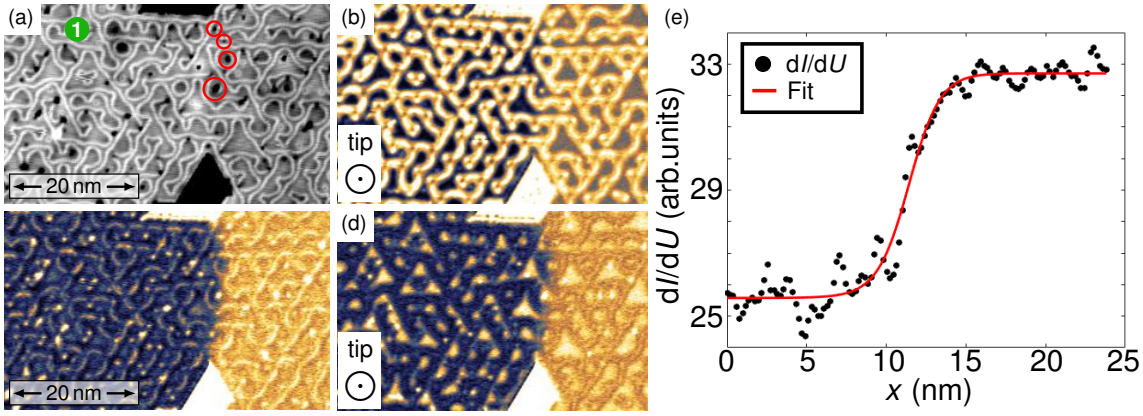

Figure 3.15: STM constant-current (a) and spin-polarized differential conductance maps ((b) to (d)) of a Co monolayer area on Pt(111). The tip has out-of-plane sensitivity. A single domain wall is located on a constriction of the film. The red ellipses in (a) and (c) indicate the position of atomic defects, which possibly act as pinning centers for the wall. The $\mathrm{d}I/\mathrm{d}U$ signal in the white box in (c) is averaged in the short direction and plotted against the long direction in (e). The red line is a fit of Eq. 3.1 to the data points, in arbitrary units. *Measurement parameters*: 1 nA, 4 K, Cr bulk tip; (a), (c): -770 mV; (b): -670 mV; (d): -870 mV. (a), (c) and (e) are adapted from [85].

plotted in Fig. 3.15(e) as a function of the position across the wall.
The domain wall width has been estimated following this procedure for domain walls in different Co layers deposited on the two substrates. The distribution of the obtained widths for the different Co layers is presented in Fig. 3.16, with the error bars indicating the uncertainty produced by the fitting procedure. The average domain wall widths are presented in Table 3.1. For the Co monolayer on Ir, the values are scattered around the mean (2.6 nm) in a window of about 1 nm. For the double layer Co on Ir there are fewer values, which are distributed in a range of 1.5 nm around the mean value of 4.4 nm. Also the few values available for the Co monolayer and triple layer on Pt differ by almost 1 nm. Possible explanations for the observed scattering could be the presence of atomic defects or inhomogeneities as well as of a dislocation network in most of the layers, which can both locally modify the magnetic parameters [85]. Additionally, in the case of the Co double layer on Ir, the size of the Co terraces where the wall is located is only two to three times larger than the wall width (while being at least 5 times larger in the Co monolayer case): geometrical constrictions [97], as well as edge effects [98], could both be responsible for variations in the wall width. Despite the scattering of the values, an increase in the domain wall width with the Co coverage is visible from the graph, for both Ir and Pt substrates, therefore indicating that the ratio $\sqrt{A/K}$ increases as more Co is deposited. This information alone is, however, not enough to recognize which of the two parameters is responsible for the increase in wall width.

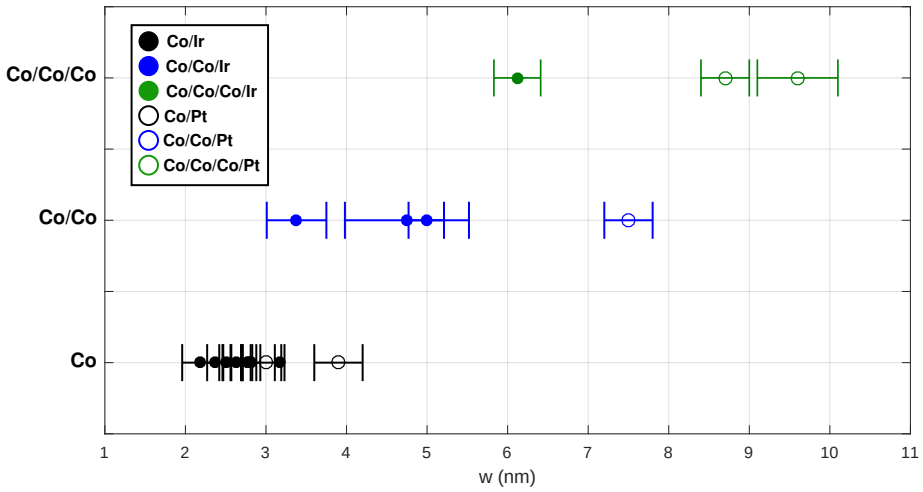

Figure 3.16: Domain wall width distribution for different Co coverages deposited on Ir(111) and Pt(111), plotted at different heights and in different colours for clarity. The values are scattered, but a clear trend towards an increase of width with Co coverage is visible.

-	Co	Co/Co	Co/Co/Co
Pt	3.5	7.5	9.2
Ir	2.7	4.4	6.1

Table 3.1: Average domain wall width (in nanometers) for different amount of Co deposited on a Pt(111) or Ir(111) substrate.

3.3.3 Influence of the DMI on domain walls

Unique sense of magnetization rotation Another interesting property of non-collinear magnetic objects such as domain walls is their sense of magnetization rotation. Whether the walls are of Bloch or Néel type (see Section 2.1.3) can provide information regarding the strength of the DMI at the Co/Ir interface, as it is known that interfacial DMI can stabilize Néel walls with a fixed sense of rotation [47, 48]. One way to investigate this is to image a sufficient number of walls with both an out-of-plane and with an in-plane sensitive magnetic tip. The correlation between the observed contrast levels with the different tips allows to conclude whether the walls all rotate in the same direction. The absolute sense of rotation cannot, however, be determined: in such an experiment a specific tip magnetization direction $\vec{m}_t$ cannot be distinguished from $-\vec{m}_t$ without further information on the in-plane tip direction (for example aligning it to an applied vectorial magnetic field). A similar procedure to study the rotational sense consists in imaging the domain walls using a tip whose magnetization is canted, i.e. it is sensitive to both the out-of-plane and to

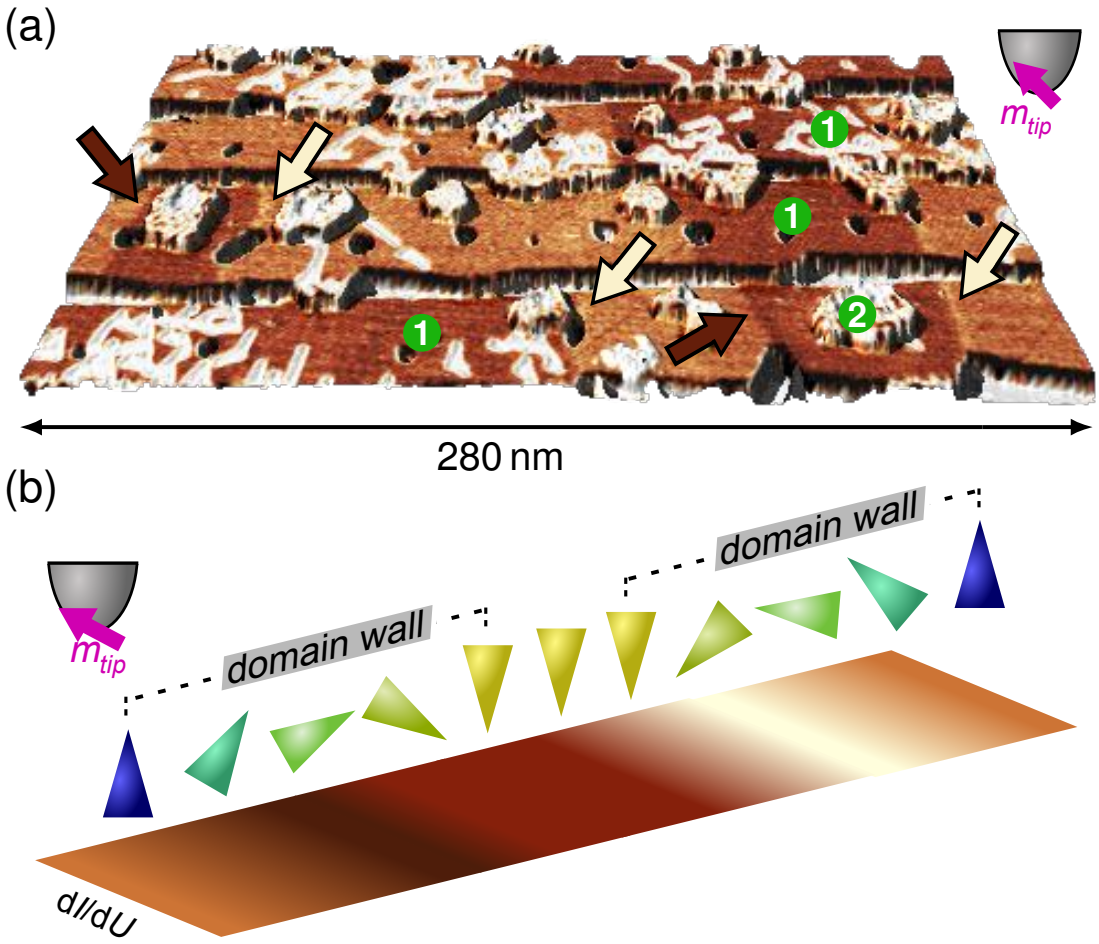

Figure 3.17: (a): Perspective view of the topography of about 1.2 monolayers of Co on Ir(111), coloured with the simultaneously measured spin-resolved differential conductance. The tip apex has a canted magnetization, and is therefore sensitive to both an in-plane and the out-of-plane magnetization components of the sample. Adjacent domain walls consistently show two alternating contrast levels (some of them indicated by the arrows). (b): Schematics of spin-resolved differential conductance contrast across two consecutive domain walls with same rotational sense using a tip with canted magnetization. *Measuring parameters*: -450 mV, 500 pA, Cr bulk tip, 8 K. Adapted from [84].

an in-plane component of the sample magnetization. Figure 3.17(a) shows several domain walls in the Co monolayer on Ir(111) imaged with such a canted tip. The domains are now separated by domain walls which appear either darker than the dark domains or brighter than the bright domains (some of them are indicated by the differently coloured arrows). The observed ordering, i.e. bright domain - very dark wall - dark domain - very bright wall (from left to right), is the same in the whole image for all the walls, and further images with the same tip on adjacent ar-

eas confirm this ordering for a total of 13 domain walls. Adjacent walls with same rotational sense consistently show this type of contrast order when imaged with a magnetic tip with canted magnetization, as depicted in Fig. 3.17(b). This allows to conclude that the walls in a monolayer Co on Ir(111) possess unique rotational sense, originating from the DMI at the Co/Ir interface.
For the double layer Co a similar conclusion can be drawn. Several domain walls have been imaged both with an out-of-plane and with an in-plane sensitive tip in a sample of almost two full Co layers on Ir(111), as shown in Fig. 3.18. The bias voltage has been selected in order to reduce the influence of the reconstruction pattern on the $\mathrm{d}I/\mathrm{d}U$ signal. In (a) the tip is sensitive to the out-of-plane sample magnetization component, and a domain structure following the Co terraces is visible. In Figs. 3.18(b) to (d) some of the domain walls are imaged again using a fully in-plane tip, and they appear as very bright or very dark lines. By combining the two datasets with the different tips one can find a sequence in the contrast levels similar to the one observed for the Co monolayer case: going from bottom to top of the scan area the observed sequence is: dark domains - very bright walls - bright domains - very dark walls. The consistency of this ordered sequence for all the considered walls is once again an indication that the walls have a fixed sense of magnetization rotation. Note that in Fig. 3.18(a) all the domain walls appear slightly darker than the dark domains. This is probably due to additional electronic contributions (TAMR or NCMR, see Section 2.2.2) visible at this bias voltage.

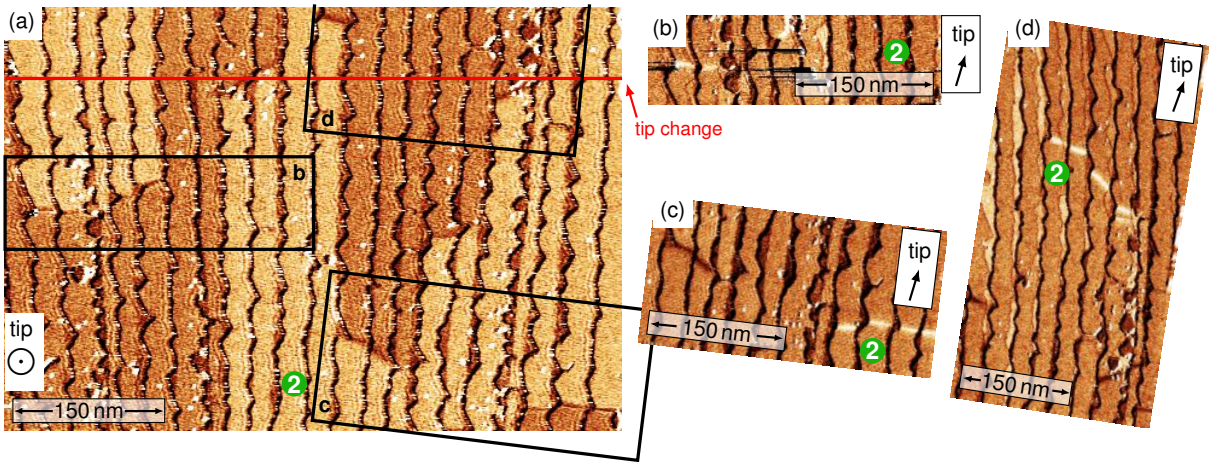

Figure 3.18: Spin-polarized differential conductance maps of about 2 monolayers of Co on Ir(111) with different tip sensitivities. In (a) the tip is sensitive to the out-of-plane component of the magnetization, in (b), (c) and (d) the tip is instead fully in-plane sensitive, as opposite magnetic domains cannot be distinguished anymore. All the walls show contrast levels consistent with the hypothesis of unique sense of magnetization rotation. The tip direction in (b) to (d) is only indicative. *Measuring parameters*: 750 mV, 600 pA, Cr bulk tip, 4 K.

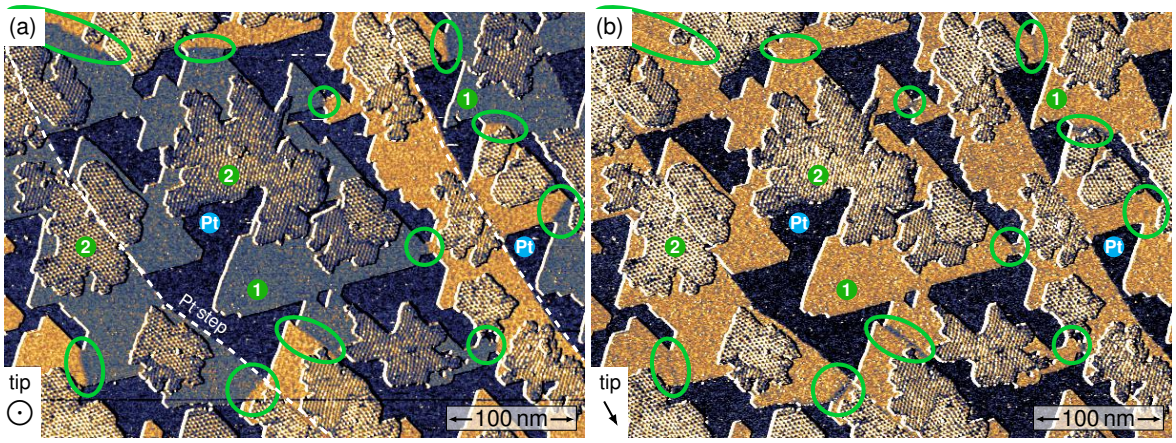

Figure 3.19: Spin-polarized differential conductance maps of a Co/Pt(111) sample, with out-of-plane (a) and in-plane (b) magnetic sensitivity. In (a) the oppositely oriented domains are clearly visible, as well as several domain walls separating them, indicated by the green ellipses. In (b) the domains are not visible anymore, but the domain walls now present different $\mathrm{d}I/\mathrm{d}U$ signals depending on their orientation. *Measurement parameters*: 250 mV, 1 nA, 4 K, Cr bulk tip. Adapted from [85].

Also in the case of Co on Pt a specific bias voltage is selected to minimize the $\mathrm{d}I/\mathrm{d}U$ signal from the dislocation network in the film. This is shown in Fig. 3.19, where the Co monolayer displays a more uniform $\mathrm{d}I/\mathrm{d}U$ signal. Figures 3.19(a) and (b) show the same area imaged with an out-of-plane sensitive and with a fully in-plane sensitive tip, respectively. The domain walls, indicated by the green ellipses, appear all very similar in (a), while in (b) they possess different levels of $\mathrm{d}I/\mathrm{d}U$ contrast, from hardly visible walls to very dark ones. The absence of walls which are brighter than the out-of-plane domains is explained by additional electronic contributions to the $\mathrm{d}I/\mathrm{d}U$ signal on the walls, namely TAMR and NCMR. From these data alone it is not possible to disentangle TAMR from NCMR in this experiment. This additional electronic contrast reduces the $\mathrm{d}I/\mathrm{d}U$ signal produced by TMR with in-plane tip sensitivity, as sketched in Fig. 3.20. In this way, walls with positive TMR $\mathrm{d}I/\mathrm{d}U$ signal are hardly visible, as such signal cancels out with the reduced signal from TAMR or NCMR, whereas walls with negative TMR signal have a very dark contrast. To investigate whether all these walls have the same rotational sense, some of them have been imaged at higher resolution using an in-plane sensitive magnetic tip (Figs. 3.21(b) to (d)). As it is expected that the DMI at the Co/Pt interface plays a role for the magnetization within the walls, the walls are assumed to be of Néel type and a unique rotational sense is tentatively assigned to them, which is selected arbitrarily to be a rotation from the bright to the dark magnetic domains (i.e. the in-plane spins of the walls point towards the dark domains). It must be then verified if the magnetic contrast of the walls obtained with an in-plane tip is consistent with this hypothesis. For this analysis several walls among those visible in Fig. 3.21(a) have

been discarded. Wall #1 has been discarded because it moves between different positions while scanning across it, and walls #3, #7 and #8 were discarded because they sit on constrictions whose size is comparable with the domain wall width, which can give rise to additional effects due to confinement [97] or edge effects [98].
Walls #2 and #6 are hardly visible, i.e. in this case they are the walls with the highest $\mathrm{d}I/\mathrm{d}U$ signal. Walls #4 and #11 have a slightly lower $\mathrm{d}I/\mathrm{d}U$ signal, followed by walls #5 and #9, which are even darker. Wall #10 has the lowest contrast level. The magnetization direction within the walls in Figs. 3.21(b) to (d) is indicated with red arrows. The tip magnetization direction is closest to the magnetization directions of the brightest walls, namely walls #2 and #6. This means that the angle between tip and wall magnetization direction is the smallest for these two walls. Walls #4 and #11 present a slightly lower $\mathrm{d}I/\mathrm{d}U$ contrast, and therefore such angle is expected to be larger than for walls #2 and #6. Similarly, the angles for walls #5 and #9 will be even larger, given their darker $\mathrm{d}I/\mathrm{d}U$ contrast. Finally the largest tip-wall angle, i.e.

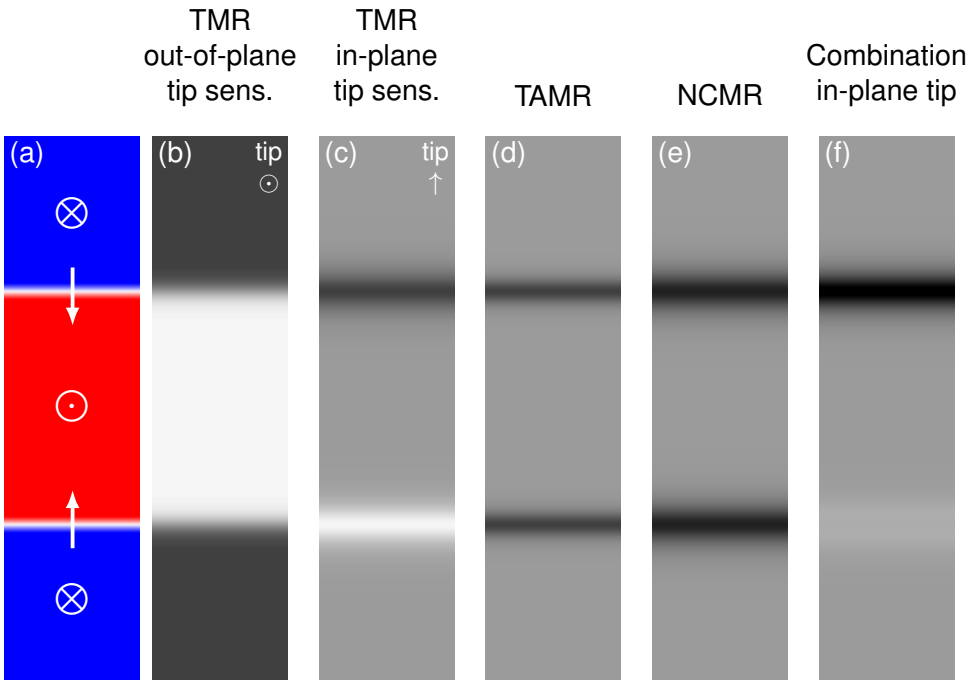

Figure 3.20: Sketch explaining the contrast observed in Fig. 3.19 in the case of two Néel walls with the same rotational sense (a). The images (b) and (c) show the contrast induced by the tunneling magnetoresistance (TMR). In (b) the tip is sensitive to the out-of-plane component of the sample magnetization, while in (c) to the in-plane component, which is perpendicular to the wall. Image (d) shows the contrast generated by the tunneling anisotropic magnetoresistance (TAMR) and image (e) the contribution of the non-collinear magnetoresistance (NCMR), both assumed negative here. Image (f) is a linear combination of the contributions (c), (d) and (e) reproducing the contrast in Fig. 3.19(b). Adapted from [85].

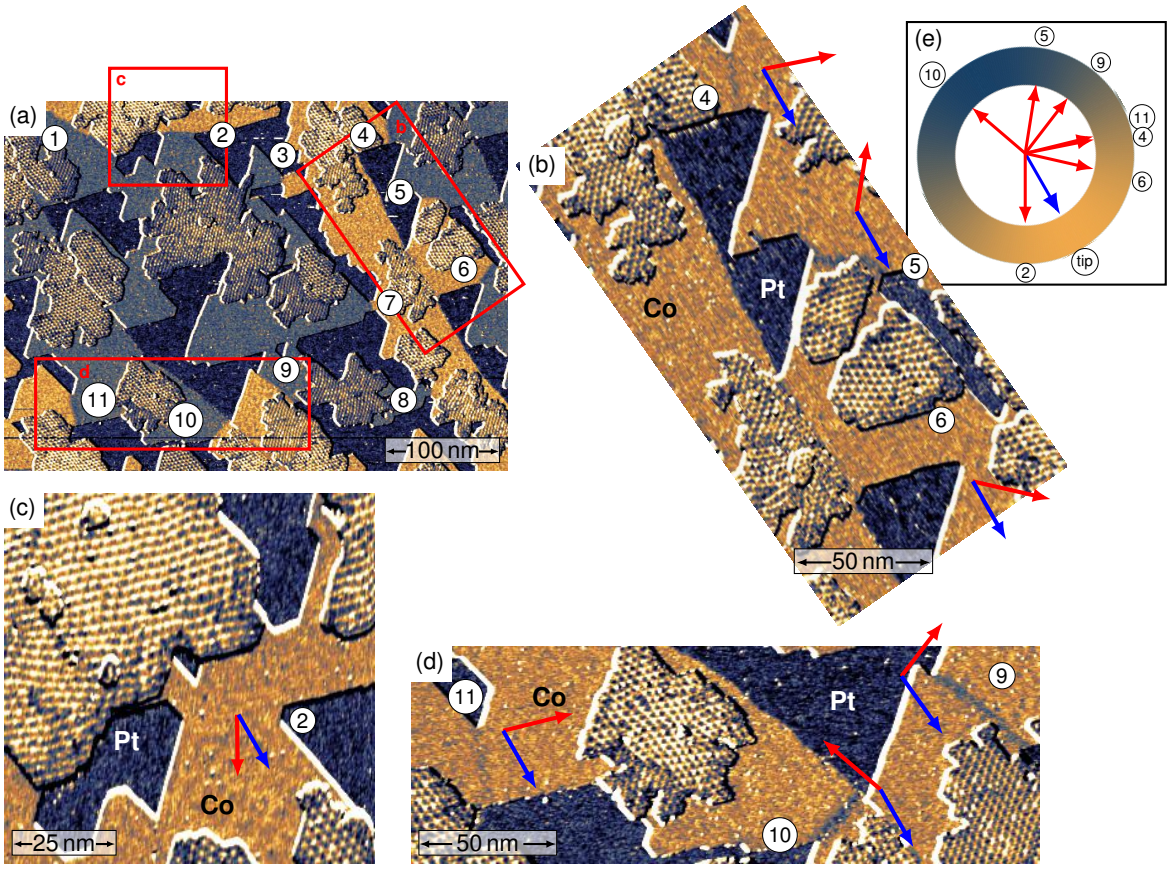

Figure 3.21: (a): Spin-resolved differential conductance map with out-of-plane sensitivity of a Co/Pt(111) sample, with several domain walls labelled by numbers. The red boxes indicate the areas shown in (b), (c) and (d). (b) to (d): Higher resolution images of domain walls in (a) using a tip sensitive to the in-plane magnetization component. The red arrows indicate the magnetic direction within the walls. The blue arrows indicate the tip magnetization direction. (e): Calculated TMR contrast as a function of the angle with respect to the tip magnetization direction (in blue). The directions of all the considered wall magnetizations are drawn in red and labelled by numbers. *Measurement parameters*: (a) to (d): 250 mV, 1 nA, 4 K, 0 T, Cr bulk tip. Adapted from [85].

closest to 180°, is expected to be for wall #10. The tip magnetization direction derived in this way is sketched by the blue arrow. All the observed $\mathrm{d}I/\mathrm{d}U$ contrast levels of the walls are in accordance with the proposed magnetization direction within the walls, as sketched in Fig. 3.21(e), demonstrating that the initial assumption of fixed sense of magnetization rotation is correct. Note that this conclusion also holds when assuming the opposite wall rotational sense, namely from dark to bright magnetic domains, by simply considering a tip direction rotated by 180° in the sample plane. For this reason, it is not possible to determine from these data the absolute rotational sense of the walls.

Absolute sense of rotation As mentioned above, the DMI at the interface between Co and substrate is responsible for favouring Néel walls over Bloch walls, with a fixed sense of rotation. Specifically, the sign of D, the DM vector, determines the absolute sense of rotation, i.e. whether the walls rotate clockwise or anti-clockwise when going, for example, from an up-pointing domain to a down-pointing domain (also referred to as right-rotating and left-rotating walls). Experiments like the ones presented in the above paragraph are not sufficient to determine the absolute rotational sense of the walls, since the exact tip magnetization direction cannot be determined, and one can only investigate the orientation of the walls' magnetization with respect to it. One way to overcome this limitation is to use tips whose magnetization can align with the direction of an applied magnetic field, such as W tips which are coated with several atomic layers of Fe. The shape anisotropy of the Fe film favours a magnetization of the tip apex pointing parallel to the sample plane, and its direction can be controlled using a magnetic field. Therefore, using out-of-plane and in-plane fields in combination with such tips allows to identify right-rotating and left rotating magnetic structures [99, 100].
Here a different method to determine the absolute rotational sense of Néel-type domain walls is described, which still relies on an in-plane magnetic field, but does not require a tip magnetization that aligns to it. The idea is to determine the rotational sense of a wall by observing its changes upon the application of an in-plane field along the wall's direction [101]. To illustrate this, spin dynamics simulations of two domain walls with opposite rotational sense in in-plane magnetic fields have been performed [84]. The following Hamiltonian is considered:

$$\mathcal{H} = -J \sum_{<ij>} (\mathbf{m_i} \cdot \mathbf{m_j}) - \mathbf{D} \sum_{<ij>} (\mathbf{m_i} \times \mathbf{m_j}) + K \sum_i (m_i^z)^2 - \sum_i \mu_S \mathbf{B} \cdot \mathbf{m_i}, \tag{3.3}$$

where $\mathbf{m_i} = \frac{\mathbf{M_i}}{M_i}$ is the unit vector of the magnetic moment at atom site i. The exchange interaction and the DMI are assumed to act only between nearest neighbors $< ij >$, with strength J and $\mathbf{D}$, respectively. K represents the uniaxial magnetocrystalline anisotropy, and the last term accounts for the Zeeman energy due to an external magnetic field $\mathbf{B}$. The values of J, $\mathbf{D}$ and K for a single layer of Co on Ir(111) have been calculated by Sebastian Meyer and co-workers using DFT [84], and are shown in Table 3.2 in Section 3.4.2. A magnetic moment of μ_S = 2.2 μ_B per atom is used, which is the sum of the calculated moment of the Co atoms (1.9 μ_B) and the induced moment of the interface Ir atoms (0.3 μ_B). The equilibrium positions for domain walls stabilized by opposite directions of $\mathbf{D}$ are obtained by solving the Landau-Lifshitz-Gilbert equation using an implicit method [102–104]. Figures 3.22(a) and (b) show the walls' equilibrium configurations without magnetic field, while Figs. 3.22(c) and (d) show those upon application of a magnetic field in the in-plane (here y) direction. The field tilts the spins of the walls towards the field direction, but the domain walls also tilt to partially recover the cycloidal configuration, which is favoured by the DMI.

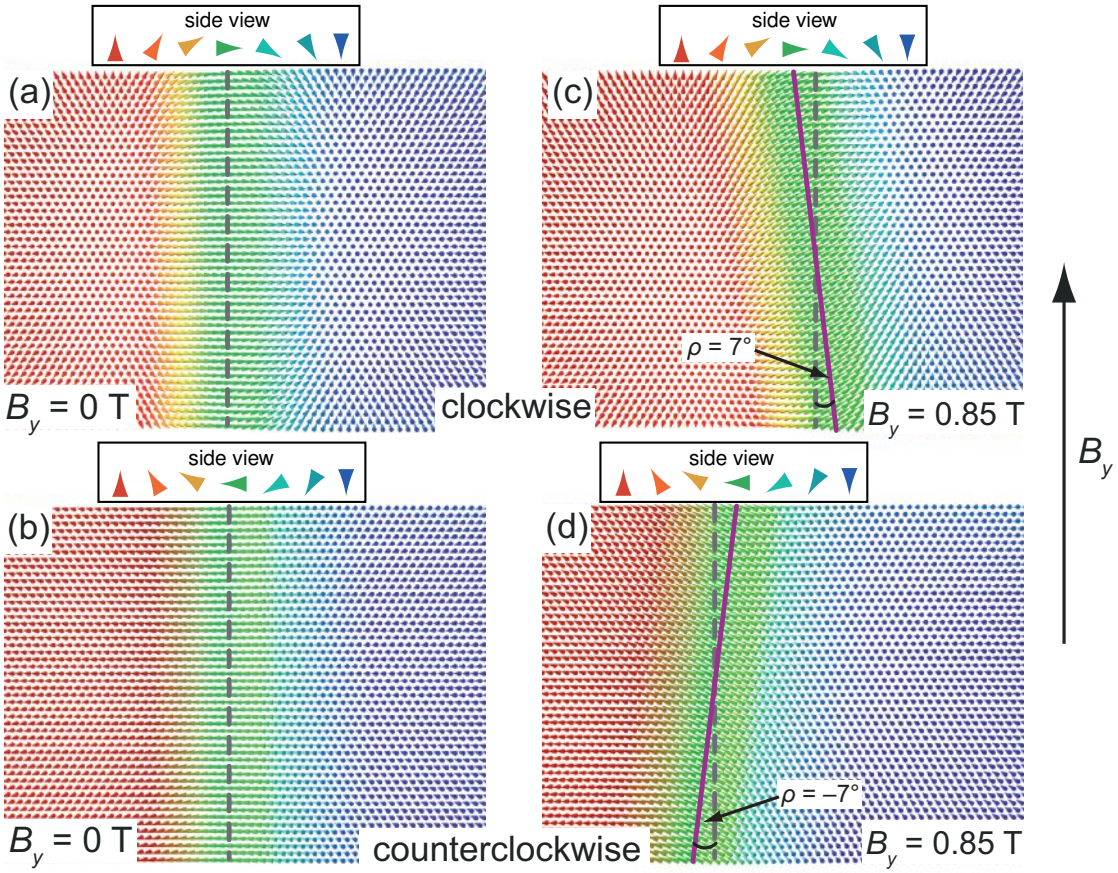

Figure 3.22: Spin dynamics simulation with open boundary conditions of two Néel domain walls with opposite rotational sense, which is depicted in the side view sketches at the top of each panel. (a), (b): Wall equilibrium position in zero magnetic field. (c), (d): Wall equilibrium position when an in-plane field $\mathbf{B_y}$ of 0.85 T is applied. The two walls tilt in opposite directions with an angle of about $\pm 7°$ to partially maintain their cycloidal configuration. Adapted from [84].

Thus, the rotational sense of the domain walls can be experimentally determined from the direction of their tilting in an in-plane magnetic field. Only the Co monolayer on Ir(111) case has been considered here, since the reconstruction pattern present in higher Co layers, and in Co/Pt(111) samples as well, could affect the equilibrium position of the walls and therefore their behaviour in magnetic fields [85]. A domain wall is selected (see Fig. 3.23(a)) and imaged in the absence of magnetic field to determine its exact position (Fig. 3.23(b)). When scanning in the forward and backward directions the wall is in slightly different positions, as indicated by the dashed lines. This can occur when the tip has a small residual stray field, and therefore drags the wall back and forth during scanning. A magnetic field along the y direction is then applied, as indicated by the blue arrow in Fig. 3.23(c), and a tilting of the wall in both the forward and backward scans is observed. From the direction of the tilting

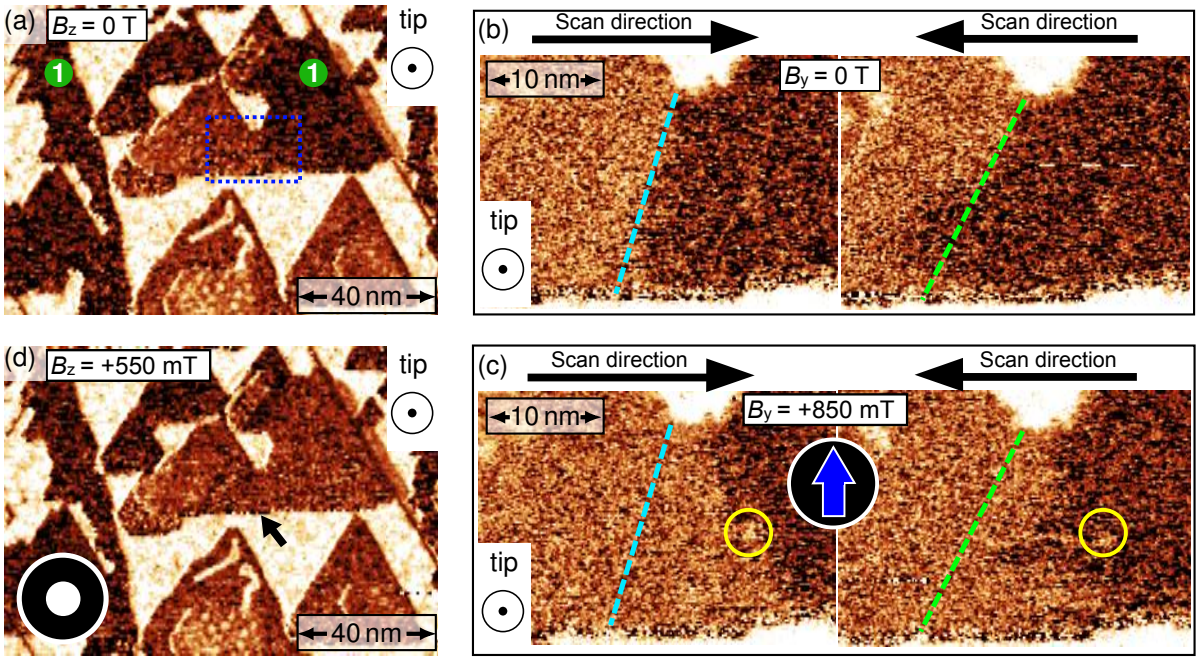

Figure 3.23: Spin-resolved differential conductance maps of Co monolayer islands with out-of-plane magnetic sensitivity. (a): The DW occurs at the coalescence point of two Co islands. The dotted blue rectangle indicates the area imaged in (b) and (c), in zero field and with an in-plane field along the y direction, respectively. The direction of the magnetic field is indicated by the blue arrow. The dashed lines mark the position of the wall in the forward (left) and backward (right) scans at zero-field. In both cases the wall tilts in an in-plane field with respect to these lines. The yellow circle indicates an impurity in the Co, possibly acting as a pinning center for the wall. (d): Same area as in (a), imaged while applying an upwards pointing out-of-plane magnetic field. The expanding bright domain thus points along the field direction. *Measuring parameters*: -450 mV, 350 pA, Cr bulk tip, 4.7 K. Adapted from [84].

the direction of the wall's in-plane magnetization is deduced, which is pointing to the right. To determine the absolute rotational sense it is then necessary to assign the out-of-plane magnetization directions of the adjacent domains, which is done by applying a magnetic field in the out-of-plane direction. This is visible in Fig. 3.23(d), where the bright domain, indicated by the black arrow, has expanded, while the dark one has shrunk. The bright (dark) areas in the Co correspond then to the domains pointing upwards (downwards), and therefore the magnetization across the wall rotates clockwise, as in Figs. 3.22(a) and (c). The observed tilting angle is larger than the one expected from Fig. 3.22, possibly because the wall is attracted by an impurity (see yellow circles in Fig. 3.23(c)) which acts as a pinning center, although the wall still tilts in the direction favoured by the DMI. In the absence of impurities and with a non-interacting tip, this method allows to quantify the strength of the DMI in the system. This can be done by measuring the tilting angle as a function of

the applied in-plane magnetic field, and then finding the correct value of **D** to reproduce such a tilting in a spin dynamics simulation based on reasonable assumptions for J and K. Note that in order to make a statistically stronger claim on the direction of magnetization rotation, this experiment needs to be repeated on several domain walls.

3.4 Effect of a Pt top layer

3.4.1 Effects on domain wall properties

This Section presents an investigation of how the magnetic state of a monolayer Co on Ir(111) is modified by adding a Pt atomic layer on top, in particular with respect to DMI. It has been claimed that the DMI in a Co film of several monolayers sandwiched between Ir and Pt increases significantly due to an additive effect of the two interfaces [30, 105]. The results obtained here are compared to DFT calculations to investigate whether this effect is present also in the limit of one Co layer, when the Pt/Co and Co/Ir interfaces are only one atom apart.
Figure 3.24(a) shows the magnetic state of isolated Pt islands deposited at room temperature on a Co monolayer. The spin-resolved $\mathrm{d}I/\mathrm{d}U$ signal of the Pt islands is strongly correlated with that of the surrounding Co layer: the Pt islands with dark (bright) contrast are always inside dark (bright) Co magnetic domains, suggesting that the origin of such contrast is magnetic, and therefore that the Co induces a magnetic polarization in the Pt. As the Co monolayer on Ir has an out-of-plane easy axis, the tip magnetization direction in Fig 3.24(a) has out-of-plane sensitivity, and therefore it is concluded that the Pt/Co bilayer is ferromagnetic with an out-of-plane component. There are two $\mathrm{d}I/\mathrm{d}U$ contrast levels on the Pt for each magnetization direction, originating from islands growing in the two different stackings. At this low Pt coverages no domain wall located on the Pt was found, and all of the observed islands are single domain ferromagnetic. This suggests that the domain wall energy per unit length:

$$\sigma_{DW} = 4\sqrt{AK} - \pi|D|, \tag{3.4}$$

is higher in the Pt/Co bilayer than in the uncovered Co layer. In Eq. 3.4 A is the exchange stiffness, K is the effective uniaxial anisotropy and D is the DMI constant. Another indication for this change in domain wall energy could be the appearance, together with the usual large scale magnetic domains, of smaller domains, some of them indicated by the green ellipses in Fig. 3.24(a). Such objects always encompass at least one Pt island inside them, and are surrounded by larger magnetic domains with opposite orientation. In uncovered Co layers this has been observed for a few double layer Co islands surrounded by Co monolayer. In order for the objects in Fig. 3.24(a) to align their spins with the ones of the surrounding domains, the domain walls have to cross areas covered by Pt. If σ_{DW} is higher in the Pt, this process

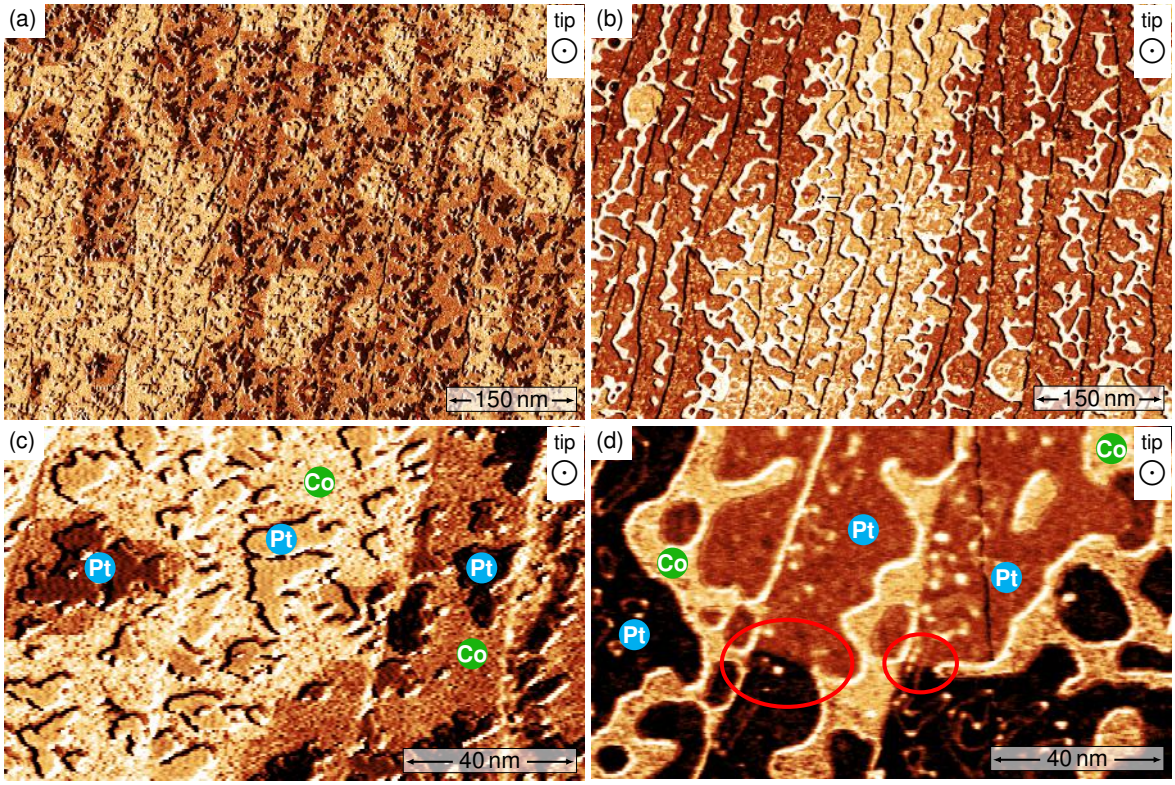

Figure 3.24: Spin-polarized differential conductance maps, with out-of-plane magnetic sensitivity, of different amounts of Pt grown on a full Co monolayer on Ir(111). (a), (c): About 0.3 monolayers of Pt deposited at room temperature. The green ellipses indicate small magnetic objects encompassing Pt islands. The domain walls avoid crossing Pt islands, creating more complicated paths in the Co instead. (b), (d): About 0.6 monolayers of Pt deposited on the sample and subsequently post-annealed. The inset in (c) shows one domain wall moving, once an out-of-plane magnetic field is applied. The domain walls are rarely located on the Pt/Co bilayer, but when it happens (see red ellipses) they follow very straight paths to minimize their lengths, contrarily to what happens when they are on the bare Co. *Measurement parameters*: 1 nA, 8 K, (a) to (c): -450 mV, (d): -550 mV. (c) and (d) are adapted from [84].

has an additional energy cost, which could prevent some of the objects to shrink and vanish.

More extended Pt films on the Co monolayer can be grown using a post-annealing procedure, as described in Section 3.2.3. The magnetic state of such a sample is shown in Fig. 3.24(b): once again large magnetic domains are visible, although with this tip at this bias voltage the difference in contrast is visible mostly on the Pt, and not on the underlying Co. It has been observed that for different bias voltages both Co and Pt display a 2-levels $\mathrm{d}I/\mathrm{d}U$ contrast, indicating that also for the post-annealed sample the Co induces a polarization in the out-of-plane direction in the Pt layer. As an additional proof that the Pt/Co bilayer is out-of-plane magnetized, an

out-of-plane magnetic field is applied, and a small displacement of one domain wall in the Pt is observed, visible in the inset and marked with a blue ellipse. Although the contrast on the Co patches is not clearly visible, it is evident from Fig. 3.24(b) that the vast majority of the Pt areas are single domain ferromagnetic, and only seldom does a domain wall cross the Pt. This provides additional evidence that the walls have a lower energy when located on the bare Co/Ir(111) surface. A closer view on a few domain walls in both types of Pt/Co/Ir(111) samples is presented in Figs. 3.24(c) and (d). Instead of minimizing their length, the walls create longer and more complex paths on the Co in order to avoid crossing the Pt areas as much as possible. On the other hand, when going through the Pt, the walls are located in geometrical constrictions and follow straight paths, as indicated by the red ellipses in Fig. 3.24(d).

Due to the higher domain wall energy, walls on Pt are rare and mostly located where confinement effects can change the intrinsic domain wall width [97]. Only two domain walls on the Pt/Co bilayer were found in constrictions at least twice as large as the wall width, and the estimated widths are 2.7 nm and 3.6 nm. These values are similar to the ones found for the bare Co monolayer on Ir(111), although more values would be needed for a more accurate estimate of the average domain wall width.

Given the knowledge on width and energy per unit length for the domain walls in the different materials, one can try to extract information about the magnetic parameters in the films. As already explained, in the model used here the domain wall width depends on the ratio of exchange stiffness and effective uniaxial anisotropy. Assuming that domain walls in Co/Ir(111) and in Pt/Co/Ir(111) have roughly the same width, it can be concluded that the ratio A/K remains the same in the two systems, i.e. A and K either increase or decrease by the same percentage when going from Co/Ir(111) to Pt/Co/Ir(111). Combining this with the indication of an increased domain wall energy in Pt/Co/Ir(111), one can write the following system of equations

$$\begin{cases} A_{Co}/K_{Co} \simeq A_{Pt/Co}/K_{Pt/Co} \\ \left(4\sqrt{A_{Pt/Co}K_{Pt/Co}} - \pi|D_{Pt/Co}|\right) > \left(4\sqrt{A_{Co}K_{Co}} - \pi|D_{Co}|\right). \end{cases}$$

The increase in domain wall energy can be caused by either an increase of $\sqrt{AK}$ or by a decrease of $|D|$ (or a combination of both effects). Unfortunately, from the data available it is not possible to identify which of the two terms is responsible for the change in energy: an increase of both A and K in Pt/Co, as long as it keeps the wall width constant, is plausible, but it cannot be excluded that a decrease of $|D|$ in Pt/Co is instead the main cause. Therefore from these data alone the effect of a Pt layer on the DMI in the system cannot be deduced. To gain further insight the results are compared with theoretical calculations.

3.4.2 Comparison with theoretical results

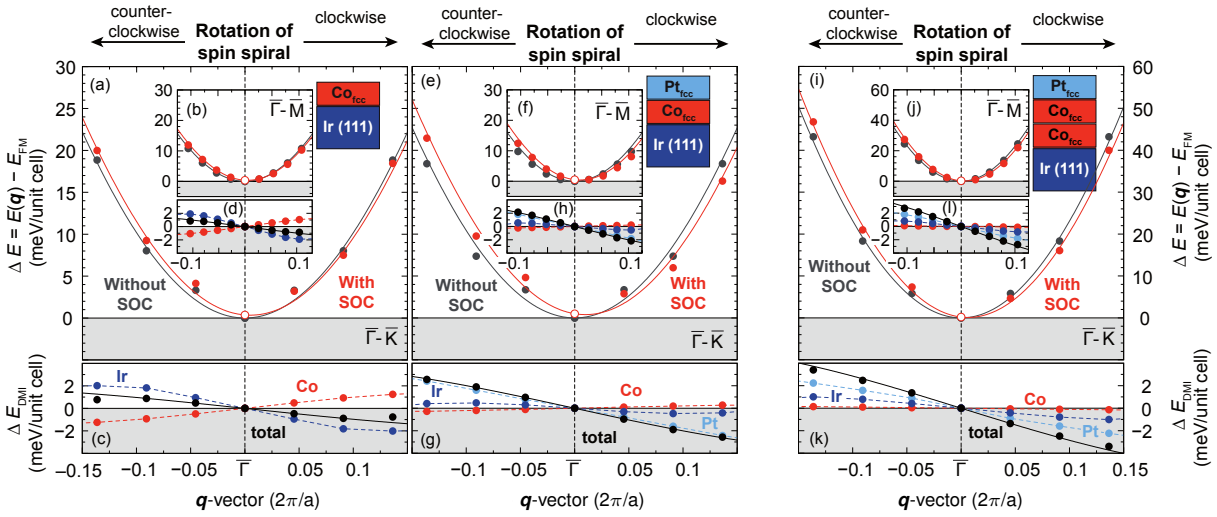

Figure 3.25: (a), (b) Calculated energy dispersion $E(\mathbf{q})$ of flat, cycloidal spin spirals for Co/Ir(111) ((e), (f) for Pt/Co/Ir(111), (i), (j) for Pt/Co/Co/Ir(111)) without (grey dots) and with (red dots) spin-orbit interaction for left and right rotating spin spiral states in $\overline{\Gamma}$-$\overline{\mathrm{K}}$ and $\overline{\Gamma}$-$\overline{\mathrm{M}}$ direction, respectively. The grey line is a fit of the dispersion to the Heisenberg model, the red line is a fit including the DMI and the magnetocrystalline anisotropy. (c), (d), (g), (h), (k), (l) Element-resolved energy contribution for Co/Ir(111), Pt/Co/Ir(111) and Pt/Co/Co/Ir(111) to the DMI $\Delta E_{\mathrm{DMI}}(\mathbf{q})$. Note that the total DMI is the sum of all contributions and that all energies are given per unit cell (i.e. two magnetic atoms for Pt/Co/Co/Ir(111)). The black curve is the fit of the DMI. All fits are made within the nearest-neighbor approximation. Taken from [84].

System	J	D	K	$\Delta E_{\mathrm{DW-FM}}$	w	w_{exp}
Co/Ir(111)	$+17.6$	-0.54	-0.73	$+53.3$	3.2	2.7 ± 0.3
Pt/Co/Ir(111)	$+18.0$	-1.12	-1.00	$+43.8$	2.8	$2.7, 3.6$
Pt/Co/Co/Ir(111)	$+20.0$	-0.80	-0.09	-4.1	9.9	–

Table 3.2: Calculated values for the nearest neighbor exchange interaction J (meV), Dzyaloshinskii-Moriya interaction D (meV), magnetocrystalline anisotropy energy K (meV), calculated energy difference [47] $\Delta E_{\mathrm{DW-FM}} = \frac{4}{a}\sqrt{2|JK|} - \frac{2}{a}\pi\sqrt{3}|D|$, between a DW and the FM state (meV/nm), and calculated DW width $w = 2a\sqrt{\frac{3J}{2|K|}}$, with a the lattice constant of the (111) plane of the substrate, compared to the experimental DW width w_{exp} (nm). $D < 0$ represents clockwise rotation and $K < 0$ represents an out-of-plane easy magnetization axis. All magnetic interactions are given per Co atom. Taken from [84].

The Co monolayer on Ir(111) and the Pt/Co/Ir(111) systems are mostly pseudomorphic films. It is therefore possible to model them and calculate their magnetic

properties using density functional theory, and see if the results reproduce what has been observed in the experiments. This has been done by Sebastian Meyer and co-workers for both systems [84] and the main results are presented in Fig. 3.25 and in Table 3.2. Panels (a) and (b) ((e) and (f)) in the Figure show the calculated energy dispersion for Co/Ir(111) (Pt/Co/Ir(111)) in $\overline{\Gamma}$-$\overline{\mathrm{K}}$ and $\overline{\Gamma}$-$\overline{\mathrm{M}}$ directions, respectively. The ferromagnetic state is the lowest energy state for both systems, and the calculated magnetocrystalline anisotropy (see Table 3.2) favours the out-of-plane magnetization direction. From the calculations it is possible to disentangle the contribution of the single layers to the total DMI in the system (see panels (c), (d), (g) and (h)). For both systems the DMI favours clockwise-rotating non-collinear magnetic states ($D < 0$, in agreement with what is observed experimentally). Additionally, the total DMI increases when adding a single Pt layer on top of the Co, but for this bilayer system it is mostly due to the Pt/Co interface, while the contribution from the Ir layer is negligible. When an additional Co layer is introduced, separating the two interfaces farther from each other (see panels (k) and (l)), the contribution from the Ir layer becomes significant again, supporting the interpretation of DMI as an additive effect [30]. Thus, in the limit case of a single Co layer sandwiched between Pt and Ir only one interface contributes significantly to the DMI, probably as a consequence of hybridization effects between the two interfaces, which are only one atom apart.
The energy difference between a domain wall and the ferromagnetic state has been calculated according to:

$$\Delta E_{\mathrm{DW-FM}} = \frac{4}{a}\sqrt{2|JK|} - \frac{2}{a}\pi\sqrt{3}|D| \tag{3.5}$$

where a is the lattice constant of the (111) plane of the substrate [47]. Domain walls are found to be energetically unfavourable in both Co/Ir(111) and Pt/Co/Ir(111) (see Table 3.2), and the obtained domain wall widths are in good agreement with the ones estimated experimentally.
The smaller domain wall energy in Pt/Co/Ir(111) seems to disagree with the experimental observation of domain walls being more likely to occur in the uncovered Co monolayer. However, the difference between the two domain wall energies is small with respect to the accuracy of the parameters. An error of only 0.1 meV in either the value of K or D can lead to $\Delta E_{\mathrm{DW-FM}}$ values which are energetically degenerate. Due to the high sensitivity of $\Delta E_{\mathrm{DW-FM}}$ to the magnetic parameters, it is then not possible to predict from such calculations in which layer the domain walls are favoured to be located.

3.5 Magnetism of Co/Ir(111) at higher temperatures

In order for non-collinear magnetic structures to be used in technological applications, they have to be stable at room temperature. For magnetic skyrmions, thermal stability in ultrathin films has already been achieved by increasing the thickness of

the magnetic layers and the number of layer repetitions [16, 25, 30–32, 106]. Additionally, the Curie temperature for several transition metals has been predicted, and observed, to increase with the film thickness [107–110]. Therefore investigating the minimum film thickness to guarantee room temperature stability of magnetic structures remains a topic of great interest. For example, it has been shown that for one monolayer of Fe on Ir(111) the magnetic ground state, known as nanoskyrmion lattice [11], vanishes around 28 K [111], while on the double and triple layer Fe the magnetic structures are stable up to 150 K and room temperature, respectively [112]. The Curie temperature (T_c) for Co ultrathin films has already been studied for different substrates, and it is often measured as a function of the average Co coverage on the whole sample. A few examples are presented in Table 3.3.

System	Co thickness (monolayers)
Co/Cu(100) [107]	2.2
Co/Cu(111) [109]	1.2
Co/Rh(001) [113]	~ 2
Co/W(110) [114]	1.7

Table 3.3: Minimum Co thickness, on different substrates, necessary to achieve T_c around room temperature.

Instead of studying the T_c of the whole film, using SP-STM it is possible to observe separately the magnetism of the single atomic layers and identify which layers display magnetic features. This Section presents SP-STM measurements on monolayer and double layer Co on Ir(111) at about 78 K and at room temperature. The film is still magnetic on both layers at 78 K, while at room temperature only the double layer shows signs of magnetic contrast. The measurements were performed with a low temperature STM cooled with liquid nitrogen, or operated at room temperature. At these temperatures no magnetic field is available.

3.5.1 Magnetism at 78 K

Figure 3.26 shows a perspecitve view of a sample of 1.5 monolayers of Co on Ir(111) at 78 K. The image is coloured with the measured $\mathrm{d}I/\mathrm{d}U$ signal. Both for the monolayer and the double layer two levels of contrast are clearly visible. Areas with same contrast level extend over several terraces, in some areas following the terrace edges, similarly to what is observed for magnetic domains in Section 3.3. At these temperatures no magnetic field is available, and from this data alone it is not possible to confirm whether this contrast has magnetic origin, or if it is for example due to Co areas growing in different stackings, although there is no evidence for such kind of stacking contrast in samples with same Co coverage investigated at low temperature. Additional insight can be gained from a different sample with mostly Co double layer, which displays again two levels of $\mathrm{d}I/\mathrm{d}U$ contrast, as shown in Fig 3.27(a):

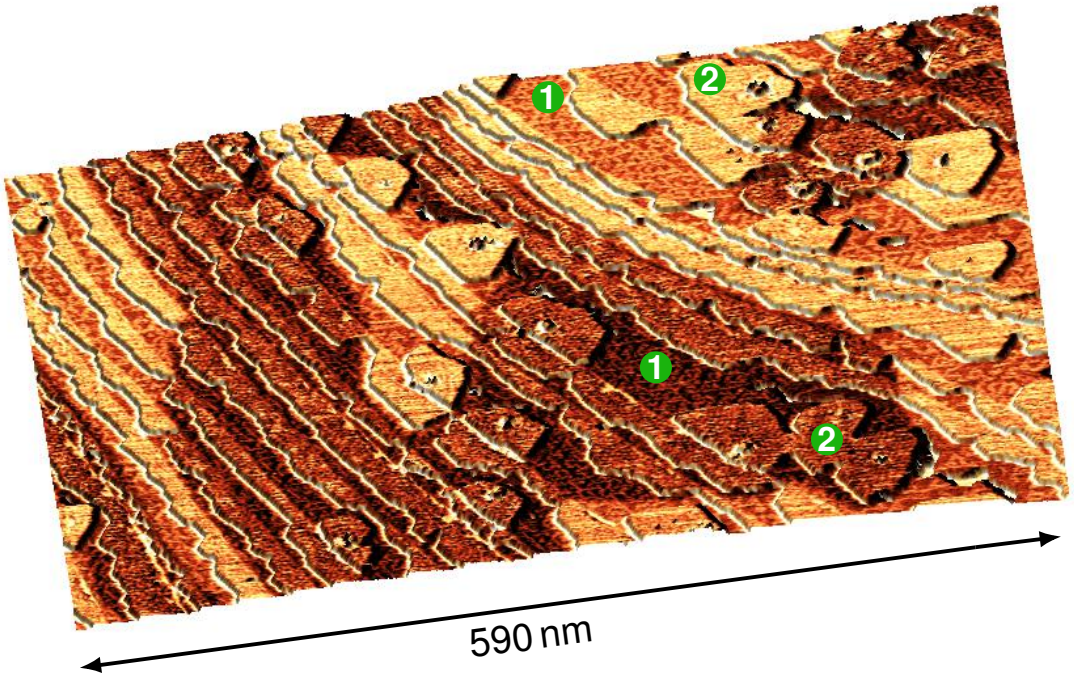

Figure 3.26: Perspective view of the topography of about 1.5 monolayers of Co on Ir(111), coloured with the simultaneously measured differential conductance. The contrast levels and arrangement are similar to the domain structures observed in the Co double layer at 8 K. *Measurement parameters*: -250 mV, 1 nA, Cr bulk tip, 78 K.

here the areas with different $\mathrm{d}I/\mathrm{d}U$ signal are oriented following the terrace edges, creating a stripe-like pattern very similar to the one observed in Fig. 3.10(a). Additionally, the contrast on the double layer Co changes in correspondence with constrictions of the film, another feature which is typical for magnetic domain walls. All the above observations strongly suggest that the observed contrast in Figs. 3.26 and 3.27 has a magnetic origin, and therefore that both the Co monolayer and double layer are still magnetic at 78 K. The appearance of only two levels of contrast over several areas is also an indication, at least for the Co double layer, that the sample magnetization in this layer still has an out-of-plane component. To confirm this for the Co monolayer as well, more areas with a two-levels contrast should be observed. The inset of Fig. 3.27(a) shows a domain wall on the Co double layer: the $\mathrm{d}I/\mathrm{d}U$ signal of the wall has been plotted in Fig. 3.27(b) and Eq. 3.1 has been fitted to it to extract the domain wall width. It was possible to observe only two walls on the Co double layer which were in constrictions at least twice as large as their width. The obtained width values are 4.7 nm and 5.9 nm, which are close to the ones found for the Co double layer at low temperature. A better statistics on such wall widths could help understand whether the average wall width in this system is increasing with temperature.

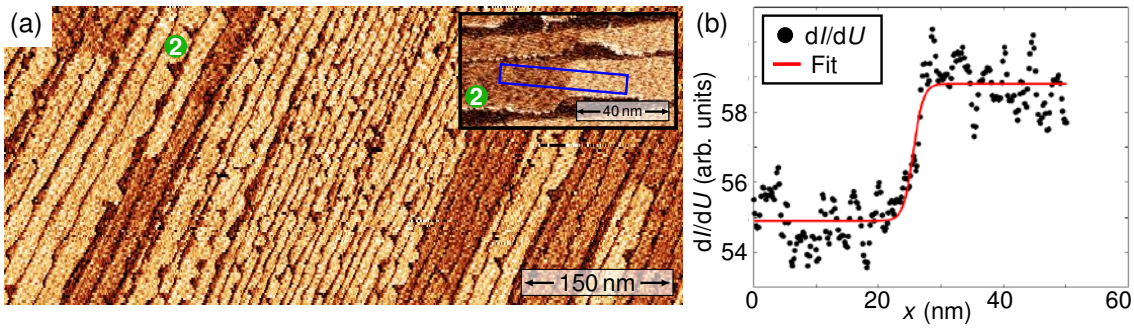

Figure 3.27: (a): Spin-polarized differential conductance map of about 1.8 monolayers of Co on Ir(111) at 78 K. The presence of only two levels of contrast on the Co suggests that the sample has out-of-plane magnetization. A domain wall on the Co double layer is visible in the inset. The signal in the blue box is averaged in the short direction and plotted against the long direction in (b). The red line is a fit of Eq 3.1 to the data points, in arbitrary units. *Measurement parameters*: 800 mV, 500 pA, 78 K, Cr bulk tip.

3.5.2 Magnetism at 300 K

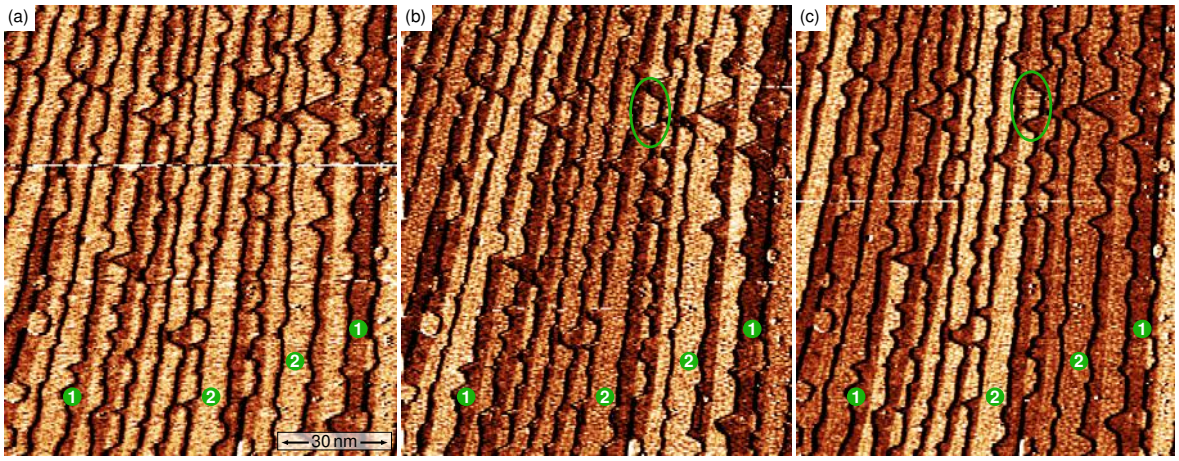

Figure 3.28: Differential conductance maps of the same area of about 1.6 monolayers of Co on Ir(111), imaged with three different tips at room temperature. The appearance of a two-levels contrast which is almost completely symmetric in (b) and (c) suggests that the double layer Co areas are magnetic, and imaged with two tips with opposite magnetization components along the sample magnetization direction. The green ellipse indicate an area where the contrast is not symmetric in (b) and (c), possibly because of a change in magnetization in that area. *Measurement parameters*: -250 mV, 300 pA, Cr bulk tip, 300 K.

Figure 3.28 shows the same area of a sample with monolayer and double layer Co areas on Ir(111), imaged at room temperature with three different tips, which are

obtained by applying short voltage pulses in order to modify the tip apex. Figure 3.28(a) shows a $\mathrm{d}I/\mathrm{d}U$ map where the contrast on each layer is constant throughout the area. In Fig. 3.28(b) the Co double layer areas have two distinct levels of $\mathrm{d}I/\mathrm{d}U$ contrast, suggesting that the tip might now have a non-zero spin polarization. Figure 3.28(c) shows that the contrast on the Co double layer areas is now inverted with respect to (b), except for one point indicated with a green ellipse. This suggests that, while in (a) the tip has no significant spin polarization, in (b) and (c) the tip is spin-polarized, and its magnetization component parallel to the sample magnetization changes sign in the two images. In the area indicated by the ellipse, the sample magnetization is probably switching, maybe as a consequence of the tip scanning over it. Additionally, no change in $\mathrm{d}I/\mathrm{d}U$ signal of the Co monolayer was observed, also when imaging it at different bias voltages. These results provide a strong indication that the Co double layer on Ir(111) is magnetic at room temperature. The two levels of contrast, inverting in intensity with different tips, suggest that the sample magnetization has an out-of-plane component. The Co monolayer did not show any signs of magnetism at room temperature.
It was not possible to image stable single domain walls, as every time the tip would scan across them they would move to a different position. This could be explained by an increased mobility of the walls at room temperature [115], or by a large stray field from the tip, due for example to a Co cluster on its apex.

3.6 Summary

This Chapter presented a study of several magnetic properties of Co epitaxial films deposited on two heavy metal substrates, namely Ir(111) and Pt(111). The films exhibit large out-of-plane magnetic domains, whose size and shape can be strongly influenced by the sample's morphology, especially for films with one and two Co atomic layers. For thicker films of Co/Ir(111) the domains seem to become less constrained by terrace edges and other pinning centers, resulting in an increased domain size. The domain walls separating the observed domains are found to have a width on the order of a few nanometers, which increases with the thickness of the Co films. The dislocation network does not seem to influence the equilibrium position of the walls, which are mostly located at atomic constrictions. The walls also possess a unique rotational sense, induced by the DMI at the interface between Co and the substrate. Their absolute sense of rotation is investigated, for the Co/Ir(111) case, by observing the wall tilting in in-plane magnetic field, and the results indicate that the walls are rotating clockwise, in agreement with DFT calculations. With a Pt layer on top of the Co/Ir(111), the magnetic domains are still out-of-plane magnetized, and the walls are found to be energetically unfavourable on the Pt/Co bilayer. DFT calculations show that the DMI energy is increased in the bilayer system, although the total DMI stems mostly from the Pt/Co interface, with a negligible contribution from the Co/Ir interface.

Finally, measurements at higher temperatures reveal that the monolayer Co on Ir(111) is still magnetic at liquid nitrogen temperature, while in the double layer Co the magnetism is preserved up to room temperature. The presence of domain walls a few nanometers wide in atomically thin magnetic films at room temperature can be of great relevance for spintronic devices such as racetrack memories [4].

Chapter 4

Domain walls and zero field magnetic skyrmions in Rh/Co/Ir(111)

In the previous Chapter it has been shown that magnetic domain walls, due to their positive energy per unit length, tend to be found in constrictions of the magnetic film, where their length is minimized. In the case of Co/Ir(111) the domain wall energy is modified by a non-magnetic top layer, namely Pt. The walls are observed to avoid, when possible, the Pt/Co bilayer, and to prefer longer paths on the uncovered Co. Adding a cover layer has already been proven to be a very effective way to modify the magnetic state of ultrathin films [12, 76, 116], as the modifications of the films' magnetic parameters induced by the top layer lead to different magnetic configurations. This Chapter presents the results obtained by depositing a different top layer, now Rh instead of Pt, on a Co monolayer on Ir(111). Under specific growth conditions, this system is found to favour the creation of non-collinear magnetic objects, in zero magnetic field, such as domain walls and magnetic skyrmions, the latter with diameters below 5 nm. These objects are easily detectable due to a significant electronic contribution of the domain walls to the system's density of states over a wide range of bias voltages. Additionally, by applying high bias voltages with the STM tip it is possible to move such magnetic objects, and to induce them starting from a ferromagnetic background.
Some of the results presented in this Chapter constitute part of a joint publication with colleagues from the University of Kiel, who have performed DFT calculations to model the Rh/Co/Ir(111) system, as well as spin-dynamics simulations to verify the stability conditions of different non-collinear objects [117].

4.1 Growth of a Rh top layer

The Co monolayer on Ir(111) is grown following the procedure already described in Section 3.2.1, and the Rh can be grown on top of the Co at different temperatures. Figure 4.1 shows the growth of a Co monolayer on Ir(111) (Figs. 4.1(a) and (b)) and

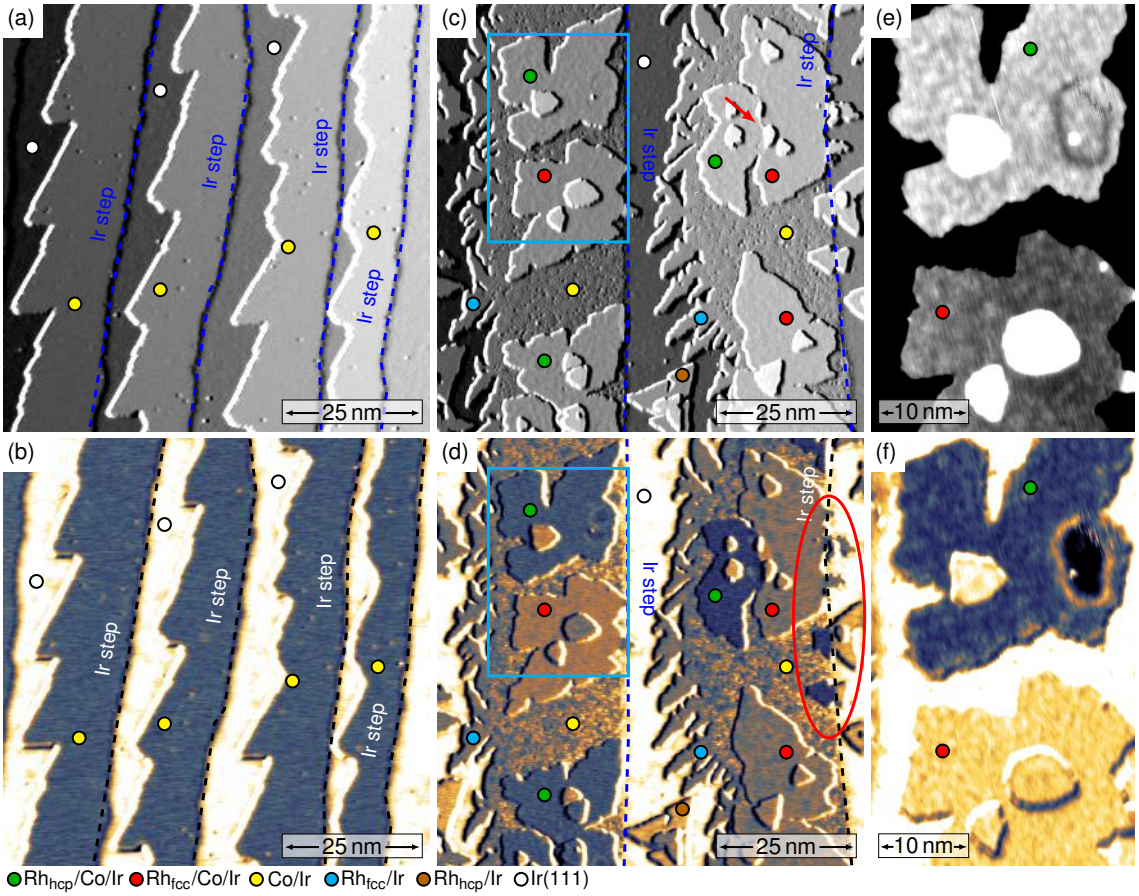

Figure 4.1: STM constant-current ((a), (c)) and differential conductance ((b), (d)) maps of a Co/Ir(111) and Rh/Co/Ir(111) sample, respectively. Map (d) is also spin-polarized. The differentiated height signal has been added to the height maps to increase visibility of the structural details. The Co layer appears dirtier after the Rh deposition. The Rh islands on Co/Ir(111) present some roughness in the constant-current map, which could be a sign of intermixing. The red arrow in (c) indicates a stacking fault line. The red ellipse in (d) indicates Rh/Ir(111) islands connected to Rh/Co/Ir(111) areas on the adjacent terraces. (e), (f): STM constant-current and spin-polarized differential conductance maps of the area indicated in (c) and (d) by the rectangles. A roughly circular domain is visible in the top island, recognizable in $\mathrm{d}I/\mathrm{d}U$ thanks to both TMR and electronic effects (see Section 4.2.2). The domain wall separating the small object from the surrounding domain is also visible in (e) as a dark line. Also in the rest of the two Rh/Co islands, where no magnetic structures are present, neither the topography nor the $\mathrm{d}I/\mathrm{d}U$ signal are perfectly uniform. *Measurement parameters*: 800 pA, 4 K, Cr bulk tip; (a) to (d): -400 mV; (e), (f): -250 mV.

the growth of a Rh layer on top of it (Figs. 4.1(c) and (d)), deposited with the substrate at room temperature. At the bias voltage used the different layers can easily be identified from their $\mathrm{d}I/\mathrm{d}U$ signals. The Co layer appears dirtier in Fig. 4.1(c)

than in Fig. 4.1(a), similarly to what has been observed for the uncovered Co monolayer after Pt deposition (see Section 3.4.1). The exact source of contamination has not been identified, but possible candidates are both Rh atoms embedded in the Co surface, as well as by-products of the evaporation of the Rh, such as hydrogen. As the Co monolayer does not completely cover the Ir(111) surface, the Rh grows both on top of the Co and on the Ir substrate. In the latter case it tends to grow directly from the Co step edges producing areas with irregular dendritic edges. No gap in the constant-current height signal is visible between Rh and Co, indicating that the Rh follows the stacking of the Co monolayer, i.e. the fcc stacking. Isolated Rh islands on Ir(111) are also visible, and they possess either irregular edges, similar to those of the Rh connected to the Co areas, or compact straight edges. The observed $\mathrm{d}I/\mathrm{d}U$ contrast is different for these two Rh areas, suggesting that they correspond to differently stacked Rh/Ir islands. Additionally, the approximately triangular shapes formed by such islands point along different directions, depending on the $\mathrm{d}I/\mathrm{d}U$ contrast. It is therefore concluded that all Rh/Ir areas with irregular edges correspond to fcc-stacked areas, and hcp-stacked islands grow with more compact edges. The stacking of Rh islands on Co/Ir(111), which present different $\mathrm{d}I/\mathrm{d}U$ signals at several bias voltages, can then be deduced from the stacking of the Rh/Ir(111) islands connected to them, without dislocation lines in between (see red ellipse in Fig. 4.1(d)).
In Fig. 4.1(d) two levels of contrast are visible for each stacking of Rh/Co/Ir(111), corresponding to islands with opposite magnetization (the details of the magnetic properties will be discussed in Section 4.2; for now the reader should know that the magnetic domains on Rh/Co/Ir(111) are out-of-plane ferromagnetic). Rh grows pseudomorphically on top of the Co, without signs of reconstruction lines. However, as shown by Fig. 4.1(e), the height signal on the Rh/Co areas is not uniform, and creates a height modulation between 5 and 10 picometers. At specific bias voltages a modulation of the $\mathrm{d}I/\mathrm{d}U$ signal for both Rh stackings is also visible, as observed in Fig. 4.1(f). No obvious spatial correlation between the inhomogeneities in the constant-current and $\mathrm{d}I/\mathrm{d}U$ maps has been found. The origin of such roughness could be a certain degree of intermixing of Rh with the underlying Co, or the growth of the Rh film on an inhomogeneous Co layer. The latter one presents indeed several defects, as visible in the uncovered Co areas of Figs. 4.1(c) and (d), and therefore an additional Rh layer on top might show signs of the buried defects.

To understand the role of the substrate temperature on the growth of the Rh layer, Rh has been deposited at three different temperatures, and the results are presented in Fig. 4.2. To deposit Rh at lower substrate temperatures, the sample was cooled down to 4.2 K after the Co deposition by inserting it in a low-temperature STM. Once the Rh evaporator had reached the desired deposition parameters, the sample was taken out of the STM and quickly brought in front of the evaporator, in order to deposit Rh while the sample temperature was still well below room temperature.

The result is shown in Figs. 4.2(a) and (b): the Rh islands on Co/Ir(111) present, in both stackings, a highly irregular shape, with dendritic edges similar to those visible on Rh_{fcc}/Ir(111) in Fig. 4.1. Such islands tend to grow separately from each other, posing a challenge to the growth of large Rh/Co areas. Figures 4.2(c) and (d) shows a similar amount of Rh as in (a) and (b), but now deposited at room temperature on Co/Ir(111). This is achieved by simply waiting enough time after the Co deposition to let the sample cool down after the initial annealing, typically 90 minutes or more. The shape of the Rh islands is now remarkably different, with more straight edges and larger patches connected together. On the Rh_{hcp}/Co/Ir(111) islands bright lines

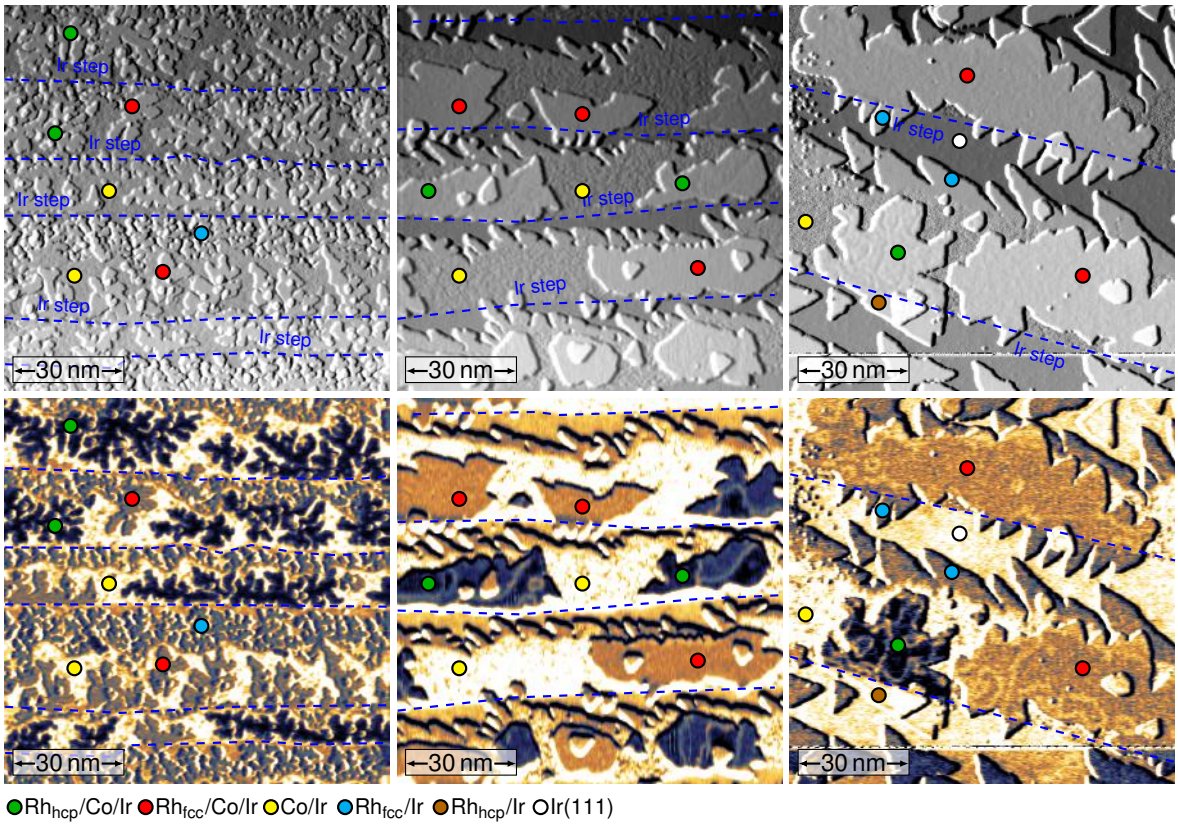

Figure 4.2: STM constant-current and differential conductance maps of Rh/Co/Ir(111) samples with different Rh deposition temperatures. The derivative of the topographic signal has been added to the topography signal to help identifying the different layers. (a), (b): sample has been cooled down inside the STM before the Rh deposition. (c), (d): Rh is deposited 120 minutes after the annealing procedure, when the sample is at room temperature. (e), (f): Rh is deposited directly after the Co deposition, when the substrate is still above room temperature. Map (d) is spin-polarized, and domain walls are visible in (d) on Rh_{hcp}/Co/Ir(111) as bright lines, due to electronic effects (see Section 4.2.2). The same effects allow to observe domain walls on both stackings of Rh on Co/Ir(111) in (f), with a tip with no significant spin polarization. *Measurement parameters*: -250 mV, 1 nA, 4 K, Cr bulk tip.

separate areas with different $\mathrm{d}I/\mathrm{d}U$ signal, and also form a small circular object, while such lines are not visible in Fig. 4.2(b). Figures 4.2(e) and (f) now show the result of depositing Rh directly after the Co deposition, with the substrate still above room temperature due to the previous annealing procedure. Now on both stackings of Rh on Co/Ir(111) it is possible to recognize bright lines, running across the islands and forming isolated objects, as shown in Fig. 4.2(f). The properties of these bright lines, which will be shown to be magnetic domain walls, will be investigated in Section 4.2. In this sample, no significant difference is visible as regards the growth of Rh/Co/Ir(111) with respect to the sample shown in Figs. 4.2(c) and (d); however, the $\mathrm{Rh}_{\mathrm{fcc}}$/Ir(111) areas grow now with straight edges, similarly to the hcp areas of Rh/Ir(111). It can therefore be concluded that the substrate temperature plays an important role in determining the shape of the Rh islands both on Ir(111) and on Co/Ir(111). Additionally, such temperature also influences the magnetism of the film, as demonstrated by the absence or presence of magnetic structures (the bright lines) in samples with different deposition temperatures. A comparison of the inhomogeneity of the Rh/Co layers in the different samples has not proven insightful to pin down the exact origin of the non-uniform contrast in both Co and Rh/Co layers. Measurements of surface corrugation have shown differences up to 10 pm between the different samples, but changes in measured corrugation on a similar scale could be also explained by slightly different tip apexes [118, 119], as the measurements on the different samples were not performed with the same tip apexes. From these data alone it is therefore not possible to conclude whether the Rh deposition temperature has an effect in the observed inhomogeneity of the Rh/Co/Ir(111) films.
Samples of Rh/Co/Ir(111) where the Rh has been deposited on a pre-cooled substrate have not been studied further, as they did not show any sign of non-collinear structures. The reason for this is not completely understood, but it is reasonable to assume that a different degree of intermixing between Co and Rh, due to the lower substrate temperature, is responsible for different magnetic properties in such films. For the results presented in the rest of this Chapter, Rh has been deposited at room temperature, unless stated otherwise.

4.2 Non-collinear magnetic structures in Rh/Co/Ir(111)

As already mentioned in the previous Section, some of the Rh/Co/Ir(111) areas display a high density of magnetic domain walls, which can be easily seen as bright lines in $\mathrm{d}I/\mathrm{d}U$ maps also with tips without a significant spin-polarization thanks to a large electronic contrast. Some of these walls form objects with approximately circular shape and with diameter below 5 nm, which are found to be stable in a ferromagnetic background at zero magnetic field. In this Section several properties of non-collinear objects in Rh/Co/Ir are investigated.

4.2.1 Response to an applied magnetic field

Figure 4.3 gives an overview of the virgin magnetic state of a Rh/Co/Ir(111) sample. In this image forward and backward scans are taken at different bias voltages, and the corresponding $\mathrm{d}I/\mathrm{d}U$ maps are shown in Figs. 4.3(a) and (b), respectively. In the forward scan, at a bias of -400 mV, uncovered Co/Ir areas with two different contrast levels are visible, indicating that the tip has out-of-plane magnetic sensitivity. At this bias Rh hcp and fcc areas on top of the Co are easily distinguishable due to the very different $\mathrm{d}I/\mathrm{d}U$ signal. Additionally, Rh fcc areas located on top of Co stripes with opposite magnetization present two different contrast levels, and each island displays a roughly constant $\mathrm{d}I/\mathrm{d}U$ signal. For the $\mathrm{Rh_{hcp}}$/Co/Ir(111) the arrangement of contrast levels is more complex: islands located on either bright or dark Co areas present a dominating bright or dark contrast level, respectively, but in most of them the two $\mathrm{d}I/\mathrm{d}U$ signals coexist. Areas with different $\mathrm{d}I/\mathrm{d}U$ signal are separated by bright lines, which will be shown to be magnetic domain walls. In the backward scan, at a bias of -250 mV, the differently magnetized Co/Ir(111) areas are

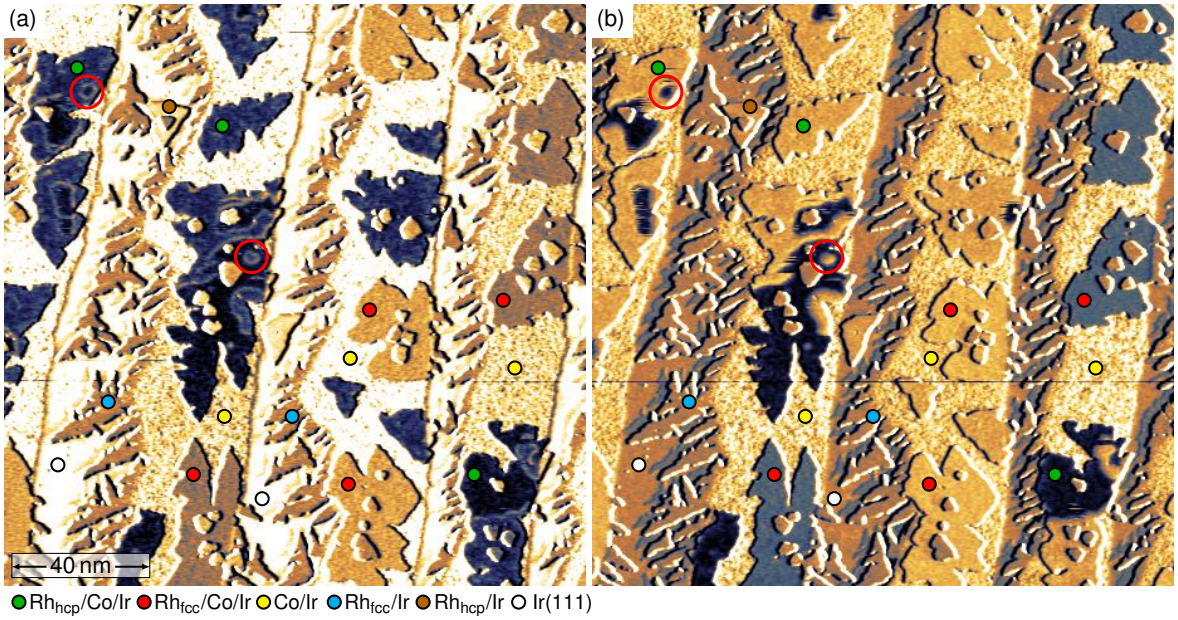

Figure 4.3: (a), (b): Spin-resolved differential conductance maps of a Rh/Co/Ir(111) sample at different bias voltages. The two-levels contrast observed on the Co/Ir(111) terraces indicates that the tip has a significant out-of-plane magnetic sensitivity. Two levels of contrast are also visible for both stackings of Rh on Co/Ir(111): in the fcc case each island has a uniform $\mathrm{d}I/\mathrm{d}U$ signal, while in the hcp case the two contrast levels coexist in the same islands. The red ellipses indicate magnetic skyrmions of both polarities. Note that a slight double tip signal is visible above the Rh/Ir islands. *Measurement parameters*: 800 pA, 4 K, Cr bulk tip; (a): -400 mV; (b): -250 mV. Adapted from [117].

barely identifiable with this tip, but for each of the two Rh stackings on Co the difference between the two contrast levels is clearly recognizable. Additionally, small circular objects, with diameters on the order of 3 nm, are visible in $Rh_{hcp}/Co/Ir(111)$ islands of both magnetization orientations, and are marked by the red ellipses in Fig. 4.3. Objects of this size and shape will be shown in Section 4.2.4 to be magnetic skyrmions.
To verify whether the observed contrast has a magnetic origin, an out-of-plane magnetic field is applied. Figure 4.4(a) shows a different area of the same Rh/Co/Ir(111) sample, where the two different contrast levels are not as clearly visible as in Fig. 4.3, but the domain walls separating them are easily identifiable. Additionally, there is one magnetic skyrmion on a $Rh_{hcp}/Co/Ir(111)$ island (see yellow ellipse in Fig. 4.4), with diameter below 3 nm. When applying 0.5 T in the out-of-plane direction, many walls in the hcp stacking move, creating large areas with uniform $\mathrm{d}I/\mathrm{d}U$ contrast. Increasing the magnetic field to +1.5 T results in the vast majority of the Rh/Co islands being now without any wall, with the exception of one island where a small bright line is still visible (see green ellipse in Fig. 4.4(c)); furthermore, the isolated skyrmion on the left side has not changed at all under the effect of the magnetic field. When

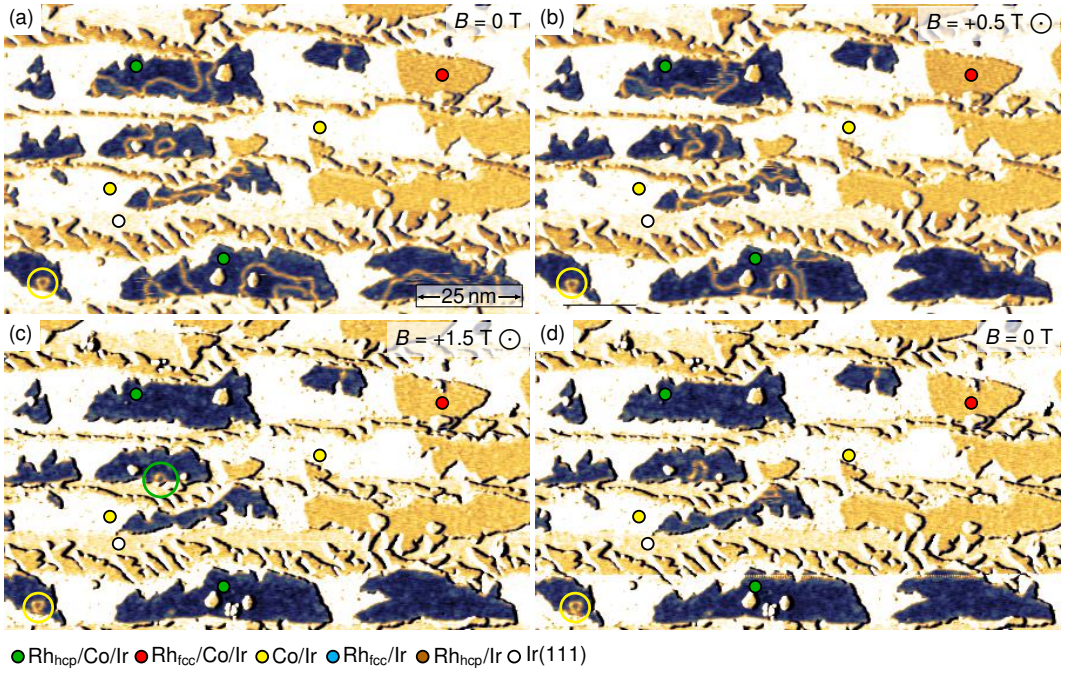

Figure 4.4: Spin-polarized differential conductance maps of the same Rh/Co/Ir(111) area under different applied magnetic fields. Most of the islands become single-domain ferromagnetic once a field of 1.5 T is applied (c), and remain so once the field is brought back to 0 (d). One isolated skyrmion, marked by the yellow ellipse, is unaffected by the magnetic field. Adapted from [117] *Measurement parameters*: -250 mV, 800 pA, 4 K, Cr bulk tip.

bringing the magnetic field back to 0 T, the islands which are free of domain walls remain mostly so, while the wall indicated by the green ellipse has expanded, as visible in Fig. 4.4(d). The two-levels contrast observed for Rh/Co/Ir(111) in Fig. 4.3, combined with the observed response of the sample to an out-of-plane magnetic field, allows to conclude that the areas with different $\mathrm{d}I/\mathrm{d}U$ contrast are out-of-plane magnetic domains, separated by domain walls which appear as bright lines due to an additional contrast mechanism, either TAMR or NCMR (see Section 2.2.2). The isolated skyrmion, probably pinned to a defect, has not changed noticeably in size or shape under the effect of the applied magnetic field.

Magnetism in samples at higher Rh deposition temperatures Non-collinear spin structures can also be observed in the $\mathrm{Rh_{fcc}}$/Co/Ir(111) areas, but their density is rather low in samples where the Rh is deposited at room temperature. As previously mentioned in Section 4.1, increasing the Rh deposition temperature results in a larger density of domain walls in the fcc Rh stacking, while in the hcp stacking the density does not change noticeably. Figures 4.5(a) and (b) displays magnetic domain walls in both stackings of Rh on Co/Ir, having deposited Rh directly after the Co deposition, i.e. when the substrate is still above room temperature. The tip does not show indications of a net spin polarization, but the walls are still recognizable as bright lines thanks to the additional contrast mechanism, which will be discussed in further details in the following Section. Different bias voltages are necessary to observe the domain walls in the two Rh stackings, as can be expected from the different local density of states in the two Rh stackings. Magnetic skyrmions, as the one visible in Fig. 4.5(c), are also found in $\mathrm{Rh_{fcc}}$/Co/Ir(111) areas of the same sample, coexisting with domains walls and creating a complex arrangement of non-collinear structures. The reason for the appearance of such objects in $\mathrm{Rh_{fcc}}$/Co/Ir at higher deposition temperature is presumably a different amount of intermixing between Co and Rh. In this type of samples the substrate temperature cannot be controlled precisely, as it strongly depends on the amount of time between annealing and Rh deposition, which might vary slightly in different preparations. The results presented below will regard mostly samples where the Rh has been deposited at room temperature, where the degree of intermixing is lower and the deposition temperature can be controlled more accurately.

4.2.2 Contrast mechanisms and unique rotational sense

Magnetic objects imaged through a combination of TMR and electronic effects such as TAMR and NCMR can appear very differently depending on the respective contributions to the $\mathrm{d}I/\mathrm{d}U$ signal of the different effects, and on the tip magnetization direction. Figures 4.6(a) to (c) show one roughly circular magnetic domain imaged with the same tip at three different bias voltages. In Fig. 4.6(a), at -300 mV, the $\mathrm{d}I/\mathrm{d}U$ signal is dominated by the contribution from the TMR, with a tip mostly sensitive

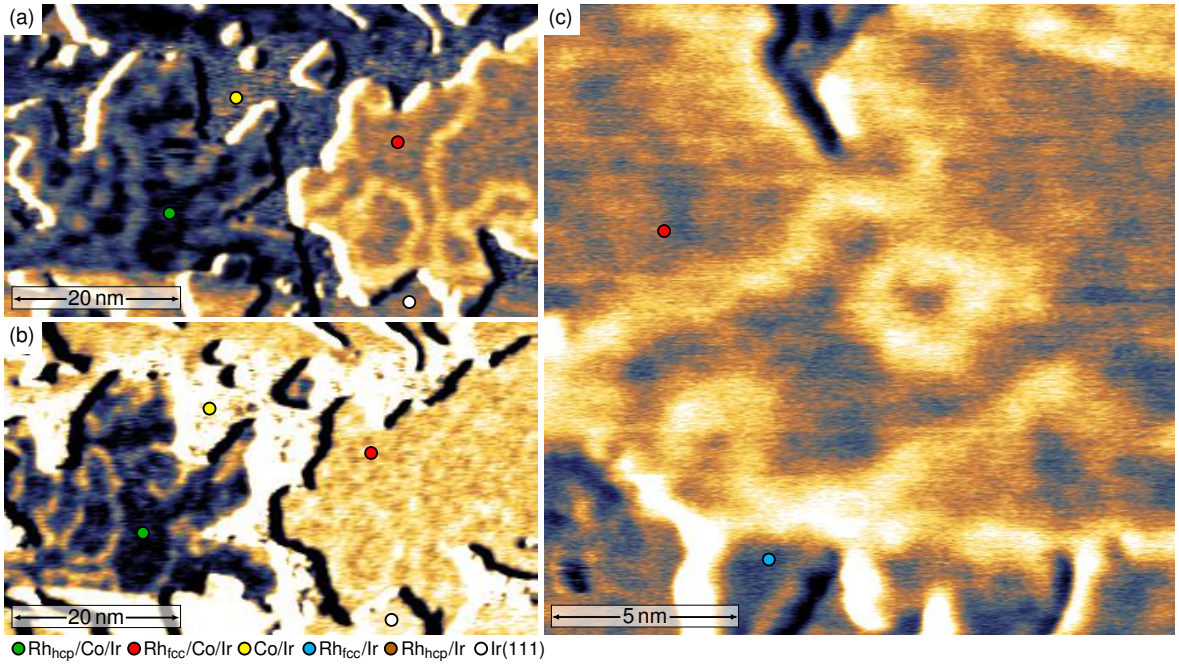

Figure 4.5: Differential conductance maps of a Rh/Co/Ir(111) sample, where the Rh has been deposited having the substrate above room temperature. Domain walls in the different Rh stackings are visible as bright stripes, at different bias voltages ((a) and (b)). Magnetic skyrmions can also be found in the fcc Rh stacking (c), similar the ones observed in Figs. 4.3 and 4.4 for the hcp Rh stacking. *Measurement parameters*: 1 nA, 4 K, Cr bulk tip; (a), (c): +250 mV; (b): -250 mV

to the out-of-plane magnetization component. Only a weak bright stripe indicates the contribution to the domain wall's contrast due to electronic effects. In Fig. 4.6(b), at -100 mV, no TMR signal is visible anymore, and only the domain wall can be recognized due to its bright contrast. At 100 mV, in Fig. 4.6(c), there is a weak TMR signal, as the small circular domain appears slightly brighter than the surrounding domain, but the wall's electronic contrast is still dominating. The presence of a large electronic signal on non-collinear structures in a broad range of bias voltages allows to easily observe such objects also in absence of strongly spin-polarized tips.
Figures 4.6(d) and (e) now show three magnetic objects imaged at the same bias voltage using different tips. In Fig. 4.6(d) the tip does not have a significant spin sensitivity, and only the domain walls are visible. In Fig. 4.6(e) the tip is sensitive to both the out-of-plane and to an in-plane component of the sample magnetization, indicating that the tip magnetization direction is neither fully out-of-plane nor fully in-plane oriented. With such a tip the three small domains appear darker than the oppositely pointing domains surrounding them, similarly to the small domain in Fig. 4.6(a). In this case, however, also the domain walls show a TMR contribution, which depends on the relative alignment of tip's and walls' in-plane magnetization directions. The domain walls in Fig. 4.6(e) show a bright contrast on the right side,

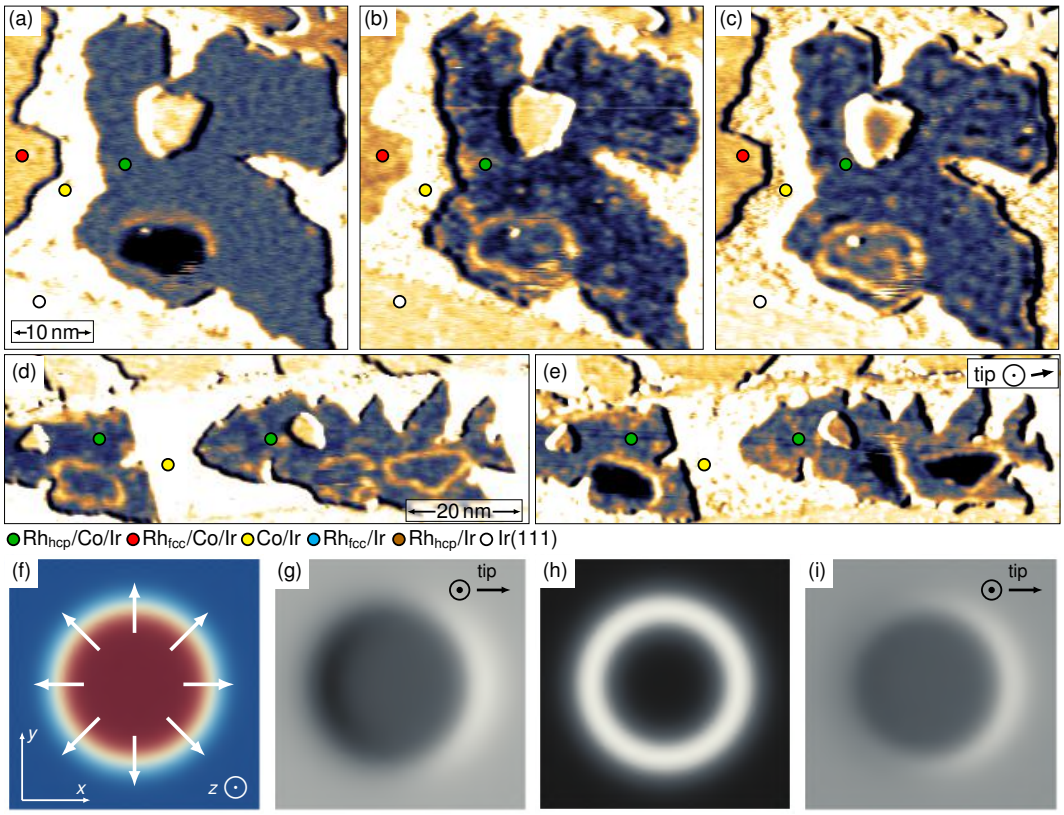

Figure 4.6: (a) to (c): Spin-polarized differential conductance maps at different bias voltages of an island of $Rh_{hcp}/Co/Ir(111)$. A small isolated magnetic object is clearly recognizable from the TMR contrast in (a), and at different bias voltages its contour is still visible, due to either TAMR or NCMR. (d), (e): Differential conductance maps of two $Rh_{hcp}/Co/Ir(111)$ islands imaged using different tips. In (d) there is no sign of a significant spin polarization, and the magnetic structures are only visible due to their electronic contrast. In (e) the tip has a canted magnetization direction, as indicated in the top right corner, which is combined with the electronic contrast present at the considered bias, resulting in a $\mathrm{d}I/\mathrm{d}U$ signal for the walls going from hardly visible to very bright. The similar arrangement of contrast levels for the three magnetic objects indicates that they possess walls with same sense of magnetization rotation. (f): Sketch of the magnetization in the z direction for a circular magnetic domain with Néel-type domain walls. The white arrows indicate the direction of the in-plane component of the walls. (g) to (i): corresponding contrast levels induced by TMR (g), NCMR (h), and a combination of the two (h). The tip direction, which is neither fully out-of-plane nor in-plane, but rather in a canted position, is drawn on the top right corners. *Measurement parameters*: 800 pA, 4 K, Cr bulk tip; (a): -200 mV; (b): -300 mV; (c): 100 mV; (d), (e): -250 mV. (d) and (e) are adapted from [117].

and are hardly visible on the left side of each of the three magnetic objects, which possess identical out-of-plane contrast in the center. The same $\mathrm{d}I/\mathrm{d}U$ contrast arrangement observed for the three objects, in both out-of-plane and in-plane direc-

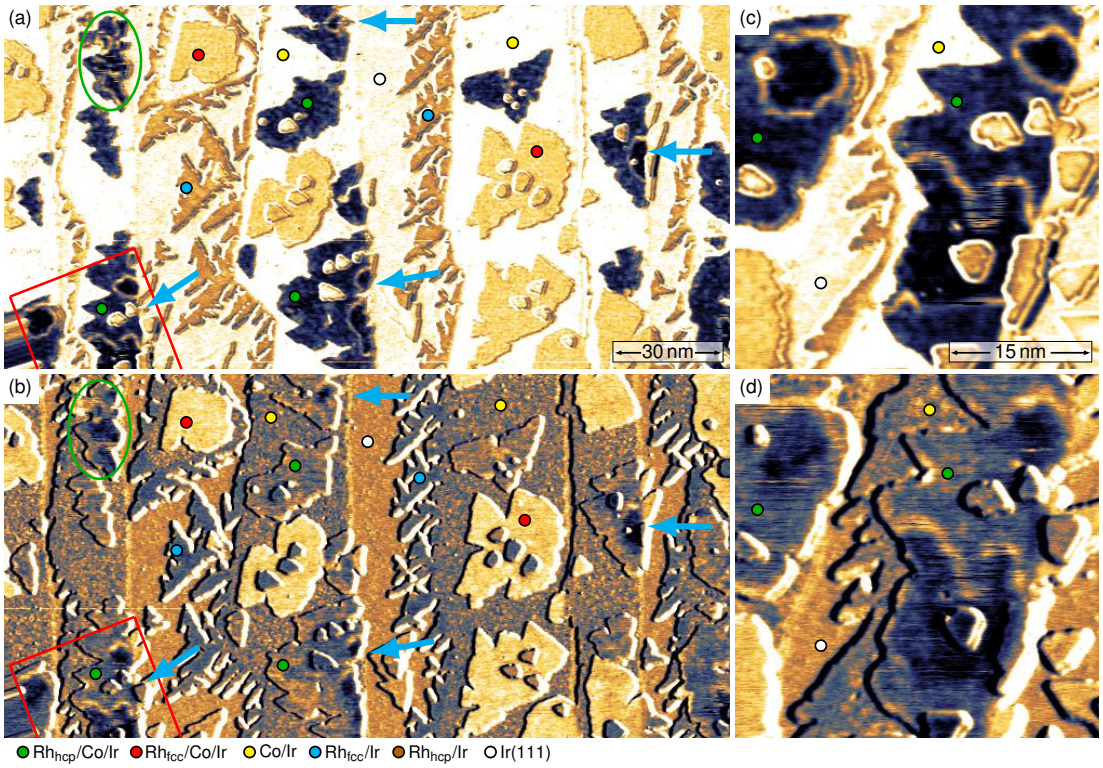

Figure 4.7: (a), (b): Spin-polarized differential conductance maps of a Rh/Co/Ir(111) sample. The magnetic objects are visible in the forward scan thanks to the electronic contrast on their walls (a), while in the backward scan the canted magnetization direction of the tip allows to recognise them as dark areas with a bright edge on their upper part (b). This contrast arrangement is the same for all the magnetic objects in the scan area (indicated by the blue arrows), excluding those in the area marked by the green ellipse, which are not in a stable position while scanning over them. The area in the red rectangle is imaged at higher resolution in (c) and (d). The image distortion in the bottom left corner of (a) and (b) corresponds to the limit of the STM scan area. *Measurement parameters*: 800 pA, 4 K, Cr bulk tip; (a), (c): -250 mV; (b), (d): 350 mV.

tions, shows that they possess the same spin structure: specifically, their in-plane spins are oriented in the same direction, meaning that the domain walls have the same rotational sense. The effects of the different contrast mechanisms are sketched, for a circular magnetic domain with Néel domain walls (Fig. 4.6(f)), in Figs. 4.6(g) to (i) : panel (g) shows the TMR contrast on such an object using a tip with canted magnetization direction, sensitive to the magnetization components in x and z directions; panel (h) depicts the effect of pure electronic contrast due to NCMR assuming a positive contribution (a similar sketch would result by considering TAMR instead, as shown in Section 2.2.4); panel (i) displays a combination of the contrasts in the previous two panels, resulting in a $\mathrm{d}I/\mathrm{d}U$ signal qualitatively similar to what is observed in Fig. 4.6(e).

As already mentioned in Section 2.1.3, the interfacial DMI stabilizes Néel-type over Bloch-type non-collinear magnetic structures, such as domain walls and skyrmions, which possess a fixed sense of magnetization rotation. To investigate whether the magnetic structures in Rh/Co/Ir(111) also have this property, it is necessary to image several of them with the same tip and verify if the observed contrast levels are in agreement with the hypothesis of a unique rotational sense. This is shown in Fig. 4.7 for a large area of Rh/Co/Ir(111), imaged at different bias voltages for forward and backward scans, using a tip that has a canted magnetization direction, i.e. it is sensitive to both the out-of-plane and one in-plane sample magnetization components. In Fig. 4.7(a) the TMR signal from the tip's spin-polarization is weak, and the magnetic objects are identifiable mostly because of the electronic contrast from their domain walls. In Fig. 4.7(b), at a different bias voltage, a larger TMR effect allows to observe the magnetic objects in the Rh hcp stacking as dark spots in a brighter background. Their position is indicated by the blue arrows. The objects also display an additional bright contrast on their top part, which is not visible on their bottom part. This asymmetry in the contrast levels is once again due to a combination of an in-plane tip sensitivity and an additional $\mathrm{d}I/\mathrm{d}U$ signal on the walls due to either TAMR or NCMR. All the magnetic objects in the scan area consistently present such asymmetry, and a closer view on some of them is given in Figs. 4.7(c) and (d). Note that the domain walls in the island in the top left corner (green ellipses in Figs. 4.7(a) and (b)) have been excluded from this analysis since they move while the tip scans over them, not allowing to determine their exact position. From the data shown in Figs. 4.6 and 4.7 it is then possible to conclude that in Rh/Co/Ir(111) the observed non-collinear magnetic structures have unique rotational sense, induced by the interfacial DMI. Therefore the domain walls must be of Néel-type.

4.2.3 Spectroscopic properties and comparison with theoretical results

In the case of isolated domain walls, as well as for large circular domains, it is hard to disentangle the effects of TAMR and NCMR in experimental data. Additional insight can be gained by comparing the obtained results with *ab-initio* calculations. Sebastian Meyer and co-workers have performed DFT calculations on both stackings of Rh deposited on Co/Ir(111), as well as spin dynamics simulations based on the obtained magnetic parameters [117]. They found that magnetic skyrmions can be stabilized in zero magnetic field, with large energy barriers that separate them from the ferromagnetic state. The vacuum densities of states (vac-DOS) for a ferromagnetic state and for spin-spirals with different periods have also been calculated, which can be used to study how different amounts of non-collinearity affect the energy-dependent density of states. From the experimental side, a measure of the vac-DOS can be obtained by performing spectroscopy measurements at different positions on the sample, keeping the tip at a fixed height and recording current and

differential conductance while the bias voltage is swept in a certain interval. As described in Section 2.2.1, the measured $\mathrm{d}I/\mathrm{d}U$ signal is then proportional to the vac-DOS at that specific energy, which in turn gives information about the local density of states (LDOS). In this system, spectra measured on the same layers at different positions are found to be very similar. Representative $\mathrm{d}I/\mathrm{d}U$ spectra for each layer are then shown in Fig. 4.8(b), taken at the locations marked in Fig. 4.8(a) with coloured circles. The Co/Ir film (blue curve) shows a maximum around -250 mV, consistent with what has been observed in previous studies [86]. The spectrum measured on $\mathrm{Rh_{fcc}}$/Co/Ir(111) shows an attenuation of the same energy peak (red curve), while in $\mathrm{Rh_{hcp}}$/Co/Ir(111) (green curve) the energy peak is shifted towards the Fermi energy E_F, which corresponds here to an applied bias voltage of 0 V. The $\mathrm{d}I/\mathrm{d}U$ signal at positive biases is higher in Rh/Co/Ir than in Co/Ir, for both Rh stackings.

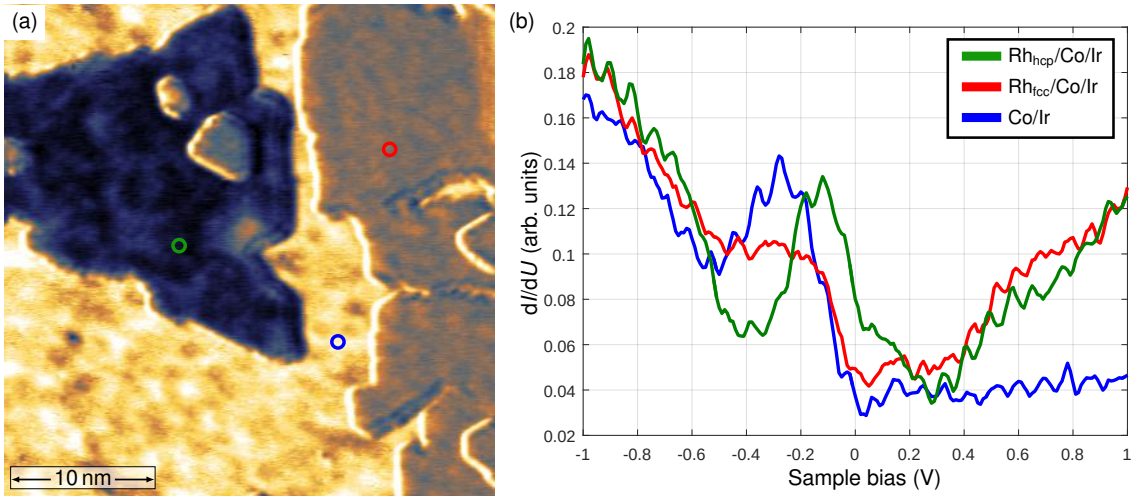

Figure 4.8: (a): Differential conductance map of a Rh/Co/Ir(111) sample. The coloured circles indicate the positions where spectroscopic curves have been measured. (b): Spectroscopic curves of the differential conductance signal, recorded at constant height at the positions indicated in (a). The tip has been stabilized at -1 V on each spot before recording the spectra. The main energy peak visible in uncovered Co/Ir is reduced in intensity in $\mathrm{Rh_{fcc}}$/Co/Ir and shifted to higher energies for $\mathrm{Rh_{hcp}}$/Co/Ir. *Measurement parameters*: -250 mV, 800 pA, 4 K, Cr bulk tip.

Changes in the LDOS on each layer can have various origins: defects and inhomogeneities might alter the electronic structure of the film at specific energies; areas with different magnetization directions can as well produce differences in the measured spectra (TMR), and so can electronic effects such as TAMR and NCMR. As mentioned above, the film's inhomogeneity does not alter significantly the measured vacuum density of states. Then, in order to quantify the changes in the LDOS due to TAMR and NCMR, the magnetic contribution to the $\mathrm{d}I/\mathrm{d}U$ signal has to be removed. Using a Cr bulk tip it is hard to prove that the spectra are not spin-polarized: even when a $\mathrm{d}I/\mathrm{d}U$ map does not show any sign of spin contrast at a specific bias

voltage, such contrast might be visible at different biases, or hidden by other sources of contrast. One way to remove the magnetic signal is of course to use non-magnetic tips, such as W tips. Another option is to average spectra measured on the same layer at positions where the magnetization is pointing in opposite directions: assuming the spectra are only different because of the spin-polarized contribution, one can thus obtain a spin-averaged spectrum. This approach has been used here to obtain spin-averaged spectra on magnetic domains and on domain walls. Figure 4.9(a) shows a $\mathrm{d}I/\mathrm{d}U$ map of two domain walls in $\mathrm{Rh_{hcp}/Co/Ir(111)}$ measured with a tip with a clear out-of-plane spin sensitivity. A small additional in-plane component of the tip magnetization cannot be fully excluded. The circular markers show the positions where $\mathrm{d}I/\mathrm{d}U$ spectra have been recorded. The spectra obtained on the oppositely pointing domains have been averaged, and plotted in Fig. 4.9(b) as a gray line. Similarly, the $\mathrm{d}I/\mathrm{d}U$ spectra recorded approximately at the center of the two consecutive domain walls are averaged and plotted in Fig. 4.9(b) as a green line. Since it has been demonstrated that the walls are of Néel-type and have a unique sense of magnetization rotation (see Section 4.2.2), it is assumed that at their centres the magnetization is fully in-plane and pointing in opposite directions. Fig. 4.9(b) thus displays two spin-averaged spectra, one corresponding to a locally collinear environment (gray curve) and one corresponding to the area in the image with maximal non-collinearity, i.e. at the center of a domain wall (green curve). The peak at E_F in the gray curve is reduced and shifted to higher energies in the green curve. Other modifications of the spectra are visible at different energies both above and below E_F. Since the magnetic signal has been averaged out and the inhomogeneity of the film does not modify significantly the measured spectra, then the modifications between the two obtained curves can be attributed uniquely to the electronic differences between the ferromagnetic state (FM) and a domain wall (DW). A measure of such modifications is the magnetoresistance (MR), defined by [73]:

$$\mathrm{MR} = \frac{\mathrm{d}I/\mathrm{d}U_{FM} - \mathrm{d}I/\mathrm{d}U_{DW}}{\mathrm{d}I/\mathrm{d}U_{FM}}, \tag{4.1}$$

and plotted in Fig. 4.9(c) as a function of the bias voltage.
From these data alone it is not possible to determine whether TAMR or NCMR is responsible for the observed MR. The ferromagnetic domains and the center of the walls are the positions where the non-collinearity is minimal and maximal, respectively. However, they also correspond to the positions where the magnetization is aligned along perpendicular directions, namely in the out-of-plane and in-plane directions, respectively, which is where the TAMR is known to show the largest difference [71]. The obtained asymmetry can, however, be compared with the one obtained from theoretical calculations. Figure 4.9(d) shows the calculated vac-DOS in $\mathrm{Rh_{hcp}/Co/Ir(111)}$ for the out-of-plane ferromagnetic state (gray curve) and for homogeneous spin spirals with different nearest-neighbours' magnetization angles ϕ (coloured curves). The green curve specifically reproduces the spectrum for a ϕ close to the value expected at the center of a domain wall in $\mathrm{Rh_{hcp}/Co/Ir(111)}$. As

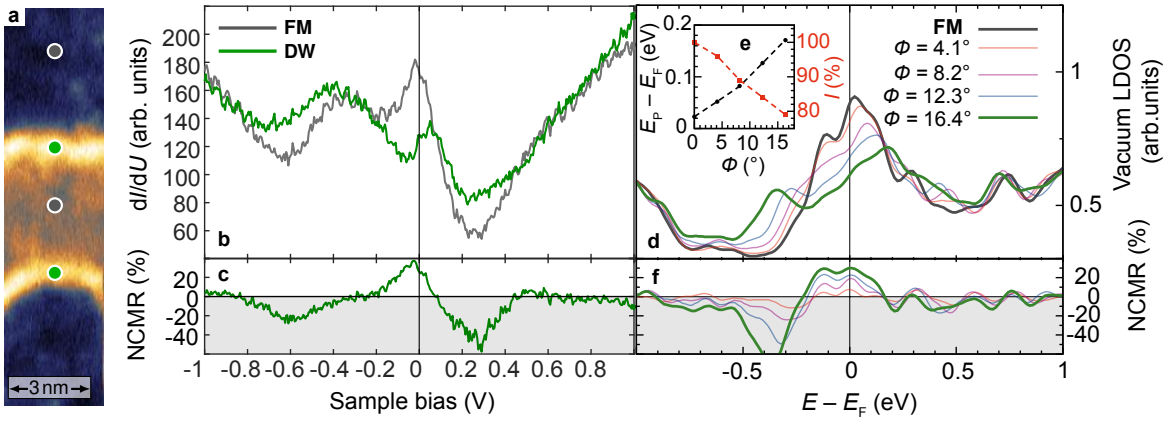

Figure 4.9: (a): Spin-polarized differential conductance map of two domain walls in $Rh_{hcp}/Co/Ir(111)$. The circles indicate the positions where constant-height spectroscopy curves have been measured. Spectra obtained on circles with same colour have been averaged together and plotted in (b) as a function of the applied bias voltage. The obtained curves display the spin-averaged $\mathrm{d}I/\mathrm{d}U$ signal for the collinear ferromagnetic state (label: FM) and for the center of a domain wall (label: DW). The energy peak around E_F shifts towards positive energies and decreases in intensity when going from the gray to the green curve. (c): Magnetoresistance calculated according to Eq. 4.1 between the two spectra in (b). (d): Calculated vacuum density of states of $Rh_{hcp}/Co/Ir(111)$ for a ferromagnetic state (gray curve) and for spin spirals with different nearest-neighbours' angle ϕ (coloured curves). The shift towards positive energies of the main energy peak around E_F reproduces what is observed in panel (b). (e): Energy peak position with respect to E_F (black points) and peak intensity with respect to the FM state (red points) for the calculated spin spiral curves as a function of ϕ. Both such quantities are proportional to the degree of non-collinearity expressed by ϕ. (f): Calculated magnetoresistance between the ferromagnetic vac-DOS and spin spiral vac-DOS with different ϕ. The shape of the curve in (c) shows similarities to the green curve in (f). *Measurement parameters*: (a): -250 mV, 800 pA, 4 K, Cr bulk tip. Adapted from [117].

the degree of non-collinearity, i.e. the nearest-neighbours' angle ϕ, increases, the peak at E_F decreases in intensity and shifts towards higher energies, similarly to what is observed for the experimental curves in Fig. 4.9(b). Figure 4.9(e) shows that both the energy shift and the intensity reduction of this peak are linear with ϕ. In Fig. 4.9(f) the MR defined in Eq. 4.1 is calculated for each of the spin spiral curves with respect to the ferromagnetic state, and plotted with the corresponding colour. This quantity, which shows how the vac-DOS of the ferromagnetic state is modified by tilting nearest-neighbours' spins by an angle ϕ, is taken as a measure of the effect of the NCMR on the density of states. The shape of such MR curves, especially for the green curve, is similar to the experimental curve visible in Fig. 4.9(c), with one peak around the Fermi energy with similar intensity, and negative MR

around it at both positive and negative bias voltages. Similar experiments on different walls imaged with different magnetic tips consistently show MR curves similar to the one presented in Fig. 4.9(c). This comparison shows that the experimentally-observed modifications of the vac-DOS at the center of domain walls are reproduced by the calculated NCMR contrast for spin spirals in this system, displaying a MR effect as large as 40% of the measured $\mathrm{d}I/\mathrm{d}U$ signal. Additionally, the TAMR contrast for $\mathrm{Rh_{hcp}}$/Co/Ir(111) has also been calculated [117]: the calculated MR in the vac-DOS between the ferromagnetic out-of-plane and in-plane states in $\mathrm{Rh_{hcp}}$/Co/Ir(111), which is proportional to the TAMR, is between 3 and 6%, and with an energy-dependent shape which does not correlate with the experimentally observed MR curve. Therefore it is concluded that the observed electronic contrast on non-collinear structures on Rh/Co/Ir is due to NCMR, while TAMR does not contribute significantly to it.

4.2.4 Modelling of domain wall profiles with large electronic contrast

In the previous Section it has been shown that NCMR is the mechanism responsible for the large $\mathrm{d}I/\mathrm{d}U$ signal visible on the non-collinear magnetic structures in this system. This additional electronic signal has to be taken into account when estimating the wall width from a $\mathrm{d}I/\mathrm{d}U$ line profile. The profile of a domain wall can be characterized by the angle φ, i.e. the angle of the spins in the wall with respect to the magnetic easy axis, which is the z axis in this case, pointing in the out-of-plane direction. This quantity has already been defined in Section 2.1.3 as:

$$\varphi(x) = \arccos\left(\tanh\left(\frac{x - x_0}{w/2}\right)\right). \tag{4.2}$$

The NCMR refers to a modification of the LDOS due to a local degree of non-collinearity, i.e. due to spins in adjacent atomic sites which are tilted with respect to each other. A useful parameter to describe this effect is the mean nearest-neighbours angle $\bar{\alpha}$, which is the mean of the angles between one spin direction and those of its six nearest neighbors [74]. In Pd/Fe/Ir(111) it has been observed that the main peak in the LDOS shifts to higher energies and lower intensities when going from the ferromagnetic state to the center of a skyrmion [17]. Additionally, while the intensity of the peak scales roughly linearly with $\bar{\alpha}$, the peak energy shift has in general a non-linear dependence on such angle, due to either a TAMR contribution or to the inhomogeneity of the local spin texture of a skyrmion (with the exception of its center) [73]. In Rh/Co/Ir(111) the vac-DOS calculations from the previous Section have shown that, at the center of a domain wall, both the energy position and the intensity of the main peak in the density of states scale linearly with the nearest-neighbours' angle. One simplified way to describe the domain wall NCMR contribution to the $\mathrm{d}I/\mathrm{d}U$ signal at constant energy, i.e. at constant bias voltage as it is the case for a

$\mathrm{d}I/\mathrm{d}U$ map, is presented here. In a simple 1D model, the mean nearest-neighbours' angle at position x is described by:

$$\begin{aligned}\bar{\alpha}(x) &= \frac{(\varphi(x+\Delta x)-\varphi(x))+(\varphi(x)-\varphi(x-\Delta x))}{2} \\ &= \frac{(\varphi(x+\Delta x)-\varphi(x-\Delta x))}{2} \approx \frac{\mathrm{d}\varphi}{\mathrm{d}x}\Delta x,\end{aligned} \tag{4.3}$$

where neighbouring atomic sites are at a distance of Δx. As a first approximation, the change in $\mathrm{d}I/\mathrm{d}U$ signal can be assumed to be proportional to $\bar{\alpha}$, and therefore proportional to $\mathrm{d}\varphi/\mathrm{d}x$. The limitation of this model will be discussed later in the Section, but for now it provides an analytical formulation for the NCMR contrast across the wall, which can be fitted to the experimental data. Figure 4.10(a) shows a series of three domain walls imaged with a tip with no sign of spin polarization at the considered bias voltage. Small variations in the $\mathrm{d}I/\mathrm{d}U$ signal are visible in each of the out-of-plane domains and are not consistent with a TMR signal due to an out-of-plane tip sensitivity. They are therefore attributed to inhomogeneities of the film (see Section 4.1). Small differences in contrast are sometimes also visible along each wall, but the lack of correlation with a possible in-plane tip direction indicates that the origin might be also in this case the non-uniform electronic structure of the

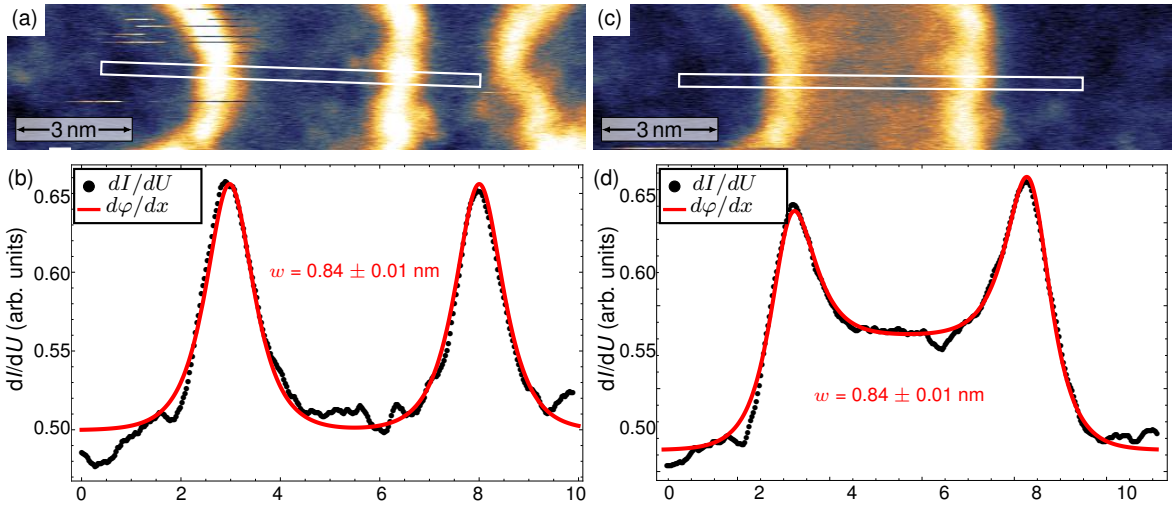

Figure 4.10: (a): Differential conductance map of several domain walls in $\mathrm{Rh_{hcp}/Co/Ir(111)}$. The $\mathrm{d}I/\mathrm{d}U$ signal within the white box is averaged along the short direction and plotted against the long direction in (b). The red line is a fit of the function in Eq. 4.5 to the data points in arbitrary units. (c): Spin-polarized differential conductance map of the same area as (a), with a tip which now possesses a net spin polarization. Note that one of the walls in (a) has now moved out of the scan area. (d): Domain wall profile of the signal inside the white box in (c). Now the fitting function is the one expressed in Eq. 4.6. *Measurement parameters*: -250 mV, 800 pA, 4 K, Cr bulk tip.

Rh/Co/Ir(111) film. The $\mathrm{d}I/\mathrm{d}U$ signal in the white rectangle is plotted in Fig. 4.10(b) as a function of the position across the walls. The two walls can be interpolated considering a 360° domain wall profile [49]:

$$\varphi_{360}(x) = \arccos\left(\tanh\left(\frac{x+x_0+c}{w/2}\right)\right) + \arccos\left(\tanh\left(\frac{x+x_0-c}{w/2}\right)\right), \tag{4.4}$$

where the two walls are centered at $x_0 \pm c$ along the x axis. The fitting function is then:

$$\begin{aligned} y_1(x) &= y_0 + B\frac{\mathrm{d}\varphi_{360}}{\mathrm{d}x} \\ &= y_0 + B\frac{\mathrm{d}}{\mathrm{d}x}\left(\arccos\left(\tanh\left(\frac{x+x_0+c}{w/2}\right)\right) + \arccos\left(\tanh\left(\frac{x+x_0-c}{w/2}\right)\right)\right), \end{aligned} \tag{4.5}$$

where the fitting parameters are y_0, B, x_0, c and w. The red line of Fig 4.10(b) displays the fitting of $y_1(x)$ to the experimental data, having assumed no TMR in the $\mathrm{d}I/\mathrm{d}U$ signal. The procedure yields a wall width of 0.84 nm.

In most of the analysed wall profiles, the NCMR contrast is mixed together with the TMR contrast, due to the tip's magnetic sensitivity. An example is given in Fig. 4.10(c), which displays the same area as Fig. 4.10(a) now imaged with a different tip, which has out-of-plane sensitivity. Note that the rightmost domain wall in (a) has moved to a different position out of the scan area in (c), and is not visible anymore. The domain wall profile inside the white rectangle is plotted in Fig. 4.10(d), and the following function is fitted to the data:

$$y_2(x) = y_0 + A\cos(\varphi_{360}(x) + \phi) + B\frac{\mathrm{d}\varphi_{360}}{\mathrm{d}x}, \tag{4.6}$$

where $A\cos(\varphi_{360}(x) + \phi)$ represents the TMR contribution to the $\mathrm{d}I/\mathrm{d}U$ signal. The additional parameter ϕ accounts for the relative orientation of the tip magnetization with respect to the z axis. The obtained width agrees well with the one obtained in Fig. 4.10(b) on the same walls.

This estimate for the wall width might suffer from a systematic under- or overestimation of the real w due to the simplified modelling of the observed contrast. Specifically, how the $\mathrm{d}I/\mathrm{d}U$ signal at constant bias voltage is affected by a change of the local non-collinearity is highly dependent on the LDOS at that specific bias, and an analytical formulation in terms of $\bar{\alpha}$ might be highly complex, if there would be any. An example of such bias-specific NCMR signal is presented in Fig. 4.11. Here the same domain walls are imaged at two different bias voltages, using the same tip. The different apparent width is attributed to features in the LDOS, at the two bias voltages used, which scale differently with the local non-collinearity, producing a different $\mathrm{d}I/\mathrm{d}U$ signal. One way to investigate the accuracy of the proposed model for the NCMR signal would be to estimate the wall width using the same method used in Section 3.3.2, which assumes a purely TMR-induced $\mathrm{d}I/\mathrm{d}U$ signal. However,

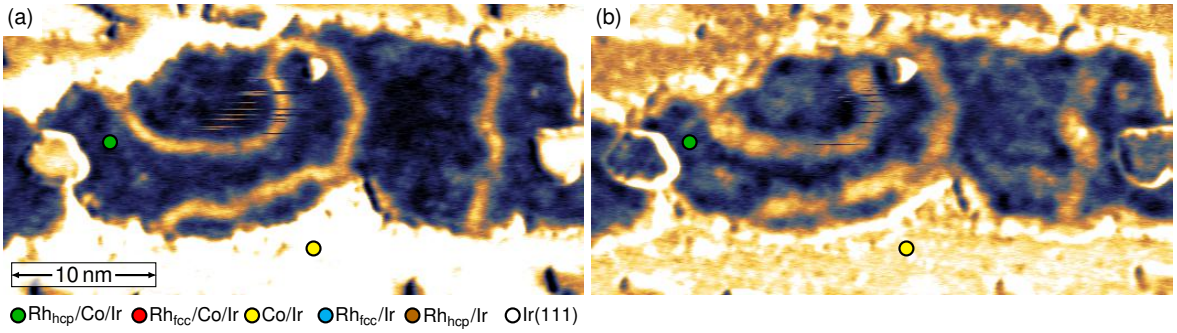

Figure 4.11: (a), (b): Differential conductance maps of the same area of $Rh_{hcp}/Co/Ir(111)$ at different bias voltages. The domain walls appear in the two images as bright stripes with different widths. *Measurement parameters*: 800 pA, 4 K, Cr bulk tip; (a): -200 mV; (b): 250 mV.

to do so walls with vanishing NCMR contrast would be needed, and unfortunately such electronic contrast appears to be present at all of the bias voltages where spin-polarized contrast is also visible. Thus, such a test of the model's validity cannot be performed here. A more accurate modelling of the NCMR contrast across different layers and at different biases would require additional knowledge of the detailed LDOS structure for each layer, and is beyond the scope of this analysis.
Different wall widths at different bias voltages can nevertheless be used as upper and lower bounds for the true value of w, assuming the systematic bias from the model does not shift such bounds excessively. The model bias is assumed to affect equally wall width estimations performed in both Rh stackings and in samples with different Rh deposition temperatures. The obtained minimum and maximum values for w are presented in Table 4.1 for three cases, namely $Rh_{hcp}/Co/Ir$ with Rh deposition at room temperature, and both stackings of Rh on Co/Ir at higher Rh deposition temperature (see Section 4.1). In the case of $Rh_{fcc}/Co/Ir(111)$ the values appear to be less scattered than in $Rh_{hcp}/Co/Ir(111)$, possibly because of a different LDOS, which might produce smaller variations in the apparent wall width with the bias voltage. In the sample where Rh has been deposited at room temperature only rarely is a wall visible on the Rh_{fcc}/Co stacking, and no estimation of its wall width has been possible.

-	Rh_{hcp}/Co - RT	Rh_{hcp}/Co - above RT	Rh_{fcc}/Co - above RT
w_{min} (nm)	0.6	0.8	1.1
w_{max} (nm)	1.1	1.6	1.3

Table 4.1: Minimum and maximum values for the estimated domain wall width, obtained at different bias voltages, for different Rh stackings and deposition temperatures.

The proposed model assumes that the magnetic structures in a 2D magnetic film only change along one spatial direction, and remain unchanged along the other one. This is a reasonable approximation for domain walls as those presented in Fig. 4.10, which run in a straight line across the area considered for the fitting, but it is not in principle valid for magnetic objects with curved domain walls. Consider for example the magnetic objects in Figs. 4.12(a) and (b). A small isolated domain, which has an irregular shape in zero magnetic field (Fig. 4.12(a)), shrinks in size and assumes an almost circular shape once an out-of-plane magnetic field is applied (Fig. 4.12(b)). The $\mathrm{d}I/\mathrm{d}U$ signal inside the white rectangles is plotted against the position across the objects in Figs. 4.12(c) and (d) as black points. In the case of the object in Fig. 4.12(b) it cannot be assumed that the magnetic configuration is unchanged in the direction perpendicular to the line profile, as done above for straight walls, and therefore a fitting procedure using $\mathrm{d}\varphi/\mathrm{d}x$ was not performed. To obtain information about the size of the object and about the domain wall widths a different

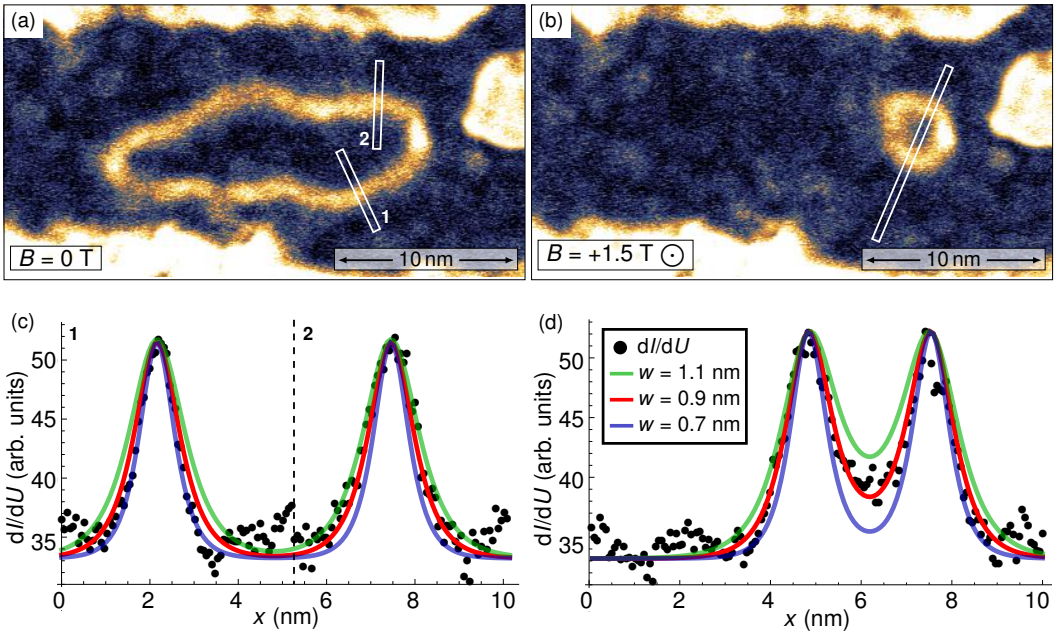

Figure 4.12: (a), (b): Differential conductance maps of the same area of $\mathrm{Rh_{hcp}}$/Co/Ir(111) in zero magnetic field (a) and with +1.5 T applied in the out-of-plane direction (b). The magnetic field makes the domain shrink and assume a circular shape. The two separate white boxes in (a) have been chosen in order to cross the walls perpendicularly. The $\mathrm{d}I/\mathrm{d}U$ signal in the white rectangles is averaged along the short direction and plotted against the long directions in panels (c) and (d) as black dots, in arbitrary units. The coloured solid lines are the calculated NCMR contrast for different values of domain wall width w, having assumed a linear dependence of the $\mathrm{d}I/\mathrm{d}U$ signal from the mean nearest-neighbours' angle. *Measurement parameters*: -250 mV, 800 pA, 4 K, Cr bulk tip. Adapted from [117].

approach was used here. It consists of simulating the spin configuration observed experimentally, and then calculating the expected NCMR contrast as a function of the position across the object. As both Figs. 4.12(a) and (b) show no signs of a net spin-polarization, the $\mathrm{d}I/\mathrm{d}U$ signal from the non-collinear objects comes only from the NCMR, and therefore the calculated curve can directly be superimposed to the experimental data. By manually tuning the parameters of the spin configuration one can achieve an estimate of a few useful quantities, such as the wall width and the object's radius. In Fig. 4.12(a) two separate line profiles are taken for two non-overlapping walls, to ensure the profiles are perpendicular to the wall direction. To reproduce the contrast in these line profiles, a 360° domain wall spin configuration is assumed, i.e. two parallel walls located at a certain distance c [1]. In the case of the circular object in Fig. 4.12(b) the spin configuration is assumed to be that of a magnetic skyrmion. These two configurations are thus described by the following vectors [49, 50]:

$$\vec{S}_{360DW}(x) = \begin{pmatrix} \sin(\varphi_{360}(x, x_0, c, w)) \\ 0 \\ \cos(\varphi_{360}(x, x_0, c, w)) \end{pmatrix}, \quad \vec{S}_{Sk}(x, y) = \begin{pmatrix} \sin(\varphi_{Sk}(\rho, c, w)) \cdot x/\rho \\ \sin(\varphi_{Sk}(\rho, c, w)) \cdot y/\rho \\ \cos(\varphi_{Sk}(\rho, c, w)) \end{pmatrix}, \tag{4.7}$$

where $\rho = \sqrt{(x - x_0)^2 + (y - y_0)^2}$ is the radial distance from the center of the skyrmion, located at the position (x_0, y_0), φ_{360} has been defined in Eq. 4.4, and φ_{Sk} is a two-dimensional version of φ_{360} defined as:

$$\varphi_{Sk}(\rho, c, w) = \arccos\left(\tanh\left(\frac{\rho + c}{w/2}\right)\right) + \arccos\left(\tanh\left(\frac{\rho - c}{w/2}\right)\right). \tag{4.8}$$

The exact dependence of the NCMR contrast on the local non-collinearity remains unknown, and therefore one needs to make an assumption on such a dependence. Similarly to what has been done in Eq. 4.3 for the 1D case, a linear relationship between the mean nearest-neighbours' angle $\bar{\alpha}$ and the NCMR signal is assumed. The blue, red and green lines in Figs. 4.12(c) and (d) show then the calculated NCMR contrast for different values of the domain wall width w, with all the other spin structure parameters unchanged (distance between domain walls in (c): 4.9 nm; skyrmion diameter in (d): 2.8 nm). While in Fig. 4.12(c) all the three calculated profiles reproduce approximately the experimental data, in Fig. 4.12(d) the different domain wall widths produce a very different $\mathrm{d}I/\mathrm{d}U$ signal at the center of the skyrmion, and only the red curve produces a good agreement with the data points. The blue and green curves therefore serve as lower and upper bounds for w at this bias voltage, while the value which would best reproduce the data could only be determined with a fitting procedure. Nevertheless the value of 0.9 nm, corresponding to the red curve, is very close to the value of 0.84 nm obtained assuming the same lin-

[1] The distance c between the walls in the spin simulation is not representative of the real distance between the two walls, as they are not parallel to each other. Nevertheless this spin configuration still allows to reproduce nicely the observed $\mathrm{d}I/\mathrm{d}U$ contrast.

ear dependence between the NCMR contrast and $\bar{\alpha}$ in the 1D case (see Fig. 4.10(b)). Note that the $\mathrm{d}I/\mathrm{d}U$ signal at the center of the small circular object in Fig. 4.12(b) is higher than in the ferromagnetic domain around it. A possible origin of such a difference cannot be explained by a variation in $\mathrm{d}I/\mathrm{d}U$ due to the film's inhomogeneity, as described in Section 4.1, because such a difference is not visible for the larger domain in Fig. 4.12(a). Therefore the higher signal shows that the object lacks a central region of collinear spins, and can thus be called a magnetic skyrmion in the strict sense. Additionally, it also shows that the contrast mechanism involved is effectively NCMR and not TAMR: in the latter case the signals at the center and outside of the sykrmion would have had the same intensity.
To summarize, for the domain walls of Rh/Co/Ir(111) an estimate of the wall width yields values around 0.9 nm. The proposed model simplifies the dependence of the $\mathrm{d}I/\mathrm{d}U$ signal on the local non-collinearity, but nevertheless allows for the estimation of useful quantities such as the skyrmion diameter, which is found to be around 3 nm for the object presented in Fig. 4.12(b). Magnetic skyrmions with similar diameters have also been observed in Pd/Fe/Ir(111) [12, 50] and in the hydrogenated double layer Fe on Ir(111) [120]. It can then be concluded that other isolated objects which possess similar diameter, as the ones presented in Figs. 4.3 and 4.4, are magnetic skyrmions as well, stable in zero magnetic field and surrounded by a ferromagnetic background.

4.3 Tip-induced movement and creation of magnetic objects

So far it has been shown that one way to modify the magnetic state of the Rh/Co/Ir(111) film consists in applying a magnetic field in the out-of-plane direction: this can lead to the movement of the domain walls and to the magnetic saturation of the Rh/Co areas, depending on the strength of the field, as seen in Fig. 4.4. Additionally, a magnetic field can reduce the size of isolated magnetic objects as done in Fig. 4.12, where a magnetic skyrmion of about 3 nm in diameter has been produced. A different approach consists in using the STM tip to locally modify the film's magnetic configuration: it has been shown that applying large currents or large bias voltages can lead to controlled writing and deleting of magnetic skyrmions in different materials [12, 20]. In this Section a similar procedure is presented, and the response of the magnetic structures in $\mathrm{Rh_{hcp}}$/Co/Ir(111) to tip-induced excitations is investigated. Figure 4.13 shows a sequence of measurements on two $\mathrm{Rh_{hcp}}$/Co/Ir(111) islands: between each two images a large bias voltage has been applied while keeping the tunneling current constant. After having measured the $\mathrm{d}I/\mathrm{d}U$ map of Fig. 4.13(a) at -450 mV, another image of the same area is taken at a bias voltage of +4.5 V and with same tunnelling current (not shown). Then the voltage is brought back to the initial value, and the $\mathrm{d}I/\mathrm{d}U$ map of Fig. 4.13(b) is measured. The position of the do-

main walls, visible as bright stripes thanks to the NCMR effect, has now changed in both islands. After finishing the scan, the tip is brought at the position indicated by the red dotted circle in Fig. 4.13(b), and the bias voltage is slowly swept down to -5.5 V, while keeping the current constant at 1 nA, and then swept back to -450 mV. Figure 4.13(c) shows the effect of such a procedure: the locally applied large bias voltage influences not only the wall in the vicinity of the tip, but also those on the adjacent island, about 10 nm away from the tip position. Applying now +5.5 V at the same location results in the configuration of Fig. 4.13(d): the wall in the top island is back in the exact same position it had in Fig. 4.13(a), and the walls on the bottom island are in a configuration very similar to the one of Fig. 4.13(b). Thus some locations in the islands appear to be energetically more favourable for domain walls, as the walls repeatedly come back to them after being moved by the large bias voltage. This is also visible in the sequence of Figs. 4.13(e) to (h), which displays the same two islands in a scan area that now encompasses them completely: applying both positive and negative large bias voltages at specific locations results in the movement of walls on both islands, and some of the walls' positions are the same in different panels of Fig. 4.13. The origin of these more favourable wall positions is attributed

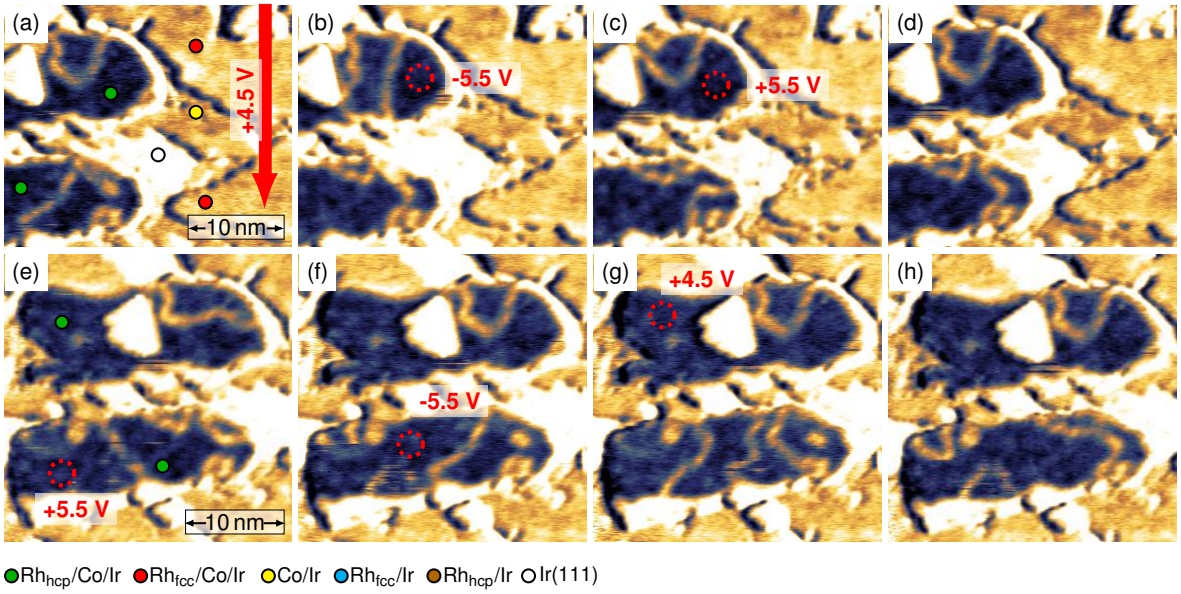

Figure 4.13: Differential conductance maps of two Rh_{hcp}/Co/Ir(111) islands. Maps (e) to (h) display the same islands visible in (a) to (d), with the scan area shifted to the left and with a different initial magnetic configuration. Between (a) and (b) a full scan across the area with +4.5 V is performed. The dotted circles indicate the positions where the tip is located when performing a voltage ramp to the indicated value. The feedback loop is on during the ramps, meaning that the tunnel current is kept at a constant value of 1 nA. Many of the walls can be found in the same positions throughout the sequence of images. *Measurement parameters*: -450 mV, 1 nA, 4 K, Cr bulk tip.

to the inhomogeneity of the film, which can produce local variations of the magnetic parameters, thus resulting in different domain wall energies at different positions. The shape of the magnetic objects in Rh/Co/Ir(111) is therefore strongly influenced by the film's quality and local properties. Whereas large bias voltages at a constant tunnel current allow to move the domain walls in different positions, tunnel currents up to 9 nA at a constant small bias voltage (around -0.5 V) do not produce any effect and leave the magnetic configuration unaltered.
The conditions to induce magnetic structures in a ferromagnetic background have also been investigated. Applying large bias voltages on ferromagnetic areas of Rh/Co in the virgin magnetic state does not yield any result, and neither does applying large currents. However, a magnetic field can be used to bring Rh/Co islands into a ferromagnetic state, which is then perturbed using the STM tip, as shown in Fig. 4.14. Note that the sample area displayed in Figs. 4.14(a) to (d) is part of the area imaged in Fig. 4.4. The Rh_{hcp}/Co/Ir island in (a) indicated by the green ellipse is brought into the ferromagnetic state by applying an out-of-plane magnetic field in (b). Other islands in the scan area are not completely saturated at this magnetic field, as visible

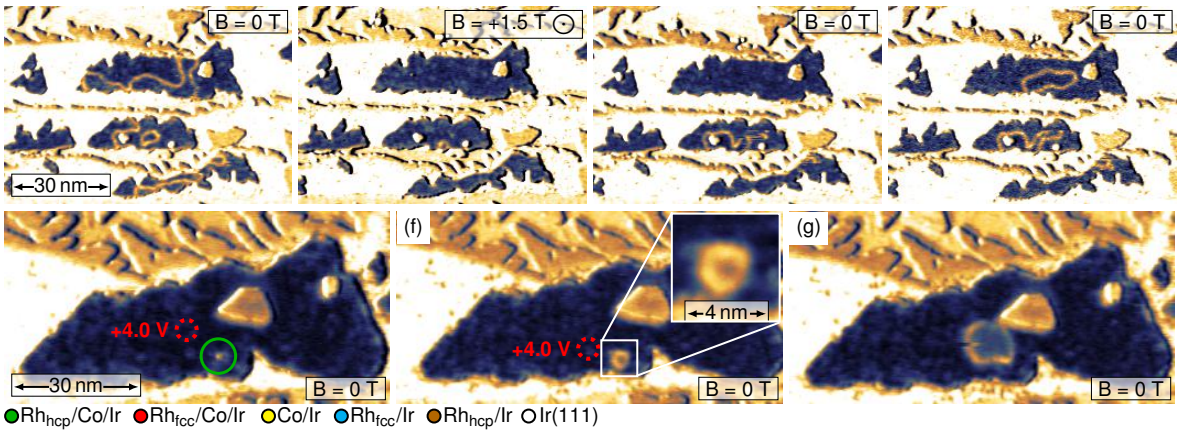

Figure 4.14: (a) to (d): Differential conductance maps of a Rh/Co/Ir(111) sample, demonstrating the tip-induced nucleation of magnetic structures. In zero magnetic field (a) several domain walls are visible in different islands. Upon application of +1.5 T in the out-of-plane direction (b) most of the domain walls vanish, and in particular the large Rh_{hcp}/Co/Ir(111) top island is uniformly magnetized, and remains so also once the magnetic field is switched off (c). Applying +4 V at the position indicated by the red marker results in the creation of a small magnetic domain from the ferromagnetic background (d). (e) to (f): In (e) the Rh_{hcp}/Co/Ir(111) island has previously seen a magnetic field of +1.5 T and is magnetically saturated. Applying a bias voltage of +4 V at the position indicated by the red circle results in a magnetic skyrmion nucleating in the vicinity of an atomic defect (f). The inset offers a closer view on the object. Another voltage ramp in the vicinity of the skyrmion (red marker in (f)) results in a large magnetic object, which appears to be still pinned to the atomic defect. *Measurement parameters*: -250 mV, 1 nA, 4 K, Cr bulk tip.

by the yellow ellipse in (b). The field is then reduced back to zero (see Fig. 4.14(c)), and the island is still ferromagnetic, while some domain walls are present in the neighbouring islands. The tip is then brought in the position indicated by the red dotted circle, and a bias voltage ramp to +4.0 V at constant tunnel current is performed. When scanning again over the same area (see Fig. 4.14(d)), a small domain has nucleated roughly in correspondence to the area where the tip was positioned. The applied bias voltage has induced the nucleation of a domain in a ferromagnetic background.
This procedure has been applied to several different areas of Rh_{hcp}/Co/Ir(111) to nucleate magnetic structures. Similarly to what has been observed for the domain wall movement, the changes in the magnetic configuration do not necessarily happen at the position where the tip is located during the voltage ramp. Figure 4.14(e) shows a ferromagnetic Rh/Co island in zero magnetic field. The island has been previously saturated with an out-of-plane magnetic field of +1.5 T. An atomic defect is highlighted by the green ellipse. A voltage ramp up to +4.0 V is applied about 6 nm away from the defect, and as a result a magnetic skyrmion is nucleated at the edge of the island, possibly pinned to the atomic defect, as the domain wall crosses the defect position (see Fig. 4.14(f)). Another voltage ramp produces an expansion of the skyrmion to a much larger size, as visible in Fig. 4.14(g). Note that also here the domain wall is still crossing the atomic defect. The inset of Fig. 4.14(f) shows a closer view of the magnetic skyrmion, whose diameter can be estimated in the same way as it has been shown in Section 4.2.4, yielding 2.2 nm. In Rh/Co/Ir(111) it is therefore not only possible to observe stable nanometer-wide magnetic skyrmions in zero magnetic field, but such objects can also be nucleated in a ferromagnetic background using the STM tip.
Whereas in other systems the sign of the applied bias voltage, or tunnel current, allows to separately write or delete magnetic skyrmions [12, 20], here applied bias voltages of both signs can result in domain wall movement, while nucleation of magnetic structures from ferromagnetic backgrounds has only been investigated using positive bias voltages. Furthermore, the nucleation procedure has been observed not to work for a few Rh_{hcp}/Co/Ir islands, and it has not been possible to delete previously induced magnetic structures, neither with large bias voltages nor with large tunnelling currents in zero magnetic field. These results indicate that the presented procedure does not allow full control over the manipulation of the magnetic state of Rh_{hcp}/Co/Ir islands. The possible mechanisms responsible for such tip-induced changes are nevertheless examined below.

- Thermal fluctuations might randomly induce a change in the magnetic structure. They can, however, be excluded as responsible mechanism, because the walls and skyrmions considered for the discussion above, as well as the ferromagnetic islands, are stable at the measurement temperature (T = 4.2 K) during successive scans. Therefore random thermal noise cannot be the origin of the

observed domain wall movement and nucleation.

- High tunnel currents or bias voltages can generate local Joule heating of the sample, due to the electrical power injected from the STM tip. Such power is proportional to the product of tunnel current and bias voltage. It has been discussed above that tunnel currents up to 9 nA, with a bias voltage around -0.5 V, do not produce any movement of the walls. In contrast, bias voltages of ± 4 V, with tunnel currents from 0.8 to 1 nA, are sufficient to move the domain walls. In these two cases the injected electrical power is similar, and it cannot therefore be accounted for the observed movement of walls only at high biases. On the other hand, the effect of large tunnelling currents, at moderate bias voltages, for the nucleation of magnetic objects has not been studied. Therefore it cannot be excluded that Joule heating could influence the creation of domains and skyrmions in ferromagnetic islands.
- Electrons tunnelling between tip and sample with a certain energy and spin direction can relax through several elastic or inelastic processes, including electron-phonon and electron-electron interactions. The production of phonons in the sample due to high-energy electrons can result in local heating of the magnetic nanoislands [121], but such case has already been excluded above. Non-thermal excitations, including magnon generation, spin-flip scattering and other electron-electron processes, can contribute significantly to the electron energy and spin relaxation, depending on the energy of the tunnelling electrons [122, 123]. Such scattering processes involving high-energy electrons produced by the large applied bias voltages might be responsible for the nucleation and motion of domain walls. At lower biases these processes could have a smaller contribution to the electron relaxation, explaining why a sufficiently large voltage is necessary to trigger a modification of the magnetic configuration.
- The tunnel current produces an Oersted field, which has been shown to influence magnetic switching processes [124]. The sign of the tunnel current determines the sense of rotation of the field around the flow of current. Such field is, however, proportional to the tunnel current, and not correlated with the applied bias voltage. Such an effect would explain neither the observed movement and nucleation of the walls at large biases nor the absence of any effect when increasing the current. This mechanism therefore cannot be accounted for the tip-induced changes in the magnetic state of the film.
- The tip could induce a local stray field on the sample, for example because of a Co cluster attached at its apex. Additionally, antiferromagnetic Cr tips can also have small stray fields when close enough to the surface ($\approx$ 100 mT at 6 Å [125]). Such field should indeed increase in strength as the tip gets closer to the sample. In the presented experiments, to induce large currents at a fixed bias voltage the tip is brought closer to the surface, and in this case no significant effect on the magnetic structures has been observed. On the contrary,

when the bias voltage is increased, the tip draws farther away from the surface to keep the tunnelling current constant. In such cases the magnetism in the film is significantly modified. Thus, the observed effects do not agree with an explanation based on the tip's stray field, and therefore such mechanism can be neglected as the origin of either domain wall motion or nucleation.

- Electric fields can modify the magnetic properties of a metallic film, for example by changing the interlayer distances and thus the magnetic interactions [126], or because of a redistribution of the charges at the surface of the film, which in turn can modify the occupied electronic bands of the system [127, 128]. The bias voltage applied between tip and sample produces an electric field which, if sufficiently large, can lead to visible changes in the magnetic configuration of the film [20, 128]. The electric field at the sample's surface can be estimated in first approximation (parallel plates approximation) as:

$$E = \frac{U}{d}, \tag{4.9}$$

  where U is the applied bias voltage and d is the tip-sample distance. When keeping the current feedback loop on, the distance $d = d(U)$ is increased as U increases to keep the current at the desired value. Since the tip-sample distance was not recorded during the experiments presented in Figs. 4.13 and 4.14, it is not possible to estimate here the applied electric field as a function of U. It is, however, reasonable to assume that during a bias sweep U changes by a larger amount with respect to d, given the exponential dependence of the tunnel current on the tip-sample distance, and therefore that the electric field increases in magnitude when U increases [2]. This has already been verified for a Cr bulk tip on different samples, namely Fe/W(110) and Fe/Mo(110) [128]. For this reason the generated electric field could be responsible for the observed modifications of the magnetic film at high bias voltages. The electric field at the sample's surface decreases in intensity as one moves farther from the tip position, but if the field is large enough it could still influence magnetic structures located several nanometers away, as seen in the experiments.
- An electric current passing through a magnetic material becomes spin-polarized, with a large fraction of the electrons orienting their spins along the direction induced by the magnetic layer. The electrons in such a spin-polarized current, when injected in another magnetic layer, can interact with the layer's magnetization by transfer of angular momentum, exerting a torque on the magnetization known as spin-transfer-torque (STT). Such an effect has been used in an SP-STM configuration to influence the magnetization switching of nanoislands [124, 130], and is one of the proposed mechanisms responsible for the writing and deleting, depending on the current sign, of magnetic skyrmions in

[2] The increase in E is however not completely monotonic: at bias voltages corresponding to field emission resonances, d decreases very steeply, producing a decrease of E. The exact energy of such resonances depends on the considered system, for Fe/W(110) the first one being around +4.7 V [129]

Pd/Fe/Ir(111) [12, 77]. The injection of spin-polarized electrons is expected to produce variations of the magnetization in correspondence of the tip position, where the electrons tunnel into the sample. In Fig. 4.13 changes in domain wall positions are detected in some cases at 10 nm away from the tip location, even on different Rh/Co islands. For this reason the STT is neglected as possible origin of the tip-induced domain wall motion. On the other hand, its influence on the creation of domain walls from ferromagnetic islands cannot be excluded, as the dependence of the nucleation process on the tunnel current has not been investigated.

To summarize, non-thermal processes involving high-energy electrons and electric fields from the tip apex could both be the cause of the observed tip-induced modifications of the magnetic state in Rh_{hcp}/Co/Ir(111). Additionally, Joule heating and STT might also play a role in the creation of magnetic objects on ferromagnetic islands. To pin down the exact mechanisms behind the observed processes, specific experiments would have to be performed, to investigate the separate roles of current and bias. For example, the role of high tunnel currents in the nucleation of magnetic structures from a ferromagnetic background remains unknown and would need to be studied. Experiments with non-magnetic tips could also help in discriminating between effects due to spin-polarization and those due, for example, to the electric field from the tip, similarly to what has been done in [20]. Nevertheless the presented method allows to nucleate objects with non-trivial topology and diameter below 5 nm from a ferromagnetic background. Objects of such size are of utmost interest in view of practical applications in spintronic devices [14].

4.4 Summary and outlook

In this Chapter it has been shown that a single Rh atomic layer deposited on top of a Co/Ir(111) sample favours the presence of different non-collinear structures. This system has a ferromagnetic ground state, and magnetic skyrmions with diameter below 5 nm are found to be stable in zero magnetic field. Such structures are easily detectable thanks to their large NCMR contrast, and thus their properties could be investigated also by means of standard (non-spin-polarized) STM. This is the first Co-based ultrathin film for which an NCMR effect has been observed, and the large modifications at the Fermi energy can be exploited to detect non-collinear objects using transport measurements. Additionally, it has been shown that the magnetic state of the film can be modified by means of large bias voltages, offering the possibility to manipulate skyrmions and domain walls, and to induce them from a ferromagnetic background. The non-optimal Rh/Co interface quality, possibly due to intermixing, suggests that similar results could be obtained in sputter-deposited films, where the interfaces are generally not as ordered as in epitaxially-grown films.

Future studies regarding this system should certainly aim at clarifying the role of intermixing and surface roughness on the film's magnetic state and on its pinning

properties, as it has been shown (see Section 4.3, for example) that the surface morphology plays a decisive role in determining the shape and the position of most non-collinear structures. Highly relevant in view of technological applications would also be to study the temperature dependence of the magnetic state of films composed of Rh deposited on Co/Ir. In particular, as it has been shown that the bare double layer Co on Ir(111) is still magnetic at 300 K (see Section 3.5.2), it would be interesting to see if a Rh/Co/Co/Ir(111) could still display nanometer-sized magnetic skyrmions at room temperature.

Chapter 5

Summary and outlook

In this thesis two types of non-collinear magnetic structures in Co-based ultrathin films have been studied, namely domain walls and skyrmions. These objects arise as a consequence of the competition of different magnetic interactions, whose relative strength can be tuned by different substrates, different Co thickness and different top layers. In Co/Ir(111) and Co/Pt(111) domain walls are mostly found in constrictions of the magnetic film, separating out-of-plane ferromagnetic domains whose size and shape is influenced by the local surface morphology. As the Co thickness increases, such influence becomes negligible and the domains become larger. Also the domain walls become wider in thicker Co layers, as a consequence of either an increase or a decrease of both exchange stiffness A and effective anisotropy K. The interfacial DMI plays a key role in stabilizing non-collinear spin structures in these films, as confirmed by the observation of unique sense of magnetization rotation for the domain walls in both Co/Ir(111) and Co/Pt(111). A clockwise rotational sense for walls in Co/Ir(111) was deduced from the domain wall tilting in in-plane magnetic fields. A Pt layer on top of Co/Ir modifies the film's magnetic parameters, resulting in an increased domain wall energy. This was concluded from the observation of the majority of the walls being located on the uncovered Co/Ir(111) areas, rather than on the trilayer system. DFT calculations have shown that the DMI in Pt/Co/Ir(111) is due mostly to the Pt/Co interface, with a negligible contribution from the Co/Ir interface, suggesting that the picture of additive DMI does not hold in the limit of one Co atomic layer. Finally, the double layer of Co/Ir(111) has been observed to be still magnetic at room temperature.

By replacing Pt with Rh as a top layer, a significant change in the film's properties has been observed. Not only are domain walls found more often in Rh/Co/Ir than in uncovered Co/Ir, but the trilayer structure also hosts small isolated domains and skyrmions in the virgin magnetic state. The size and the shape of such objects appear to be strongly influenced by the local inhomogeneity of the film, presumably due to a certain degree of intermixing between Rh and Co. The local magnetic non-collinearity produces modifications in the sample's density of states at various energies. These variations induce changes in the measured $\mathrm{d}I/\mathrm{d}U$ signal as large

as 40%, allowing to easily detect the magnetic objects using conventional STM. A simple model, based on previous studies of this effect and on DFT calculations, has been developed to take into account the NCMR contribution to the $\mathrm{d}I/\mathrm{d}U$ signal when fitting domain wall profiles. Such model can be used to estimate the diameter of the magnetic skyrmions, which is found to be on the order of 3 nm. Due to such a remarkably small skyrmion size, and to the stability of these objects in zero field in a ferromagnetic ground state, it can be concluded that the Rh/Co/Ir(111) system is of strong interest in view of practical applications. Even more since it has been shown that domain walls and skyrmions can be created and moved in such films using an STM tip. The NCMR signal, never observed before for a Co-based ultrathin film, and the ease of nucleation could be exploited in devices for skyrmion detection and manipulation, respectively.

Future experiments should go in the direction of room temperature stability of the observed magnetic structures, which is a key requirement for technological applicability. Although a single atomic layer of Co might have a Curie temperature below 300 K, two Co layers, capped with Rh, on Ir(111) might still present promising non-collinear magnetic configurations up to room temperature.
This work gathers some knowledge on the magnetic properties of Co-based epitaxial ultrathin films, using a microscopy technique which allows to resolve the details of the spin arrangement down to the sub-nm scale. Hopefully, this might provide a useful reference for comparison with results obtained on sputter-deposited Co films using different imaging techniques.

Bibliography

[1] D. Reinsel, J. Gantz, and J. Rydning. *Data Age 2025: The Evolution of Data to Life-Critical*. 2017 (cit. on p. 3).

[2] M. Re. *Heat Assisted Magnetic Recording: the Next Leap Forward is Now*. 2018 (cit. on p. 3).

[3] H. Richter. The transition from longitudinal to perpendicular recording. In: *Journal of Physics D: Applied Physics* 40.9 (2007), R149 (cit. on p. 3).

[4] S. S. P. Parkin, M. Hayashi, and L. Thomas. Magnetic Domain-Wall Racetrack Memory. In: *Science* 320.5873 (2008), pp. 190–194 (cit. on pp. 3, 67).

[5] S. Mittal. A survey of techniques for architecting processor components using domain-wall memory. In: *ACM Journal on Emerging Technologies in Computing Systems (JETC)* 13.2 (2017), p. 29 (cit. on p. 3).

[6] A. N. Bogdanov and D. Yablonskii. Thermodynamically stable "vortices" in magnetically ordered crystals. The mixed state of magnets. In: *Journal of Theoretical and Experimental Phyisics* 95.1 (1989), p. 178 (cit. on pp. 4, 11, 14).

[7] S. Mühlbauer, B. Binz, F. Jonietz, C. Pfleiderer, A. Rosch, A. Neubauer, R. Georgii, and P. Böni. Skyrmion lattice in a chiral magnet. In: *Science* 323.5916 (2009), pp. 915–919 (cit. on pp. 4, 15).

[8] N. Nagaosa and Y. Tokura. Topological properties and dynamics of magnetic skyrmions. In: *Nature Nanotechnology* 8.12 (2013), p. 899 (cit. on pp. 4, 14, 15).

[9] X. Yu, Y. Onose, N. Kanazawa, J. Park, J. Han, Y. Matsui, N. Nagaosa, and Y. Tokura. Real-space observation of a two-dimensional skyrmion crystal. In: *Nature* 465.7300 (2010), p. 901 (cit. on p. 4).

[10] X. Yu, N. Kanazawa, Y. Onose, K. Kimoto, W. Zhang, S. Ishiwata, Y. Matsui, and Y. Tokura. Near room-temperature formation of a skyrmion crystal in thin-films of the helimagnet FeGe. In: *Nature Materials* 10.2 (2011), p. 106 (cit. on pp. 4, 15).

[11] S. Heinze, K. von Bergmann, M. Menzel, J. Brede, A. Kubetzka, R. Wiesendanger, G. Bihlmayer, and S. Blügel. Spontaneous atomic-scale magnetic skyrmion lattice in two dimensions. In: *Nature Physics* 7.9 (2011), p. 713 (cit. on pp. 4, 63).

[12] N. Romming, C. Hanneken, M. Menzel, J. E. Bickel, B. Wolter, K. von Bergmann, A. Kubetzka, and R. Wiesendanger. Writing and deleting single magnetic skyrmions. In: *Science* 341.6146 (2013), pp. 636–639 (cit. on pp. 4, 15, 69, 90, 93, 96).

[13] W. Legrand, D. Maccariello, N. Reyren, K. Garcia, C. Moutafis, C. Moreau-Luchaire, S. Collin, K. Bouzehouane, V. Cros, and A. Fert. Room-temperature current-induced generation and motion of sub-100 nm skyrmions. In: *Nano Letters* 17.4 (2017), pp. 2703–2712 (cit. on p. 4).

[14] A. Fert, N. Reyren, and V. Cros. Magnetic skyrmions: advances in physics and potential applications. In: *Nature Reviews Materials* 2.7 (2017), p. 17031 (cit. on pp. 4, 96).

[15] J. Sampaio, V. Cros, S. Rohart, A. Thiaville, and A. Fert. Nucleation, stability and current-induced motion of isolated magnetic skyrmions in nanostructures. In: *Nature Nanotechnology* 8.11 (2013), p. 839 (cit. on p. 4).

[16] W. Jiang, P. Upadhyaya, W. Zhang, G. Yu, M. B. Jungfleisch, F. Y. Fradin, J. E. Pearson, Y. Tserkovnyak, K. L. Wang, O. Heinonen, et al. Blowing magnetic skyrmion bubbles. In: *Science* 349.6245 (2015), pp. 283–286 (cit. on pp. 4, 15, 63).

[17] C. Hanneken, F. Otte, A. Kubetzka, B. Dupé, N. Romming, K. von Bergmann, R. Wiesendanger, and S. Heinze. Electrical detection of magnetic skyrmions by tunnelling non-collinear magnetoresistance. en. In: *Nature Nanotechnology* 10.12 (2015), pp. 1039–1042 (cit. on pp. 4, 21, 26, 84).

[18] K. Hamamoto, M. Ezawa, and N. Nagaosa. Purely electrical detection of a skyrmion in constricted geometry. In: *Applied Physics Letters* 108.11 (2016), p. 112401 (cit. on p. 4).

[19] O. Heinonen, W. Jiang, H. Somaily, S. G. Te Velthuis, and A. Hoffmann. Generation of magnetic skyrmion bubbles by inhomogeneous spin Hall currents. In: *Physical Review B* 93.9 (2016), p. 094407 (cit. on p. 4).

[20] P.-J. Hsu, A. Kubetzka, A. Finco, N. Romming, K. von Bergmann, and R. Wiesendanger. Electric-field-driven switching of individual magnetic skyrmions. In: *Nature Nanotechnology* 12.2 (2017), p. 123 (cit. on pp. 4, 15, 90, 93, 95, 96).

[21] D. Maccariello, W. Legrand, N. Reyren, K. Garcia, K. Bouzehouane, S. Collin, V. Cros, and A. Fert. Electrical detection of single magnetic skyrmions in metallic multilayers at room temperature. In: *Nature Nanotechnology* 13.3 (2018), p. 233 (cit. on p. 4).

[22] K. Zeissler, S. Finizio, K. Shahbazi, J. Massey, F. Al Ma'Mari, D. M. Bracher, A. Kleibert, M. C. Rosamond, E. H. Linfield, T. A. Moore, et al. Discrete Hall resistivity contribution from Néel skyrmions in multilayer nanodiscs. In: *Nature Nanotechnology* (2018), p. 1 (cit. on p. 4).

[23] F. Jonietz, S. Mühlbauer, C. Pfleiderer, A. Neubauer, W. Münzer, A. Bauer, T. Adams, R. Georgii, P. Böni, R. A. Duine, et al. Spin transfer torques in MnSi at ultralow current densities. In: *Science* 330.6011 (2010), pp. 1648–1651 (cit. on p. 4).

[24] X. Yu, N. Kanazawa, W. Zhang, T. Nagai, T. Hara, K. Kimoto, Y. Matsui, Y. Onose, and Y. Tokura. Skyrmion flow near room temperature in an ultralow current density. In: *Nature Communications* 3 (2012), p. 988 (cit. on p. 4).

[25] S. Woo, K. Litzius, B. Krüger, M.-Y. Im, L. Caretta, K. Richter, M. Mann, A. Krone, R. M. Reeve, M. Weigand, et al. Observation of room-temperature magnetic skyrmions and their current-driven dynamics in ultrathin metallic ferromagnets. In: *Nature Materials* 15.5 (2016), p. 501 (cit. on pp. 4, 15, 63).

[26] A. Fert, V. Cros, and J. Sampaio. Skyrmions on the track. In: *Nature Nanotechnology* 8.3 (2013), p. 152 (cit. on p. 4).

[27] X. Zhang, M. Ezawa, and Y. Zhou. Magnetic skyrmion logic gates: conversion, duplication and merging of skyrmions. In: *Scientific Rreports* 5 (2015), p. 9400 (cit. on p. 4).

[28] D. Prychynenko, M. Sitte, K. Litzius, B. Krüger, G. Bourianoff, M. Kläui, J. Sinova, and K. Everschor-Sitte. Magnetic skyrmion as a nonlinear resistive element: A potential building block for reservoir computing. In: *Physical Review Applied* 9.1 (2018), p. 014034 (cit. on p. 4).

[29] D. Pinna, F. A. Araujo, J.-V. Kim, V. Cros, D. Querlioz, P. Bessiere, J. Droulez, and J. Grollier. Skyrmion gas manipulation for probabilistic computing. In: *Physical Review Applied* 9.6 (2018), p. 064018 (cit. on p. 4).

[30] C. Moreau-Luchaire, C. Moutafis, N. Reyren, J. Sampaio, C. A. F. Vaz, N. Van Horne, K. Bouzehouane, K. Garcia, C. Deranlot, P. Warnicke, P. Wohlhüter, J.-M. George, M. Weigand, J. Raabe, V. Cros, and A. Fert. Additive interfacial chiral interaction in multilayers for stabilization of small individual skyrmions at room temperature. In: *Nature Nanotechnology* 11.5 (2016), pp. 444–448 (cit. on pp. 4, 31, 58, 62, 63).

[31] O. Boulle, J. Vogel, H. Yang, S. Pizzini, D. de Souza Chaves, A. Locatelli, T. O. Menteş, A. Sala, L. D. Buda-Prejbeanu, O. Klein, et al. Room-temperature chiral magnetic skyrmions in ultrathin magnetic nanostructures. In: *Nature Nanotechnology* 11.5 (2016), p. 449 (cit. on pp. 4, 63).

[32] A. Soumyanarayanan, M. Raju, A. G. Oyarce, A. K. Tan, M.-Y. Im, A. P. Petrović, P. Ho, K. Khoo, M. Tran, C. Gan, et al. Tunable room-temperature magnetic skyrmions in Ir/Fe/Co/Pt multilayers. In: *Nature Materials* 16.9 (2017), p. 898 (cit. on pp. 4, 63).

[33] I. Dzyaloshinsky. A thermodynamic theory of "weak" ferromagnetism of antiferromagnetics. In: *Journal of Physics and Chemistry of Solids* 4.4 (1958), pp. 241–255 (cit. on pp. 4, 9).

[34] T. Moriya. Anisotropic superexchange interaction and weak ferromagnetism. In: *Physical Review* 120.1 (1960), p. 91 (cit. on pp. 4, 9, 10).

[35] J. Hagemeister, D. Iaia, E. Y. Vedmedenko, K. von Bergmann, A. Kubetzka, and R. Wiesendanger. Skyrmions at the edge: Confinement effects in Fe/Ir (111). In: *Physical Review Letters* 117.20 (2016), p. 207202 (cit. on p. 4).

[36] S. Blundell. *Magnetism in Condensed Matter*. Oxford University Press, 2001 (cit. on pp. 8, 9).

[37] T. Okubo, S. Chung, and H. Kawamura. Multiple-q states and the skyrmion lattice of the triangular-lattice Heisenberg antiferromagnet under magnetic fields. In: *Physical Review Letters* 108.1 (2012), p. 017206 (cit. on pp. 8, 15).

[38] A. Leonov and M. Mostovoy. Multiply periodic states and isolated skyrmions in an anisotropic frustrated magnet. In: *Nature Communications* 6 (2015), p. 8275 (cit. on pp. 8, 12, 15).

[39] L. Rózsa, K. Palotás, A. Deák, E. Simon, R. Yanes, L. Udvardi, L. Szunyogh, and U. Nowak. Formation and stability of metastable skyrmionic spin structures with various topologies in an ultrathin film. In: *Physical Review B* 95.9 (2017), p. 094423 (cit. on pp. 8, 12, 15).

[40] M. A. Ruderman and C. Kittel. Indirect exchange coupling of nuclear magnetic moments by conduction electrons. In: *Physical Review* 96.1 (1954), p. 99 (cit. on p. 8).

[41] T. Kasuya. A theory of metallic ferro-and antiferromagnetism on Zener's model. In: *Progress of Theoretical Physics* 16.1 (1956), pp. 45–57 (cit. on p. 8).

[42] K. Yosida. Magnetic properties of Cu-Mn alloys. In: *Physical Review* 106.5 (1957), p. 893 (cit. on p. 8).

[43] A. Fert and P. M. Levy. Role of anisotropic exchange interactions in determining the properties of spin-glasses. In: *Physical Review Letters* 44.23 (1980), p. 1538 (cit. on p. 10).

[44] A. Fert. "Magnetic and transport properties of metallic multilayers". In: *Materials Science Forum*. Vol. 59. Trans Tech Publ. 1990, pp. 439–480 (cit. on p. 10).

[45] A. Bogdanov and A. Hubert. Thermodynamically stable magnetic vortex states in magnetic crystals. In: *Journal of Magnetism and Magnetic Materials* 138.3 (1994), pp. 255–269 (cit. on pp. 10, 11, 14).

[46] A. Hubert and R. Schäfer. *Magnetic domains: the analysis of magnetic microstructures*. Springer Science & Business Media, 2008 (cit. on pp. 10, 11).

[47] M. Heide, G. Bihlmayer, and S. Blügel. Dzyaloshinskii-Moriya interaction accounting for the orientation of magnetic domains in ultrathin films: Fe/W (110). In: *Physical Review B* 78.14 (2008), p. 140403 (cit. on pp. 12, 13, 49, 61, 62).

[48] A. Thiaville, S. Rohart, É. Jué, V. Cros, and A. Fert. Dynamics of Dzyaloshinskii domain walls in ultrathin magnetic films. In: *Europhysics Letters* 100.5 (2012), p. 57002 (cit. on pp. 12, 13, 49).

[49] A. Kubetzka, O. Pietzsch, M. Bode, and R. Wiesendanger. Spin-polarized scanning tunneling microscopy study of 360° walls in an external magnetic field. In: *Physical Review B* 67.2 (2003), p. 020401 (cit. on pp. 13, 86, 89).

[50] N. Romming, A. Kubetzka, C. Hanneken, K. von Bergmann, and R. Wiesendanger. Field-dependent size and shape of single magnetic skyrmions. In: *Physical Review Letters* 114.17 (2015), p. 177203 (cit. on pp. 14, 89, 90).

[51] T. H. R. Skyrme. A unified field theory of mesons and baryons. In: *Nuclear Physics* 31 (1962), pp. 556–569 (cit. on p. 14).

[52] A. Leonov, T. Monchesky, N. Romming, A. Kubetzka, A. Bogdanov, and R. Wiesendanger. The properties of isolated chiral skyrmions in thin magnetic films. In: *New Journal of Physics* 18.6 (2016), p. 065003 (cit. on p. 15).

[53] S. Takao. A study of magnetization distribution of submicron bubbles in sputtered Ho-Co thin films. In: *Journal of Magnetism and Magnetic Materials* 31 (1983), pp. 1009–1010 (cit. on p. 15).

[54] A. Malozemoff and J. Slonczewski. *Magnetic Domain Walls in Bubble Materials: Advances in Materials and Device Research*. Vol. 1. Academic press, 2016 (cit. on p. 15).

[55] N. Kiselev, A. Bogdanov, R. Schäfer, and U. Rößler. Chiral skyrmions in thin magnetic films: new objects for magnetic storage technologies? In: *Journal of Physics D: Applied Physics* 44.39 (2011), p. 392001 (cit. on p. 15).

[56] K. Y. Guslienko. Skyrmion state stability in magnetic nanodots with perpendicular anisotropy. In: *IEEE Magnetics Letters* 6 (2015), pp. 1–4 (cit. on p. 15).

[57] F. Büttner, I. Lemesh, and G. S. Beach. Theory of isolated magnetic skyrmions: From fundamentals to room temperature applications. In: *Scientific Reports* 8.1 (2018), p. 4464 (cit. on p. 15).

[58] M. Schott, A. Bernand-Mantel, L. Ranno, S. Pizzini, J. Vogel, H. Béa, C. Baraduc, S. Auffret, G. Gaudin, and D. Givord. The skyrmion switch: turning magnetic skyrmion bubbles on and off with an electric field. In: *Nano Letters* 17.5 (2017), pp. 3006–3012 (cit. on p. 15).

[59] W. Jiang, X. Zhang, G. Yu, W. Zhang, X. Wang, M. B. Jungfleisch, J. E. Pearson, X. Cheng, O. Heinonen, K. L. Wang, et al. Direct observation of the skyrmion Hall effect. In: *Nature Physics* 13.2 (2017), p. 162 (cit. on p. 15).

[60] G. Binnig, H. Rohrer, C. Gerber, and E. Weibel. Surface studies by scanning tunneling microscopy. In: *Physical Review Letters* 49.1 (1982), p. 57 (cit. on p. 16).

[61] J. Bardeen. Tunnelling from a many-particle point of view. In: *Physical Review Letters* 6.2 (1961), p. 57 (cit. on p. 16).

[62] J. Tersoff and D. Hamann. Theory and application for the scanning tunneling microscope. In: *Physical Review Letters* 50.25 (1983), p. 1998 (cit. on p. 17).

[63] A. Kubetzka. "Spinpolarisierte Rastertunnelmikroskopie an magnetischen Nanostrukturen: Fe/W(110)". PhD thesis. Universität Hamburg, 2002 (cit. on pp. 17, 21, 24).

[64] C. J. Chen. Origin of atomic resolution on metal surfaces in scanning tunneling microscopy. In: *Physical Review Letters* 65.4 (1990), p. 448 (cit. on p. 18).

[65] C. J. Chen. *Introduction to scanning tunneling microscopy*. Vol. 4. Oxford University Press on Demand, 1993 (cit. on p. 18).

[66] M. Julliere. Tunneling between ferromagnetic films. In: *Physics letters A* 54.3 (1975), pp. 225–226 (cit. on p. 18).

[67] J. C. Slonczewski. Conductance and exchange coupling of two ferromagnets separated by a tunneling barrier. In: *Physical Review B* 39.10 (1989), p. 6995 (cit. on p. 20).

[68] M. Bode. Spin-polarized scanning tunnelling microscopy. In: *Reports on Progress in Physics* 66.4 (2003), p. 523 (cit. on p. 20).

[69] R. Wiesendanger. Spin mapping at the nanoscale and atomic scale. In: *Reviews of Modern Physics* 81.4 (2009), p. 1495 (cit. on pp. 20, 30).

[70] D. Wortmann, S. Heinze, P. Kurz, G. Bihlmayer, and S. Blügel. Resolving complex atomic-scale spin structures by spin-polarized scanning tunneling microscopy. In: *Physical Review Letters* 86.18 (2001), p. 4132 (cit. on p. 20).

[71] M. Bode, S. Heinze, A. Kubetzka, O. Pietzsch, X. Nie, G. Bihlmayer, S. Blügel, and R. Wiesendanger. Magnetization-Direction-Dependent Local Electronic Structure Probed by Scanning Tunneling Spectroscopy. In: *Physical Review Letters* 89.23 (2002), p. 237205 (cit. on pp. 21, 82).

[72] K. von Bergmann, M. Menzel, D. Serrate, Y. Yoshida, S. Schröder, P. Ferriani, A. Kubetzka, R. Wiesendanger, and S. Heinze. Tunneling anisotropic magnetoresistance on the atomic scale. In: *Physical Review B* 86.13 (2012), p. 134422 (cit. on pp. 21, 24).

[73] A. Kubetzka, C. Hanneken, R. Wiesendanger, and K. von Bergmann. Impact of the skyrmion spin texture on magnetoresistance. In: *Physical Review B* 95.10 (2017), p. 104433 (cit. on pp. 21, 24, 82, 84).

[74] C. Hanneken. "Observation of Non-Collinear Magnetoresistance by Scanning Tunneling Spectroscopy on Skyrmions in PdFe/Ir(111)". PhD thesis. Universität Hamburg, 2015 (cit. on pp. 21, 24, 84).

[75] D. M. Crum, M. Bouhassoune, J. Bouaziz, B. Schweflinghaus, S. Blügel, and S. Lounis. Perpendicular reading of single confined magnetic skyrmions. In: *Nature Communications* 6 (2015), p. 8541 (cit. on p. 21).

[76] N. Romming, H. Pralow, A. Kubetzka, M. Hoffmann, S. von Malottki, S. Meyer, B. Dupé, R. Wiesendanger, K. von Bergmann, and S. Heinze. Competition of Dzyaloshinskii-Moriya and higher-order exchange interactions in Rh/Fe atomic bilayers on Ir (111). In: *Physical review letters* 120.20 (2018), p. 207201 (cit. on pp. 21, 69).

[77] N. Romming. "Discovery and Manipulation of Individual Skyrmions in Ultrathin Magnetic Films". PhD thesis. Universität Hamburg, 2017 (cit. on pp. 24, 96).

[78] S. Heinze. Simulation of spin-polarized scanning tunneling microscopy images of nanoscale non-collinear magnetic structures. In: *Applied Physics A* 85.4 (2006), pp. 407–414 (cit. on p. 24).

[79] F. Himpsel, J. Ortega, G. Mankey, and R. Willis. Magnetic nanostructures. In: *Advances in Physics* 47.4 (1998), pp. 511–597 (cit. on pp. 28, 36).

[80] O. Pietzsch, A. Kubetzka, D. Haude, M. Bode, and R. Wiesendanger. A low-temperature ultrahigh vacuum scanning tunneling microscope with a split-coil magnet and a rotary motion stepper motor for high spatial resolution studies of surface magnetism. In: *Review of Scientific Instruments* 71.2 (2000), pp. 424–430 (cit. on p. 29).

[81] S. Meckler, M. Gyamfi, O. Pietzsch, and R. Wiesendanger. A low-temperature spin-polarized scanning tunneling microscope operating in a fully rotatable magnetic field. In: *Review of Scientific Instruments* 80.2 (2009), p. 023708 (cit. on p. 29).

[82] R. Wiesendanger. *Scanning probe microscopy and spectroscopy: methods and applications*. Cambridge university press, 1994 (cit. on p. 30).

[83] J. F. Pulecio, A. Hrabec, K. Zeissler, R. M. White, Y. Zhu, and C. H. Marrows. Hedgehog Skyrmion Bubbles in Ultrathin Films with Interfacial Dzyaloshinskii-Moriya Interactions. In: *ArXiv e-prints* (2016) (cit. on p. 31).

[84] M. Perini, S. Meyer, B. Dupé, S. von Malottki, A. Kubetzka, K. von Bergmann, R. Wiesendanger, and S. Heinze. Domain walls and Dzyaloshinskii-Moriya interaction in epitaxial Co/Ir (111) and Pt/Co/Ir (111). In: *Physical Review B* 97.18 (2018), p. 184425 (cit. on pp. 31, 42, 47, 50, 55–57, 59, 61, 62).

[85] A. Finco, M. Perini, A. Kubetzka, K. von Bergmann, and R. Wiesendanger. Magnetic domain walls in strain-patterned ultrathin films. In: *Physical Review B* 98 (17 2018), p. 174435 (cit. on pp. 31, 36, 48, 52–54, 56).

[86] J. E. Bickel, F. Meier, J. Brede, A. Kubetzka, K. von Bergmann, and R. Wiesendanger. Magnetic properties of monolayer Co islands on Ir(111) probed by spin-resolved scanning tunneling microscopy. In: *Physical Review B* 84.5 (2011), p. 054454 (cit. on pp. 31, 32, 41, 81).

[87] E. Lundgren, B. Stanka, M. Schmid, and P. Varga. Thin films of Co on Pt(111): Strain relaxation and growth. In: *Physical Review B* 62.4 (2000), pp. 2843–2851 (cit. on pp. 33, 34).

[88] E. Lundgren, G. Leonardelli, M. Schmid, and P. Varga. A misfit structure in the Co/Pt (111) system studied by scanning tunnelling microscopy and embedded atom method calculations. In: *Surface Science* 498.3 (2002), pp. 257–265 (cit. on pp. 33, 34, 37).

[89] F. Meier, K. von Bergmann, P. Ferriani, J. Wiebe, M. Bode, K. Hashimoto, S. Heinze, and R. Wiesendanger. Spin-dependent electronic and magnetic properties of Co nanostructures on Pt(111) studied by spin-resolved scanning tunneling spectroscopy. In: *Physical Review B* 74.19 (2006), p. 195411 (cit. on pp. 33, 34, 44).

[90] F. Meier, K. von Bergmann, J. Wiebe, M. Bode, and R. Wiesendanger. Co double-layer nanostructures on Pt (111) studied by spin-polarized scanning tunnelling microscopy. In: *Journal of Physics D: Applied Physics* 40.5 (2007), p. 1306 (cit. on pp. 33, 34, 37, 44).

[91] D. Iaia, A. Kubetzka, K. von Bergmann, and R. Wiesendanger. Structural and magnetic properties of Ni/Fe nanostructures on Ir(111). In: *Physical Review B* 93.13 (2016), p. 134409 (cit. on p. 34).

[92] M. Bott, T. Michely, and G. Comsa. The homoepitaxial growth of Pt on Pt (111) studied with STM. In: *Surface Science* 272.1-3 (1992), pp. 161–166 (cit. on p. 36).

[93] C.-S. Shern, J.-S. Tsay, H. Her, Y. Wu, and R. Chen. Response and enhancement of surface magneto-optic Kerr effect for Co–Pt (111) ultrathin films and surface alloy. In: *Surface Science* 429.1-3 (1999), pp. L497–L502 (cit. on p. 45).

[94] J.-W. Lee, J.-R. Jeong, S.-C. Shin, J. Kim, and S.-K. Kim. Spin-reorientation transitions in ultrathin Co films on Pt (111) and Pd (111) single-crystal substrates. In: *Physical Review B* 66.17 (2002), p. 172409 (cit. on p. 45).

[95] C. Quirós, S. Valvidares, O. Robach, and S. Ferrer. Low-temperature growth favours hcp structure, flatness and perpendicular magnetic anisotropy of thin (1–5 nm) Co films on Pt (111). In: *Journal of Physics: Condensed Matter* 17.36 (2005), p. 5551 (cit. on p. 45).

[96] E. C. Corredor, S. Kuhrau, F. Kloodt-Twesten, R. Frömter, and H. P. Oepen. SEMPA investigation of the Dzyaloshinskii-Moriya interaction in the single, ideally grown Co/Pt (111) interface. In: *Physical Review B* 96.6 (2017), p. 060410 (cit. on p. 45).

[97] P. Bruno. Geometrically Constrained Magnetic Wall. en. In: *Physical Review Letters* 83.12 (1999), pp. 2425–2428 (cit. on pp. 48, 53, 60).

[98] S. Rusponi, T. Cren, N. Weiss, M. Epple, P. Buluschek, L. Claude, and H. Brune. The remarkable difference between surface and step atoms in the magnetic anisotropy of two-dimensional nanostructures. In: *Nature Materials* 2.8 (2003), p. 546 (cit. on pp. 48, 53).

[99] S. Meckler, N. Mikuszeit, A. Preßler, E. Vedmedenko, O. Pietzsch, and R. Wiesendanger. Real-space observation of a right-rotating inhomogeneous cycloidal spin spiral by spin-polarized scanning tunneling microscopy in a triple axes vector magnet. In: *Physical Review Letters* 103.15 (2009), p. 157201 (cit. on p. 55).

[100] L. Schmidt. "Magnetic skyrmions and spin spirals in ultrathin films and canted magnetic fields". PhD thesis. Universität Hamburg, 2017 (cit. on p. 55).

[101] O. Boulle, S. Rohart, L. D. Buda-Prejbeanu, E. Jué, I. M. Miron, S. Pizzini, J. Vogel, G. Gaudin, and A. Thiaville. Domain Wall Tilting in the Presence of the Dzyaloshinskii-Moriya Interaction in Out-of-Plane Magnetized Magnetic Nanotracks. In: *Physical Review Letters* 111.21 (2013), p. 217203 (cit. on p. 55).

[102] L. Landau and E. Lifshitz. On the theory of the dispersion of magnetic permeability in ferromagnetic bodies. In: *Physicalische Zeitschrift der Sowjetunion* 8.153 (1935), pp. 101–114 (cit. on p. 55).

[103] T. L. Gilbert. A phenomenological theory of damping in ferromagnetic materials. In: *IEEE Transactions on Magnetics* 40.6 (2004), pp. 3443–3449 (cit. on p. 55).

[104] J. Mentink, M. Tretyakov, A. Fasolino, M. Katsnelson, and T. Rasing. Stable and fast semi-implicit integration of the stochastic Landau–Lifshitz equation. In: *Journal of Physics: Condensed Matter* 22.17 (2010), p. 176001 (cit. on p. 55).

[105] H. Yang, A. Thiaville, S. Rohart, A. Fert, and M. Chshiev. Anatomy of Dzyaloshinskii-Moriya Interaction at Co/Pt Interfaces. In: *Physics Review Letters* 115.26 (2015), p. 267210 (cit. on p. 58).

[106] G. Chen, A. Mascaraque, A. T. N'Diaye, and A. K. Schmid. Room temperature skyrmion ground state stabilized through interlayer exchange coupling. In: *Applied Physics Letters* 106.24 (2015), p. 242404 (cit. on p. 63).

[107] C. Schneider, P. Bressler, P. Schuster, J. Kirschner, J. De Miguel, and R. Miranda. Curie temperature of ultrathin films of fcc-cobalt epitaxially grown on atomically flat Cu(100) surfaces. In: *Physical Review Letters* 64.9 (1990), p. 1059 (cit. on p. 63).

[108] P. Jensen, H. Dreyssé, and K. Bennemann. Calculation of the film-thickness-dependence of the Curie temperature in thin transition metal films. In: *Europhysics Letters* 18.5 (1992), p. 463 (cit. on p. 63).

[109] F. Huang, M. T. Kief, G. J. Mankey, and R. F. Willis. Magnetism in the few-monolayers limit: A surface magneto-optic Kerr-effect study of the magnetic behavior of ultrathin films of Co, Ni, and Co-Ni alloys on Cu(100) and Cu(111). In: *Physical Review B* 49 (6 1994), pp. 3962–3971 (cit. on p. 63).

[110] H. Elmers, J. Hauschild, H. Fritzsche, G. Liu, U. Gradmann, and U. Köhler. Magnetic frustration in ultrathin Fe films. In: *Physical Review Letters* 75.10 (1995), p. 2031 (cit. on p. 63).

[111] A. Sonntag, J. Hermenau, S. Krause, and R. Wiesendanger. Thermal stability of an interface-stabilized skyrmion lattice. In: *Physical Review Letters* 113.7 (2014), p. 077202 (cit. on p. 63).

[112] A. Finco, L. Rózsa, P.-J. Hsu, A. Kubetzka, E. Vedmedenko, K. von Bergmann, and R. Wiesendanger. Temperature-induced increase of spin spiral periods. In: *Physical Review Letters* 119.3 (2017), p. 037202 (cit. on p. 63).

[113] V. Jähnke, J. Güdde, and E. Matthias. Growth and magnetic ordering of Ni and Co films on Rh(001) investigated with second-harmonic generation. In: *Journal of Magnetism and Magnetic Materials* 232.1-2 (2001), pp. 27–35 (cit. on p. 63).

[114] G. Garreau, M. Farle, E. Beaurepaire, and K. Baberschke. Curie temperature and morphology in ultrathin Co/W(110) films. In: *Physical Review B* 55 (1 1997), pp. 330–335 (cit. on p. 63).

[115] R. Varga, A. Zhukov, J. M. Blanco, M. Ipatov, V. Zhukova, J. Gonzalez, and P. Vojtanik. Fast magnetic domain wall in magnetic microwires. In: *Physical Review B* 74 (21 2006), p. 212405 (cit. on p. 66).

[116] J. Sassmannshausen, A. Kubetzka, P.-J. Hsu, K. von Bergmann, and R. Wiesendanger. Pb-induced skyrmions in a double layer of Fe on Ir(111). In: *Physical Review B* 98 (14 2018), p. 144443 (cit. on p. 69).

[117] S. Meyer, M. Perini, A. Kubetzka, K. von Bergmann, S. Heinze, and R. Wiesendanger. *In preparation*. In: () (cit. on pp. 69, 74, 75, 78, 80, 83, 84, 88).

[118] Y. Kuk and P. Silverman. Role of tip structure in scanning tunneling microscopy. In: *Applied Physics Letters* 48.23 (1986), pp. 1597–1599 (cit. on p. 73).

[119] Y. Kuk, P. Silverman, and H. Nguyen. Study of metal surfaces by scanning tunneling microscopy with field ion microscopy. In: *Journal of Vacuum Science & Technology A: Vacuum, Surfaces, and Films* 6.2 (1988), pp. 524–528 (cit. on p. 73).

[120] P.-J. Hsu, L. Rózsa, A. Finco, L. Schmidt, K. Palotás, E. Vedmedenko, L. Udvardi, L. Szunyogh, A. Kubetzka, K. von Bergmann, et al. Inducing skyrmions in ultrathin Fe films by hydrogen exposure. In: *Nature communications* 9.1 (2018), p. 1571 (cit. on p. 90).

[121] A. Schlenhoff. "Imaging and Switching Individual Nanomagnets with Spin-Polarized Scanning Field Emission Microscopy". PhD thesis. Universität Hamburg, 2013 (cit. on p. 94).

[122] M. Plihal, D. Mills, and J. Kirschner. Spin wave signature in the spin polarized electron energy loss spectrum of ultrathin Fe films: theory and experiment. In: *Physical Review Letters* 82.12 (1999), p. 2579 (cit. on p. 94).

[123] P. Echenique, J. Pitarke, E. Chulkov, and A. Rubio. Theory of inelastic lifetimes of low-energy electrons in metals. In: *Chemical Physics* 251.1-3 (2000), pp. 1–35 (cit. on p. 94).

[124] S. Krause, L. Berbil-Bautista, G. Herzog, M. Bode, and R. Wiesendanger. Current-induced magnetization switching with a spin-polarized scanning tunneling microscope. In: *Science* 317.5844 (2007), pp. 1537–1540 (cit. on pp. 94, 95).

[125] C. Hanneken. "Development and Characterization of Cr Bulk Tips for SP-STM". Universität Hamburg, 2011 (cit. on p. 94).

[126] L. Gerhard, T. Yamada, T. Balashov, A. Takács, R. Wesselink, M. Däne, M. Fechner, S. Ostanin, A. Ernst, I. Mertig, et al. Magnetoelectric coupling at metal surfaces. In: *Nature Nanotechnology* 5.11 (2010), p. 792 (cit. on p. 95).

[127] C.-G. Duan, J. P. Velev, R. F. Sabirianov, Z. Zhu, J. Chu, S. S. Jaswal, and E. Y. Tsymbal. Surface magnetoelectric effect in ferromagnetic metal films. In: *Physical Review Letters* 101.13 (2008), p. 137201 (cit. on p. 95).

[128] A. Sonntag, J. Hermenau, A. Schlenhoff, J. Friedlein, S. Krause, and R. Wiesendanger. Electric-field-induced magnetic anisotropy in a nanomagnet investigated on the atomic scale. In: *Physical Review Letters* 112.1 (2014), p. 017204 (cit. on p. 95).

[129] A. Schlenhoff, S. Krause, A. Sonntag, and R. Wiesendanger. Individual Atomic-Scale Magnets Interacting with Spin-Polarized Field-Emitted Electrons. In: *Physical Review Letters* 109.9 (2012), p. 097602 (cit. on p. 95).

[130] A. A. Khajetoorians, B. Baxevanis, C. Hübner, T. Schlenk, S. Krause, T. O. Wehling, S. Lounis, A. Lichtenstein, D. Pfannkuche, J. Wiebe, et al. Current-driven spin dynamics of artificially constructed quantum magnets. In: *Science* 339.6115 (2013), pp. 55–59 (cit. on p. 95).

List of publications

Articles

Observation of sub-10 nm magnetic skyrmions in zero magnetic fields in Rh/-Co/Ir(111)
S. Meyer, M. Perini, S. von Mallotki, A. Kubetzka, K. von Bergmann, S. Heinze, and R. Wiesendanger
In preparation

Magnetic domain walls in strain-patterned ultrathin films
A. Finco, M. Perini, A. Kubetzka, K. von Bergmann, and R. Wiesendanger
Physical Review B **98** *174435* (2018)

Domain walls and Dzyaloshinskii-Moriya interaction in epitaxial Co/Ir(111) and Pt/Co/Ir(111)
M. Perini, S. Meyer, B. Dupé, S. von Malottki, A. Kubetzka, K. von Bergmann, R. Wiesendanger, and S. Heinze
Physical Review B **97** *184425* (2018)

Contributed talks

Magnetic and chiral properties of epitaxial Pt/Co$_n$/Ir(111) films investigated by SP-STM
M. Perini, A. Kubetzka, K. von Bergmann, and R. Wiesendanger
DPG Spring Meeting, Dresden, Germany, 03.2017

Posters

Magnetic and chiral properties of epitaxial Pt/Co/Ir(111) films investigated by SP-STM
M. Perini, S. Meyer, B. Dupé, S. von Malottki, A. Kubetzka, K. von Bergmann, R. Wiesendanger, and S. Heinze
654. WE-Heraeus Seminar, Bad Honnef, Germany, 11.2017

Magnetic and chiral properties of epitaxial Pt/Co$_n$/Ir(111) films investigated by SP-STM
M. Perini, A. Kubetzka, K. von Bergmann, and R. Wiesendanger
SKYMAG, Paris, France, 05.2017

Acknowledgements

Throughout my PhD many people have helped and supported me in various ways. Here I would like to sincerely thank all of them:

- Prof. Dr. Wiesendanger for his supervision, as well as for giving me the opportunity to do my PhD in his group and to present my results at several conferences;
- Dr. Kirsten von Bergmann and Dr. André Kubetzka for the daily support, the stimulating discussions and the valuable help during all the phases of this work;
- all the current and previous members of Lab013 for the nice time spend together discussing, preparing, measuring, breaking and repairing things;
- everyone in Group R for the friendly atmosphere, as well as for the useful tips and hints;
- Prof. Stefan Heinze, Sebastian Meyer and Stephan von Malottki for the fruitful collaboration, which highly improved the understanding of my results;
- Dr. Robert Frömter, PD Guido Meier, Susanne Kuhrau and Carolin Behncke for their time spent in performing SEMPA and MFM measurements on our samples;
- the mechanical and electronic workshops, as well as the helium and the administrative teams, whose support has been essential to carry out this work;
- the numerous people from the MAGicSky consortium I had the pleasure to meet and discuss with;
- my family, without whose constant and unconditioned support none of this would have been possible;
- and all my friends, who, one way or another, have accompanied me during these years.

Eidesstattliche Versicherung
Declaration on oath

Hiermit versichere ich an Eides statt, die vorliegende Dissertationsschrift selbst verfasst und keine anderen als die angegebenen Hilfsmittel und Quellen benutzt zu haben.

Die eingereichte schriftliche Fassung entspricht der auf dem elektronischen Speichermedium.

Die Dissertation wurde in der vorgelegten oder einer ähnlichen Form nicht schon einmal in einem früheren Promotionsverfahren angenommen oder als ungenügend beurteilt.

Hamburg, den

Unterschrift der Doktorandin/des Doktoranden